Polycrystalline Perovskite Ferroelectrics:
Microstructural Origins of the Macroscale Electromechanical Response

Thesis by
Wei Lin Tan

In Partial Fulfillment of the Requirements for the
Degree of
Materials Science

CALIFORNIA INSTITUTE OF TECHNOLOGY
Pasadena, California

2019
Defended May 16, 2019

Wei Lin Tan
ORCID: 0000-0001-6855-8340

ACKNOWLEDGEMENTS

It has been my dream since middle school to come to Caltech, the birthplace of JPL and an institute brimming with curiosity and excitement about pushing the frontiers of science. My time here could not have been more educational and fulfilling, and I'm grateful to have met many great minds among my professors and peers.

First and foremost, I'd like to express my heartfelt gratitude to my advisors, Prof. Dennis Kochmann and Prof. Katherine Faber.

I'm incredibly thankful, firstly, that Dennis was willing to offer a student with no background in computational mechanics (or even mechanics) a place in his group. It has given me the opportunity to be immersed in and learn about a whole new field of study from my undergraduate work in chemistry and geology, and my graduate coursework in materials science. He is one of the best teachers I've ever had, his wit and sharp insight always a guiding light, and his patience and advice invaluable in making any of my research possible.

Professor Faber is the best co-advisor I could have possibly asked for. Her wealth of experience across myriad fields, her passion for each and every detail of a project, and her calm words of wisdom have been a constant source of inspiration. She has been a pillar of support and her advice always achieves that delicate balance between encouraging exploration and efficient problem-solving.

Next, I would like to thank Prof. George Rossman and Prof. Kaushik Bhattacharya for graciously agreeing to be on my thesis committee and for spending time with me discussing aspects of my research (and sometimes many other fascinating topics which may or may not have been related to the original discussion!).

Many thanks also go out to my research group mates past and present in the Kochmann and Faber groups: My seniors in the Kochmann group, Ishan, Alex, Neel, Yingrui and in particular Stan, who showed me the ropes in unfamiliar waters and made me feel welcome. My friends and contemporaries Vidya, Greg, Carlos, Abbas, Sid, Xiaomei, Neal, Claire, Nori, Ben, Celia and Vince with whom I'd tackled coursework, had lively debates and exchanged ideas, and without whom research life would have been much duller. Special mention also goes to Ms. Denise Ruiz and Ms. Maria Trodella, our administrative staff at Caltech and ETH who ensured that our labs ran smoothly and who were always willing to lend a listening ear.

Thank you to Dr. Chi Ma, Prof. Paul Asimow, Ottman Tertuliano and Sam Loke, whose guidance and insight in characterization and fabrication techniques made much of my research possible. My gratitude also goes to Alan Devoe, Bryce Devoe and Hung Trinh from Presidio Components for their generous collaboration. I'd also like to acknowledge my funding agency, DSO National Laboratories (Singapore) for their support of my studies in Caltech.

Life here can get grueling at times, so I'm infinitely grateful for the support of all my friends within and outside of Caltech, especially my Craft & Tea group Sophia, Sam, Claire, Michelle, Marianna and Sonia, my fellow materials science year mates Max, Mike, Daryl, I-Te, Jin and Xiaolin, and my food buddies Dingyi, Shiori and Celia.

Last but certainly not least, I'd like to thank my family: my parents for their unwavering and unconditional love and support throughout my life, my little brother just starting out in graduate school whose quiet support and academic brilliance motivates me to always reach higher, and finally my husband and fellow Caltech graduate student Yu Xian, who has been both an intellectual sparring partner in school and a loving partner in life.

ABSTRACT

Ferroelectrics are a class of electromechanically coupled materials which possess an electric dipole polarization that can be permanently reoriented by applied electric and mechanical stress fields. Their reorientable polarization results in complex, nano- to micrometer scale domain structures whose evolution under electric and mechanical stress fields alters the material's overall time-dependent electrical and viscoelastic properties. To understand domain structure evolution, in-situ microscopy of domain switching processes in ferroelectric thin films, single crystals and nanoparticles have been well-studied in the past. However, domain evolution in bulk polycrystals is less well understood as their local stress and electric field environment differs from thin specimens.

This work seeks to understand ferroelectric domain evolution in bulk ferroelectric perovskite polycrystals using a combination of a recently-developed electromechanical characterization technique, Broadband Electromechanical Spectroscopy (BES), and theoretical-computational predictions. A constitutive material model for polycrystalline ferroelectrics is first developed and applied to simulate barium titanate single crystals and polycrystals. Simulated polarization, strain and energy dissipation hysteresis curves show good qualitative agreement to experimental data and demonstrate that macroscale properties can be efficiently predicted from microscale physics to some extent.

The microstructural origins of fatigue behavior in bulk polycrystalline lead zirconate titanate (PZT) are investigated using a combination of macroscale electrical and viscoelastic property characterization via BES, and scanning electron microscopy (SEM) imaging of microstructure. The evolution of electrical and viscoelastic properties during bipolar electrical fatigue show differences in the effects of electrical vs. mechanical fatigue processes, and the latter is verified through SEM imaging and measurement of microcracks.

Finally, the same electromechanical BES characterizations are performed on specimens of bulk polycrystalline barium titanate (BT). Results reveal stark qualitative differences in electrical and viscoelastic responses from PZT despite both materials being perovskite ferroelectrics. A growth vs. nucleation hypothesis is proposed to explain the observed results, guided by preliminary imaging of domain microstructure.

In summary, the BES is a powerful tool to elucidate domain switching processes within bulk ferroelectric specimens, while a computational method which bridges the micro- and macroscale further adds to the diagnostic toolbox of understanding bulk ferroelectric domain switching mechanisms. This opens the pathway to designing future applications which make use of the unique electrical and viscoelastic properties of ferroelectric switching.

PUBLISHED CONTENT AND CONTRIBUTIONS

Tan, W. L., Kochmann, D. M. An effective constitutive model for polycrystalline ferroelectric ceramics: Theoretical framework and numerical examples. *Computational Materials Science*, 136:223-237, 2017.
URL `https://doi.org/10.1016/j.commatsci.2017.04.032`
W.-L. T. developed and implemented the numerical methods under the guidance of D. M. K.

Vidyasagar, A., Tan, W. L., Kochmann, D. M. Predicting the effective response of bulk polycrystalline ferroelectric ceramics via improved spectral phase field methods. *Journal of the Mechanics and Physics of Solids*, 106:113-151, 2017.
URL `https://doi.org/10.1016/j.jmps.2017.05.017`
A. V. developed and implemented numerical schemes. W.-L. T. set up and performed experiments under supervision of D. M. K.

Tan, W. L., Faber, K. T., Kochmann, D. M. In-situ observation of evolving microstructural damage and associated effective electro-mechanical properties of PZT during bipolar electrical fatigue. *Acta Materialia*, 164:704-713, 2019.
URL `https://doi.org/10.1016/j.actamat.2018.10.065`
W.-L. T. designed and performed the experimental study under the guidance of K. T. F. and D. M. K.

TABLE OF CONTENTS

LIST OF ILLUSTRATIONS

LIST OF TABLES

Chapter 1

INTRODUCTION, BACKGROUND AND MOTIVATION

1.1 Introductory Remarks

Ferroelectrics are a class of multifunctional materials which possess *switchable electric polarization*. They are named after ferromagnets due to their similarity in having a permanent, re-orientable dipole, but contrary to their etymology, rarely contain iron. Their non-centrosymmetric crystal structure also gives rise to non-linear optical effects, and enables coupling between fields such as *piezoelectricity* (mechanical and electrical) and *pyroelectricity* (thermal and electrical) [Dorfmann and Ogden, 2005, Goulbourne et al., 2005]. These properties make ferroelectrics ideal candidates for innovations in electro-optics, actuation, transduction, sensing, data storage, and many other perhaps as-yet unrealized applications.

Ferroelectrics rose to prominence not so much for their switchable polarization, but for the fact that they can be *poled*. In a typical polycrystalline piezoelectric material such as quartz, each grain has its polar axis aligned in a random direction, effectively nullifying the piezoelectric effect across the bulk ceramic. In a ferroelectric, however, a sufficiently large applied electric field can switch the electric polarization of grains in an already-sintered ceramic, giving the bulk ceramic a net overall polarization. The ability to fabricate a bulk ceramic with piezoelectric functionality is significant in industrial applications because ceramics are far simpler to produce on large scales and require less precision in manufacturing than single crystals.

The most prevalent ferroelectric used in modern society is polycrystalline lead zirconate titanate (PZT), a perovskite ceramic with an exceptionally high piezoelectric coupling coefficient first patented in 1954 [Rosen et al., 1954]. It is ubiquitous in devices ranging from daily appliances like weighing scales and microphones to military-grade sonars. Yet, its use is largely restricted to the linear piezoelectric regime, i.e. electromechanical coupling within a small perturbation of either the electrical or mechanical field.

This is not to say that forays into utilizing the switchable electric polarization of ferroelectrics such as PZT have not been made [Takasu, 2000, Kohlstedt et al., 2005, Dawber et al., 2005, Baudry et al., 2017] – unlike ferromagnetics, perovskite ferroelectrics can have six or more polarization states, potentially greatly increasing the

information density of ferroelectric-based data storage. However, realizing such data storage is fraught with challenges, including difficulty in 'writing' stable nanoscale domains, difficulty in distinguishing different in-plane polarization states, as well as mechanical damage over many write cycles caused by strain from electromechanical coupling.

There is, hence, a rich body of work, both experimental and theoretical, on PZT and other perovskite ferroelectrics like barium titanate (BT), lead zinc niobate (PZN), bismuth titanate niobate (BTN), etc. investigating the effects of ferroelectric domain switching under large electric fields, including large mechanical damping [Jiménez and Vicente, 2000, Chaplya and Carman, 2002a,b, 2001, Wojnar et al., 2014, Le Graverend et al., 2015], significant electrostrictive strains [Burcsu et al., 2004, Shilo et al., 2007], and pronounced changes of the elastic moduli [Carman and McKnight, 2002]. The past decades of work in perovskite ferroelectrics have been, in part, to expand the potential applications of ferroelectrics beyond their basic use as piezoelectrics, and in part, because the simplicity of the perovskite structure inspired the hope that its behavior could be easily modeled either theoretically or computationally. This, however, turned out to not be the case, and many aspects of the mechanisms of polarization switching remain open questions today.

As with many open questions in materials science, we seek to understand processes and properties from their microscale origins. Yet in the case of electromechanically coupled systems such as ferroelectrics, techniques used to observe microscale processes in situ (e.g. X-ray diffraction, transmission electron microscopy (TEM), piezoresponse force microscopy (PFM)) require sample dimensions which are no longer representative of a bulk solid in terms of mechanical constraints [Li et al., 2005, Gao et al., 2013, Polking et al., 2012]. One of the few techniques available to explore switching in bulk ferroelectrics is acoustic emission [Wadley, 1980, Mohamad et al., 1981, Morosova and Serdobolskaja, 1987, Lupascu, 2004], which attributes different microscale processes like domain wall motion, domain wall pinning, microcracks, etc. to different amplitudes, frequencies and characteristic waveforms of emitted acoustic waves. While qualitatively very instructive, the noise and variance in this technique does not lend itself easily to quantitative characterization.

If we are able to close this gap in the understanding of microstructural evolution in bulk ferroelectric ceramics, we can create opportunities to expand the applications of ferroelectrics to their full range of material functionality at the bulk scale. Hence, in

this thesis, we employ Broadband Electromechanical Spectroscopy (BES) [Wojnar et al., 2014, Le Graverend et al., 2015, Kochmann et al., 2014], a recently developed dynamic electromechanical characterization method, on problems in electrical fatigue in PZT and strain limits in BT domain switching. We also compare experimental observations with theoretical-computational predictions, to further our understanding of the behavior of polycrystalline perovskite ferroelectrics at the bulk scale.

1.2 Ferroelectrics Fundamentals

Origins of Ferroelectricity – Crystal Structure

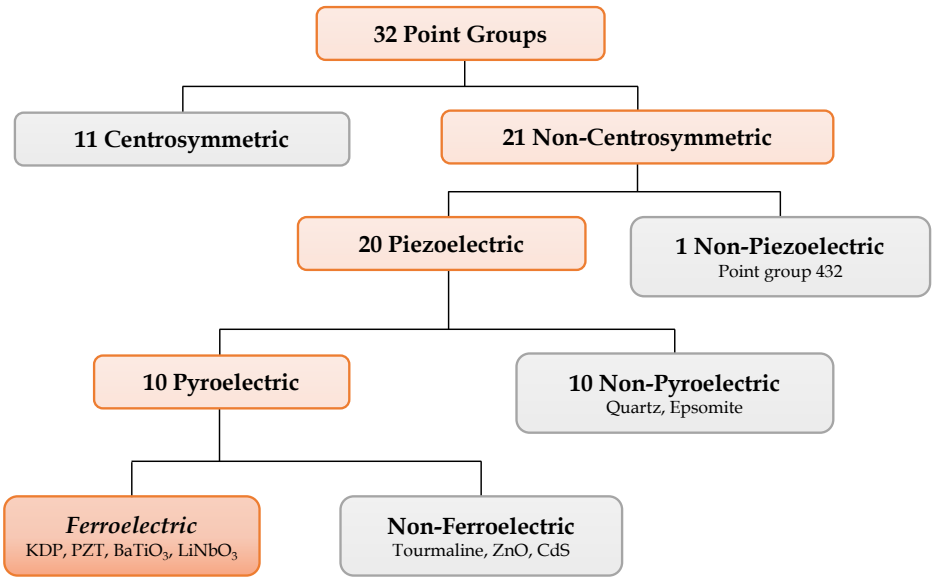

Figure 1.1: Classification of dielectrics based on crystal symmetry. [Haertling, 1999, Helman, 2016]

As mentioned briefly, ferroelectric materials possess several functional properties including non-linear optical effects, pyroelectricity and piezoelectricity. These properties are determined by the crystallographic symmetry point group of the material, as categorized in Figure 1.1.

The permanent, switchable dipole that defines ferroelectric materials arises from a lack of *centrosymmetry* in the material's crystal structure [Jaffe et al., 1971, Lines and Glass, 1977, Moulson and Herbert, 1990]. Simply put, positive and negative charges (in the form of charged ions, hydrogen bonds, etc.) within the unit cell are not symmetrically distributed in all three dimensions. ***Piezoelectricity*** thus arises when

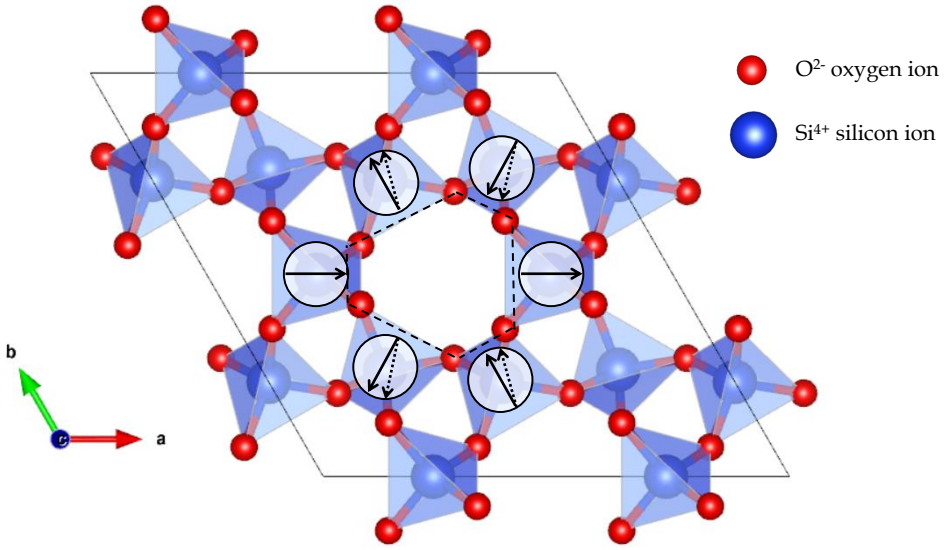

Figure 1.2: Schematic of the structure of α-quartz viewed along the optic axis (c-axis). Dotted lines show the movement of oxygen atoms caused by tilting of SiO_4 tetrahedra during compression along the optic axis. Arrows show the polarization of each tetrahedron and dotted arrows indicate change in polarization direction due to compression, resulting in the piezoelectric effect. [Karasawa, 1974, Momma and Izumi, 2011]

mechanical stress is applied, resulting in different degrees of displacement of the various charges, thus generating an electric dipole moment. Note that only a subset of piezoelectrics have a permanent dipole – although charges are not symmetrically distributed in all three spatial axes, they can still result in a net zero polarization when no external stimulus is applied.

A common example is quartz, one of the earliest-used piezoelectrics, whose structure is pictured in Figure 1.2. In its undeformed state, the low-temperature α-quartz is made up of helical chains of SiO_4 tetrahedra. Each individual tetrahedron has a net polarization, but tetrahedra are arranged such that the net polarization of the full unit cell is zero. In the projection down the c-axis shown in Figure 1.2, the central six tetrahedra form one rotation about the helix. When compression is applied along the c-axis, the tetrahedra in the helix tilt as well as translate in different directions (dotted lines), thus changing their individual polarization orientations (circled arrows) and generating a net overall polarization. When the applied stress is removed, the structure returns to its original configuration and loses its net polarization.

A subset of piezoelectric materials are ***pyroelectric*** materials. These are materials

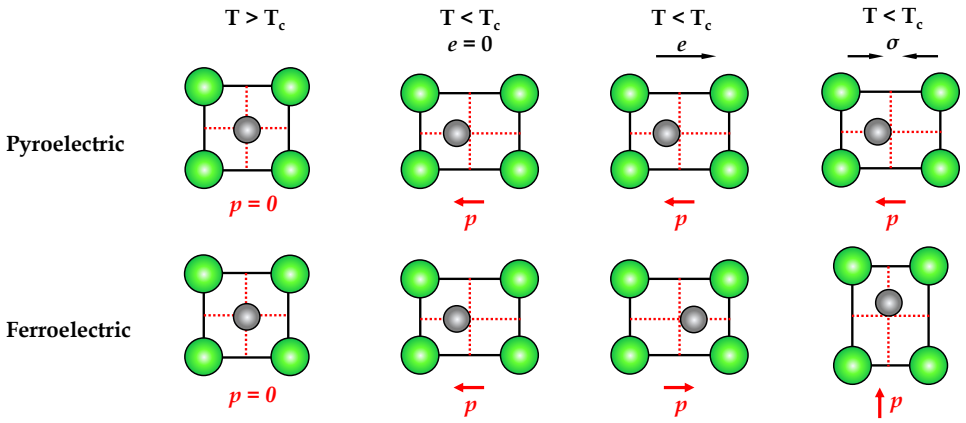

Figure 1.3: Cartoon of the effect of temperature and external fields on pyroelectric and ferroelectric materials. [Lines and Glass, 1977]

which, due to their crystal symmetry, exhibit *spontaneous polarization*. They have temperature-dependent polar and non-polar phases, and the temperature at which the material transitions from non-polar to polar is called the *Curie temperature*, or T_c [Abrahams et al., 1968]. The non-polar phase is typically called the *prototype* phase, and it decreases in symmetry upon cooling, developing a permanent electric dipole. In non-ferroelectric pyroelectrics, this electric dipole, once formed, cannot be switched via an externally applied electric field.

Finally, ***ferroelectrics*** are pyroelectrics with electric dipoles that *can* be switched via an external electric field. Figure 1.3 shows a simplified cartoon differentiating pyroelectrics and ferroelectrics based on their polarization state under different applied external fields. Unlike pyroelectricity and piezoelectricity, whether or not a pyroelectric is also ferroelectric is not defined by its crystal symmetry. In fact, the classification of a ferroelectric is somewhat ambiguous, as the ability to be switched could depend on crystal perfection, electrical conductivity, temperature and pressure among other factors. However for switchability to be feasible, the crystal structure is highly likely to only be a small perturbation from the prototype phase, else the electric field required for switching will exceed the breakdown voltage of the material.

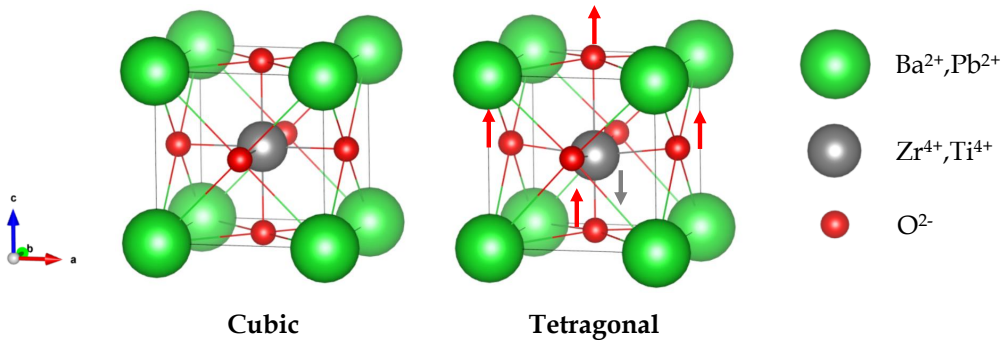

Figure 1.4: Unit cell structure of perovskite BT and PZT showing the high temperature cubic phase (*left*), and the low temperature tetragonal phase (*right*). O^{2-} ions are displaced in the opposite direction from the center Ti^{4+} / Zr^{4+} ions, generating a permanent electric dipole. [Momma and Izumi, 2011]

Perovskite Ferroelectrics

The ***perovskite structure*** obtained its name from the mineral Perovskite ($CaTiO_3$), and has the structural formula $^{VII}A^{2+VI}B^{4+}X^{2-}{}_3$. Its unit cell structure is illustrated in Figure 1.4, using two particular ferroelectric perovskites of interest, $BaTiO_3$ (BT) and $Pb(Zr,Ti)O_3$ (PZT), as examples. The prototype phase of both these ferroelectrics is cubic, with each axis of the unit cell of the same length and all angles at 90°.

Barium titanate's Curie temperature is approximately 120° C [Harwood et al., 1947], and when cooled below this, its structure transforms from cubic to tetragonal. The tetragonal structure has 6 equivalent polarization orientations, each at 90° to each other. When modeling perovskite ferroelectric switching, most computational models tend to assume tetragonal symmetry of the ferroelectric phase. Barium titanate has further phase transitions at 0° C and -90° C to the orthorhombic and rhombohedral symmetries, respectively, but as the majority of applications operate at room temperature or higher, these phases will not be discussed.

Lead zirconate titanate (PZT), as the name suggests, is a solid solution where both Zr and Ti occupy the B site in the perovskite structure. The compositional phase diagram in Figure 1.5 shows that depending on the relative percentage of Zr and Ti, the symmetry of the crystal structure changes. The most technologically relevant composition, 52% Zr - 48% Ti, is exactly on the boundary of the rhombohedral and tetragonal phases, called the *morphotropic phase boundary* (MPB). While the tetragonal phase has 6 equivalent polarization orientations, the rhombohedral phase

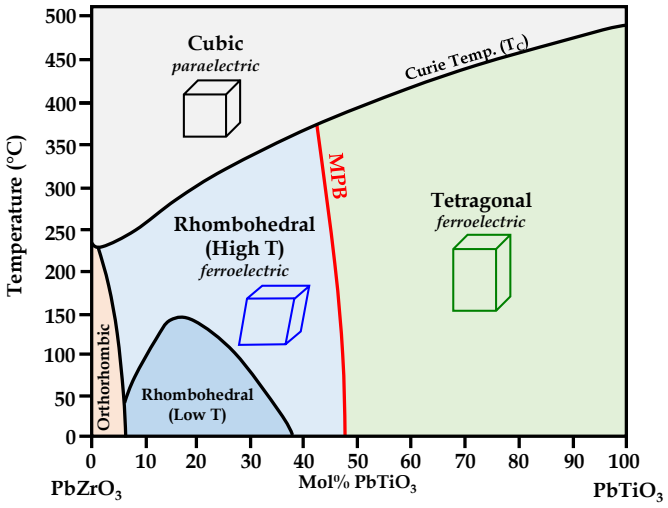

Figure 1.5: Compositional phase diagram of PZT showing the key transition between the paraelectric cubic phase and the ferroelectric tetragonal and rhombohedral phases. The red line indicates the morphotropic phase boundary (MPB), the composition at which the rhombohedral and tetragonal phases coexist. [Jaffe et al., 1971]

has 8 equivalent polarization orientations, pictured in Figure 1.6. It is assumed that the coexistence of these two unit cell structures gives MPB PZT its high piezoelectric coefficient [Hooker, 1998]. In addition to its superior performance in the linear piezoelectric regime, the coexisting phases also behave differently from single-phase PZT in the polarization switching regime. Li et al. [2005] show that the bulk polycrystalline structure can achieve greater strains when under high mechanical stress compared to purely tetragonal or purely rhombohedral samples, which exhibit much smaller strains for the same applied stress.

Despite the relatively simple unit cell structure of perovskite ferroelectrics, the interaction between both internal and externally-applied electrical and mechanical stress fields results in complex arrangements of unit cell orientations even within a single crystal. Each region of homogeneously-oriented unit cells is termed a *domain*, and the mechanism and dynamics of how domains transform within individual grains, as well as across grain in polycrystals, is a hotly investigated topic.

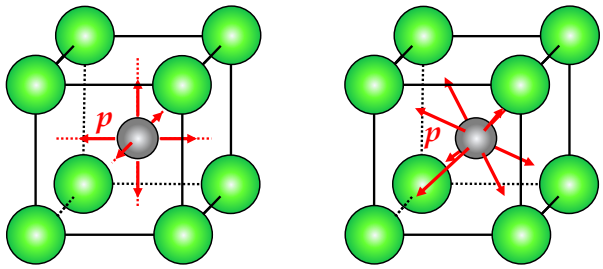

Figure 1.6: Possible polarization directions with respect to the prototype phase unit cell for tetragonal (*left*) and rhombohedral (*right*) ferroelectric perovskites. Oxygen atoms on face centers were omitted for clarity.

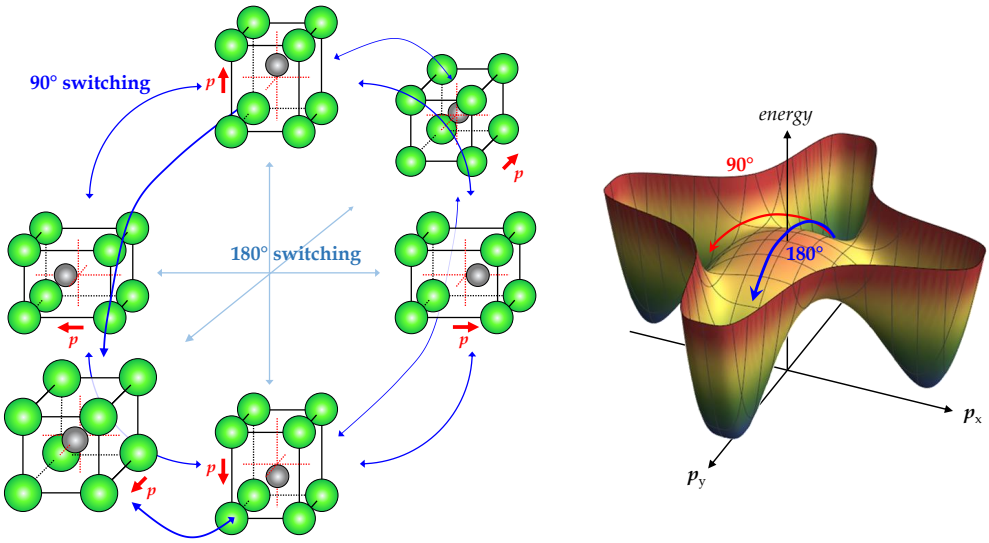

Figure 1.7: Schematic illustrating the six polarization directions of a tetragonal perovskite ferroelectric (*left*). Switching between polarization states can take place via 90°- and 180°-switching. The 2D energy landscape (*right*) gives the 4 stable polarization states in two dimensions, and illustrates the higher energy barrier for 180°-switching versus 90°-switching.

Domain Structure in Single Crystals and Polycrystals

In the absence of external forces, there exist 6 energetically degenerate polarization orientations in tetragonal, and 8 in rhombohedral perovskite ferroelectrics respectively. For simplicity of illustration, the focus will be on the tetragonal phase in this section. As Figure 1.7 shows, there are two possible types of polarization switching

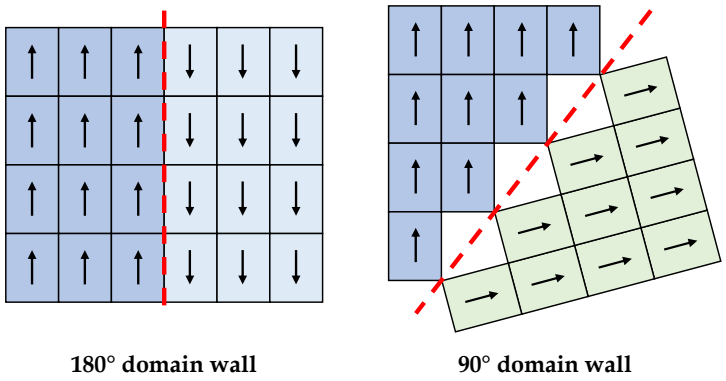

Figure 1.8: Schematic of possible domain walls in a tetragonal perovskite ferroelectric; 180° domain walls are thinner and are not ferroelastic, while 90° domain walls are more diffuse and can be moved by mechanical stress. The 90° domain walls pictured here appear to be less than 90° due to exaggeration in a and c unit cell lengths for illustration purposes.

for tetragonal perovskites: 90° and 180°. The energy landscape illustrates that the activation energy barrier for 180°-switching is higher than that of 90°-switching when there are no mechanical constraints. Hence, there are two possible pathways for switching from a $+z$ polarization to a $-z$ polarization: a single direct 180° switch, or two 90° switches. The former involves little to no change of shape while the latter results in significant deformation because of the $x-$ or $y-$polarized intermediate states. It is important to note that in real samples where individual grains are mechanically constrained by other grains, the energy landscape and thus switching behavior can become a great deal more complex.

A homogeneous region of unit cells with the same polarization orientation is termed a ***domain***, and a single crystal may contain many domains, each being one of the six given orientations. The boundary between adjacent domains, or ***domain wall***, can once again be classified as a 90° domain wall or a 180° domain wall, as per Figure 1.8. Domains typically form to lower the total internal energy of the sample, minimizing mechanical, electrical and interfacial energy. This energy minimization gives rise to complex domain patterns such as rank-I and rank-II laminates, vortices and spinodal structures, also pictured both schematically and in experimental micrographs in Figure 1.9. Since 180°-switching does not involve shape change, 180° domain walls correspondingly can only be moved via an applied electric field, and cannot be moved via application of mechanical stress, i.e. are not ferroelastic. Conversely, 90° domain walls can be moved via either an electric or mechanical field.

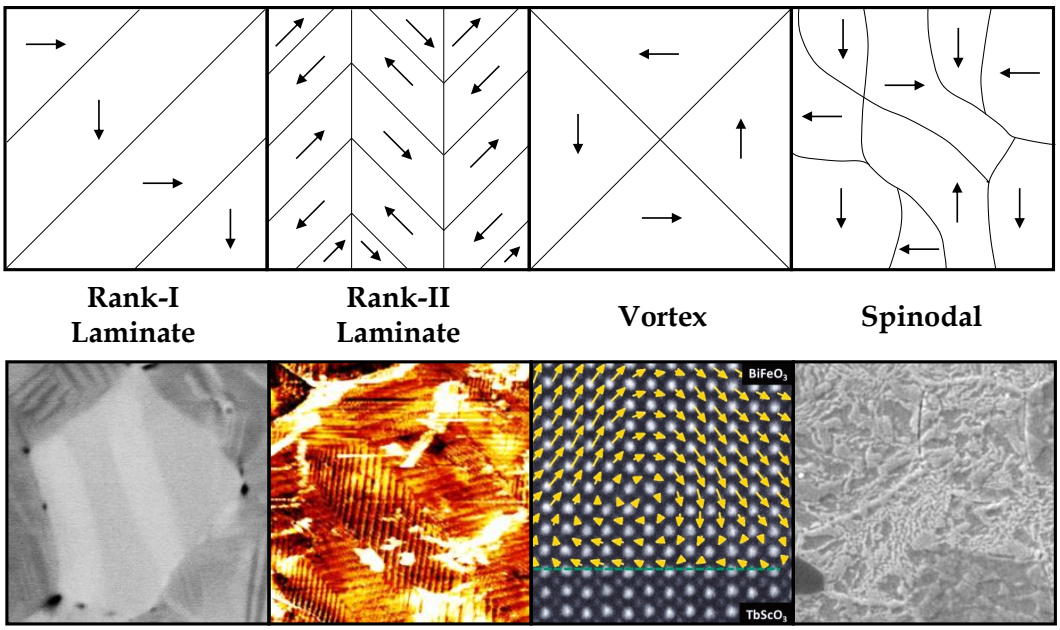

Figure 1.9: Schematics of possible domain structures in a perovskite ferroelectric (*top row*) and experimental micrographs of the same structures (*bottom row*). Rank-I laminates of PZT-5A were taken in-house by SEM and rank-II laminates were taken of BT by PFM (personal communication: Trassin, M. and Kannan, V., ETH Zürich). The vortex is an atomic-scale TEM of $BiFeO_3$ by Pan and Li [2016], and the spinodal structure is an SEM of etched PIC 151 by Lupascu [2004], reproduced with permission.

Unlike in a single crystal which can be cut such that the relevant crystallographic direction is aligned with externally-applied fields, polycrystals are typically randomly oriented, or at best textured, depending on the sintering, poling and cooling process used in fabrication. Each grain is likely tilted with respect to an applied electric or stress field, thus a combination of the 6 domains must exist for the net polarization direction to align with the applied field, as illustrated in the schematics of Figure 1.10. This mixture of domains typically manifests in the form of rank-I or rank-II laminate patterns, as are illustrated in Figure 1.9.

Domain Wall Motion

The domain switching process in ferroelectrics is often used interchangeably with the term ***domain wall motion*** to refer to the growth of existing energetically stable domains at the expense of existing energetically less favorable domains under an applied electric or stress field. This is distinct from ***domain nucleation***, where new

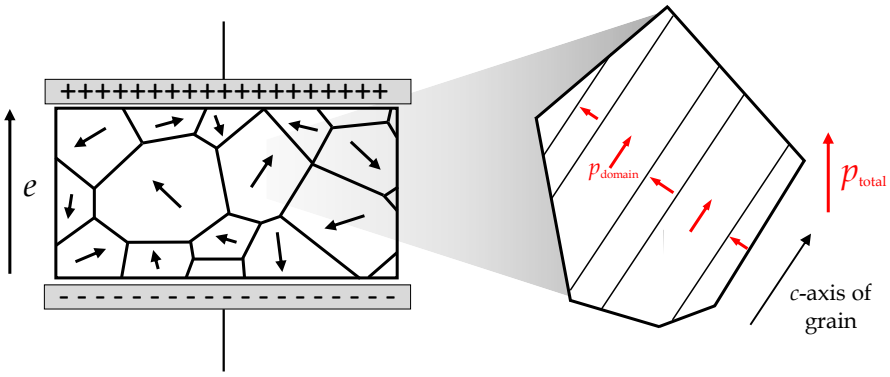

Figure 1.10: Schematic illustrating the randomly oriented c-axes of grains within a ferroelectric ceramic and the associated resulting domain structure when an e-field is applied. A combination of domains will form such that the direction of total polarization is aligned with the applied e-field.

stable domains (and thus new domain walls) are created from within a less stable domain. Both domain wall motion and nucleation occur in concert, with nucleation dominating early on upon the application of an electric field, followed by growth of the newly nucleated domains. Two of the major questions about the domain switching processes are: (*i*) To what extent does domain switching occur by 90°-switching and to what extent by 180°-switching? (*ii*) How do 90°and 180° domain walls respond to applied electric fields and mechanical stress, i.e. what kinetics govern the motion of domain walls? Neither question has a straightforward answer and depends greatly on sample dimensions, experimental configuration, sample history etc.

Early experiments on BT single crystals already demonstrated that characterizing 90°- vs. 180°-switching would not be straightforward – Merz [1954] reported a rank-II laminate structure where switching occurred by rapid nucleation of needle-like domains which grew forward but did not increase in width. Meanwhile Miller [1958] reported that by using aqueous LiCl electrodes instead of noble metal evaporated electrodes, only a few new 180° domains nucleated and grew both forward and in width until full switching was achieved. Nevertheless, more recent studies to determine the combination of crystal orientation, temperature, stress and electric field which would produce desired domain patterns and domain wall motions in single crystals (often termed 'domain engineering') have been fairly successful [Park and Shrout, 1997, Wada et al., 2006, Li and Li, 2014, Mokrý et al., 2016]. Domains were engineered to enhance strain-induced domain wall motion, thereby

increasing the magnitude of the piezoelectric effect beyond that of the c-axis-aligned piezoelectric coefficient.

Beyond patterning static domains, the issue of the kinetics of domain wall motion is also of interest. For example, 180° domain wall motion was keenly studied in the 1950s and 60s [Merz, 1956], one of the products of which is the well-known Merz's Law

$$\dot{\lambda} = \dot{\lambda}_0 \exp\left(-\frac{E_a}{E}\right). \tag{1.1}$$

However, 90°domain wall motion is confounded by the fact that it is a ferroelastic domain wall and, hence, responds to both applied electric fields (which can be well-controlled), as well as to mechanical stress fields (where internal stress in the crystal cannot be controlled). Observations of mixed 180° and 90°-switching in substrate-constrained thin films showed that 90° domains may even remain motionless and instead act as pinning sites for advancing 180° domain walls [Gao et al., 2013, Chang et al., 2011, Sato et al., 2011]. Domain wall motion is further complicated by the effects of pinning at defect sites and grain boundaries (if present) [Schrade et al., 2007, Kontsos and Landis, 2009], making experimental measurements of domain wall velocity the sum total of all effects acting upon the domain wall rather than an isolated pristine measurement.

Instead, using models to explore domain wall kinetics is a way to overcome the practical limits of experiments, but are not without their own drawbacks. Models range from atomic level molecular dynamics, first-principles simulations of switching dynamics [Zhang, 2004, Shin et al., 2007, Chen, 2011, Liu et al., 2016, Boddu et al., 2017], to mesoscale phase field models [Zhang and Bhattacharya, 2005a,b, Su and Landis, 2007, Chu et al., 2014], to macroscale thermodynamic or phenomenological models [Cocks and McMeeking, 1999, Kamlah and Tsakmakis, 1999, Landis, Bassiouny et al., 1988a, Arockiarajan et al., 2006, Miehe and Rosato, 2011]. However, each of them assumes a kinetic evolution law for switching such as the statistical Kolmogorov-Avrami-Ishibashi (KAI) model [Komolgorov, 1937, Avrami, 1940, Ishibashi and Takagi, 1971], gradient flow models, or some variant on Merz's law. Although the results of simulations may give realistic results, it is unclear what the physical basis of these kinetic laws might be in the context of domain switching, and this remains one of the open questions in the study of ferroelectric domain switching today.

1.3 Characterization of Ferroelectrics

In order to investigate the nature of ferroelectric switching in a bulk material, the two most common characteristic hysteresis curves measured are that of ***polarization*** and ***strain*** with respect to applied electric field. The former is a purely electrical measurement, while the latter arises from both linear electromechanical coupling as well as shape change caused by 90°domain switching as described in Section 1.2.

Two more hysteresis curves – ***relative compliance*** and ***mechanical damping***[1] – which give insight to the domain switching process via bulk scale measurements are introduced here. These measurements are obtained using a recently-developed technique in our lab known as Broadband Electromechanical Spectroscopy (BES), which enables simultaneous application of large electric fields and measurement of dynamic mechanical properties [Wojnar et al., 2014, Le Graverend et al., 2015, Kochmann et al., 2014].

Polarization and Electric Displacement

The electric polarization, $\boldsymbol{p}$, is the dipole moment per unit volume within a material, and refers specifically to *bound charges*, ρ_b, i.e. charges bound to atoms in a molecule or crystal structure. This dipole moment may be induced in a regular dielectric material via separation of bound charges by an electric field, or may be a permanent bound charge dipole, as in the case of pyroelectric and ferroelectric materials as previously discussed. $\boldsymbol{p}$ is thus defined by its relation to ρ_b as

$$\rho_b = -\operatorname{div} \boldsymbol{p}. \tag{1.2}$$

Conversely, the electric displacement, $\boldsymbol{d}$, refers to dipoles generated by *free charges*, ρ_f, in the material. This is the quantity of experimental importance because, typically, only free surface charges in a sample can be measured. It is similarly defined as

$$\rho_f = \operatorname{div} \boldsymbol{d}. \tag{1.3}$$

Recalling from electrostatics, the total charge, ρ_{tot} is related to the electric field (e-field), $\boldsymbol{e}$, as follows

$$\rho_{tot} = \kappa_0 \operatorname{div} \boldsymbol{e}. \tag{1.4}$$

Combining the above equations gives us the constitutive equation for e-fields

$$\boldsymbol{d} = \kappa_0 \boldsymbol{e} + \boldsymbol{p}, \tag{1.5}$$

[1] Note: this is to be differentiated from electrical damping, which is a common characterization measure for capacitors, an application also common to ferroelectric ceramics.

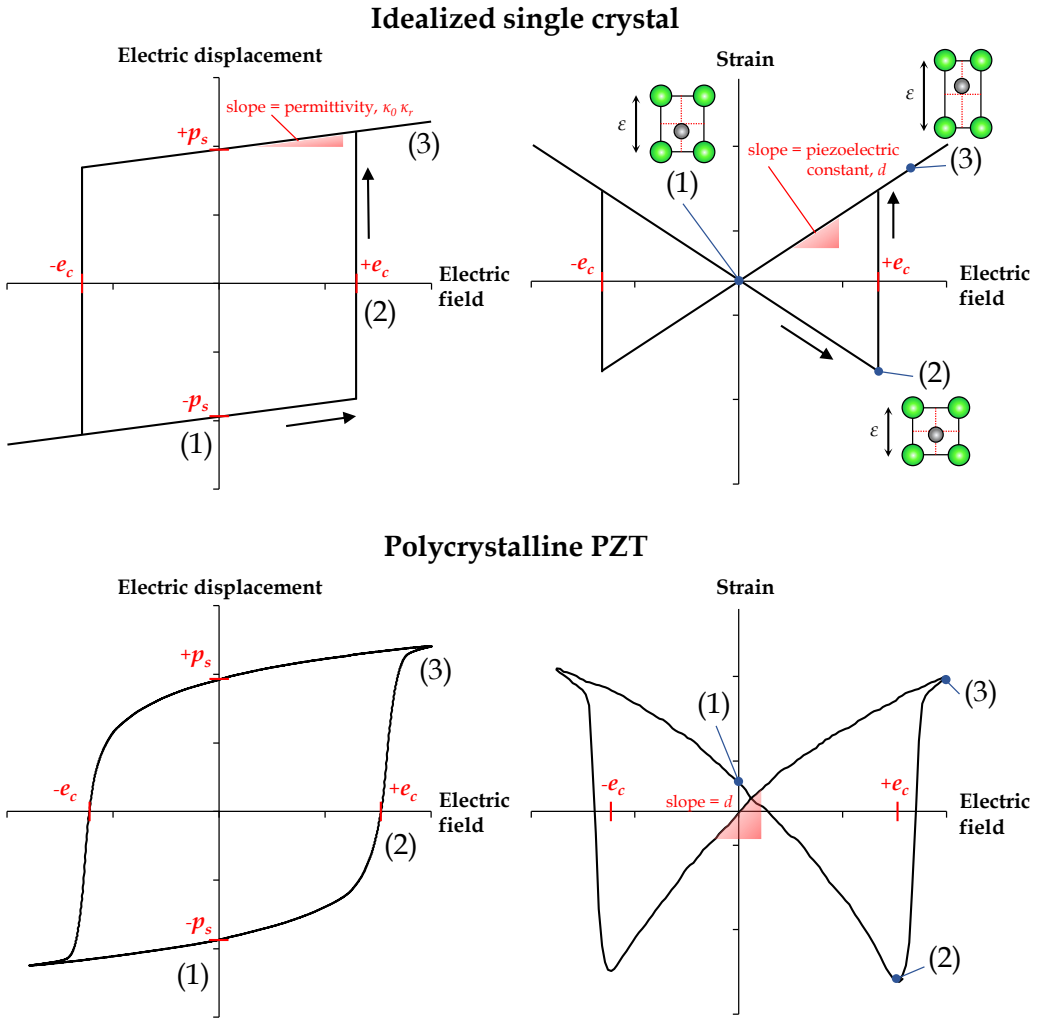

Figure 1.11: Schematic illustrating the idealized single-crystal electric displacement (*top left*) and strain (*top right*), as well as real experimental electric displacement (*bottom left*) and strain (*bottom right*) hysteresis curves, measured in-house at 0.1 Hz e-field cycling frequency at room temperature.

where κ_0 is the permittivity of free space, $8.854\,187\,817 \times 10^{-12}\,\mathrm{F\,m^{-1}}$. It is worth noting that at the e-field strengths relevant to characterization (~$\pm 2\,\mathrm{MV\,m^{-1}}$), and with the permanent polarization magnitudes of PZT and BT (~$0.3\,\mathrm{C\,m^{-2}}$), the term $\kappa_0 \boldsymbol{e}$ is several orders of magnitude smaller than $\boldsymbol{p}$, making $\boldsymbol{d}$ almost equivalent to $\boldsymbol{p}$.

Figure 1.11 shows the electric displacement versus e-field plot of an idealized single-crystal ferroelectric. Key quantities of interest are labeled on the plots, where the linear slope is the *permittivity*, $\kappa_0 \kappa_r$, the intersection of the curve with the horizontal axis is the *coercive field*, $\boldsymbol{e}_c$, and the intersection of the curve with

the vertical axis is the *spontaneous polarization* (sometimes also referred to as *remanent polarization*), $\boldsymbol{p}_s$. To separate the dielectric effect $\boldsymbol{p}_{dielec} = \kappa_0 \chi \boldsymbol{e}$ from the ferroelectric polarization, the constitutive equation can be rewritten as

$$\boldsymbol{d} = \kappa_0 \kappa_r \boldsymbol{e} + \boldsymbol{p}_s \tag{1.6}$$

where

$$\kappa_r = 1 + \chi, \tag{1.7}$$

χ is the electric susceptibility of the material and κ_r is its relative permittivity.

The polarization curves of the same ferroelectric material can vary greatly between samples depending on whether it is single-crystal or polycrystalline, on the sample's dimensions, on grain size, and on whether the sample is subject to any external mechanical constraint [Zhang and Bhattacharya, 2005a,b, Shieh et al., 2009, Tan et al., 2015]. Figure 1.12 shows a few examples of the variety of polarization curves of BT found in the literature. In both single crystals and polycrystals, polarization switching begins at e-fields smaller than the coercive field, giving the curve a rounded shape. The effect is far more pronounced in polycrystals due to the different orientations of grains with respect to the e-field.

Strain

When used as a piezoelectric material, the strain hysteresis curve is one of the most important pieces of material characterization. An idealized curve of strain parallel to e-field, ε_z, versus e-field, e_z, in a single crystal is pictured in Figure 1.11 alongside its associated polarization curve. The key quantity of interest in many industrial applications is the slope of the curve near $\boldsymbol{e} = 0$, where $\frac{d\boldsymbol{\varepsilon}}{d\boldsymbol{e}}$ gives the piezoelectric constant d.

Beginning at an originally negatively polarized state (1), a positive applied e-field will cause the tetragonal unit cell to contract along the c-axis due to the piezoelectric effect. Strain thus decreases linearly until the coercive field, e_c, is reached (2). The polarization switches from negative to positive and the resulting strain becomes an elongation along the c-axis at the given e-field (3). Further increase of e-field results in strain continuing along the same slope of the piezoelectric constant, and similarly upon decrease, the crystal retains its positive polarization and follows the slope to the origin without switching back to its original polarization.

In the case of real materials, and in particular polycrystals, the strain hysteresis curve is not linear due to the effect of 90° switching. Figure 1.11 shows the strain hysteresis

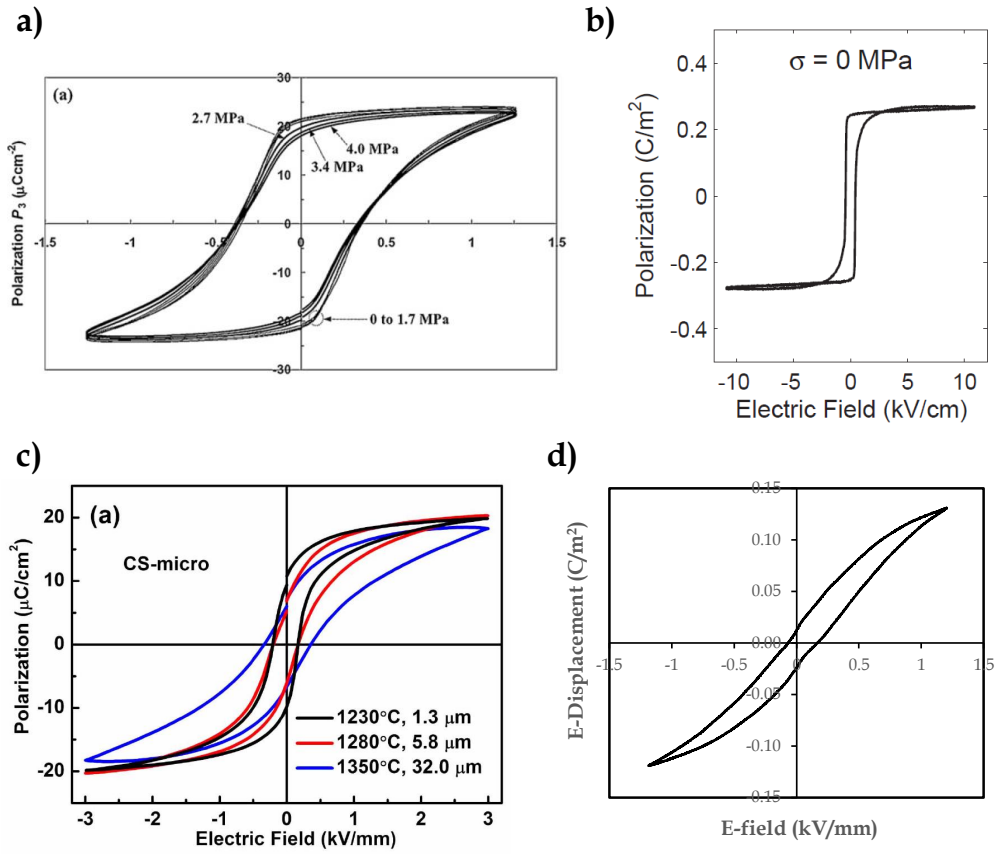

Figure 1.12: Examples of experimental BT polarization curves to demonstrate the variety of hystersis behavior within the same material: a) and b) are single crystals of BT switching under applied pressure [Shieh et al., 2009, Burcsu et al., 2004], c) are poled polycrystalline BT specimens sintered under different conditions and with different resulting grain sizes [Tan et al., 2015] while d) is an in-house measurement of unpoled polycrystalline BT supplied by collaborators from Presidio Inc. Figures are reproduced with permission or under Creative Commons.

of polycrystalline PZT as measured in our lab. Contrary to the idealized case, in an e-field opposing the original direction of polarization, the slope is greater than in an e-field in the same direction as the polarization. This arises from the fact that some 90° switching occurs, which lowers the total strain by a greater magnitude than the linear piezoelectric effect. In an e-field aligned with the direction of polarization, strain also cannot increase linearly infinitely, thus strain magnitude saturates at high e-fields.

Broadband Electromechanical Spectroscopy

One of the reasons why switching behavior in bulk ferroelectrics is not as well-studied as it is in thin films is in part due to an inability to simultaneously probe mechanical properties in situ while applying high e-fields. A large range of dynamic mechanical testing apparatuses exist, including Dynamic Mechanical Analysis (DMA) [Lakes, 2004], Inverted Torsion Pendulum (ITP) [Kê, 1947], Resonant Ultrasound Spectroscopy (RUS) [Migliori et al., 1993], and Broadband Viscoelastic Spectroscopy (BVS) [Lakes and Quackenbusch, 1996, Lakes, 2004, Dong et al., 2008] among others. However, each of these suffers from limitations in the maximum stiffnesses that can be measured, insufficiently high time resolution, or difficulty in adapting the setup to allow for simultaneous application of high e-field, limiting their application in the study of ferroelectric ceramics. On the other hand, Acoustic Emissions allows for simultaneous application of high e-field while probing internal sources of abrupt deformation in the form of domain switching and cracking by measuring emitted acoustic waves in a manner similar to seismography [Wadley, 1980, Mohamad et al., 1981, Morosova and Serdobolskaja, 1987, Lupascu, 2004]. However, as with seismography, it is a form of passive measurement.

The ability to actively measure dynamic mechanical properties of a bulk sample during application of high e-field was recently developed in our lab by Kochmann, le Graverend and Wojnar, dubbed ***Broadband Electromechanical Spectroscopy (BES)*** [Wojnar et al., 2014, Le Graverend et al., 2015, Kochmann et al., 2014]. It utilizes contactless mechanical driving oscillations across a wide range of frequencies to measure dynamic compliance and damping of a sample while simultaneously applying a high e-field.

The instrument consists of two separate driving circuits as illustrated in the schematic in Figure 1.13. The specimen must be prepared as an electroded cantilever beam, which is gripped at the base by an electrically isolated grip at the center of the setup.

Electric Displacement Measurements

Electrical measurements of the sample, specifically electric displacement, are taken using a Sawyer-Tower circuit, which consists of a capacitor of known capacitance in series with the sample, and the voltage is measured across the known capacitor. Conversion from voltage measured to electric displacement is as follows:

$$V_{measured} = \frac{q_{f,capacitor}}{C_{capacitor}} \tag{1.8}$$

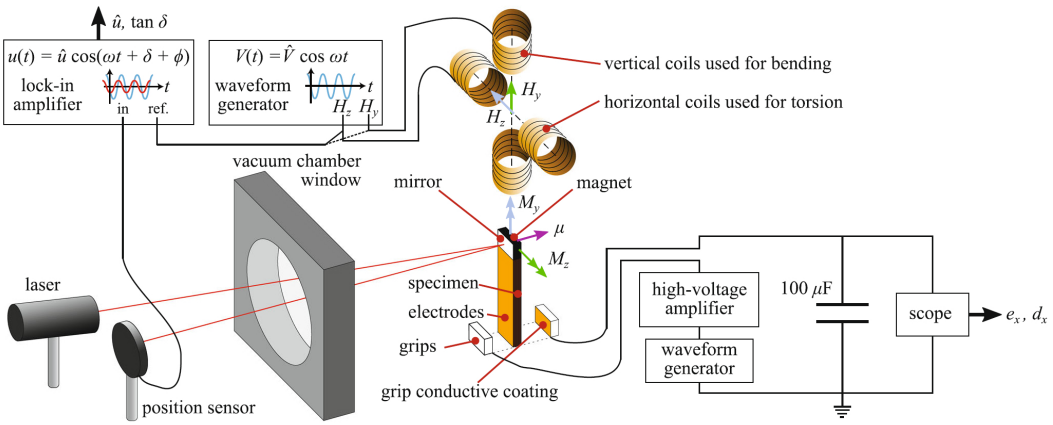

Figure 1.13: Schematic of the BES apparatus with the beam specimen clamped in the center by grips connect to a Sawyer-Tower circuit (*bottom right*). A magnet and mirror are attached to the top of the specimen. Above the sample are two pairs of Helmholtz coils – a vertical pair for bending and a horizontal pair for torsion – which are lower over the sample such that the magnet lies in the center of the four coils. This setup can be enclosed in a vacuum chamber with a window for the laser to reflect off the mirror on the specimen. The coils are driven by a sinusoidal waveform from the waveform generator, and the reflected laser position is fed into a lock-in amplifier to determine amplitude and phase delay (*top left*). This figure has been reproduced from Le Graverend et al. [2015] with permission.

since the sample and capacitor are in series, $\rho_{f,capacitor} = \rho_{f,sample}$. Recalling that

$$\rho_{f,sample} = \text{div}\, \boldsymbol{d}_{sample}, \tag{1.9}$$

for a parallel plate configuration, this simplifies to

$$\boldsymbol{d}_{sample} = \frac{q_{f,sample}}{A}, \tag{1.10}$$

where A is the area of one face of the specimen. Hence,

$$\boldsymbol{d}_{sample} = \frac{V_{measured}}{C_{capacitor} \times A}. \tag{1.11}$$

To obtain the relevant hysteresis measurements, a triangle waveform bipolar e-field is applied across the sample thickness with a peak-to-peak amplitude that depends on the specimen material and dimensions. The frequency of the waveform can be varied from $< 0.01\ Hz$ to $> 10\ Hz$ without damage to the sample, however at very low frequencies, leakage current becomes significant. We thus limit our measurements to applied e-fields of frequency between 0.1 - 10 Hz to minimize confounding factors.

Compliance and Damping Measurements

Dynamic mechanical measurements of the sample are done in bending mode in a contactless fashion. A permanent magnet (neodynium-boron-iron, 6.35 mm × 6.35 mm × 2.54 mm, 12 N maximum pull) is attached to the sample's top end via a stiff Macor® clamp. The magnet is enclosed by a pair of vertical magnetic coils driven electronically, which exert an oscillating transverse force on the beam's tip in a contactless fashion, resulting in beam bending [Lakes and Quackenbusch, 1996]. The frequency of oscillation is chosen to be significantly higher than the frequency of the applied electric field so that the fields are temporally decoupled, i.e. while the bias electric field slowly traverses the full electrical hysteresis approximately quasistatically, fast mechanical vibrations are used to extract the viscoelastic response at each point on the electrical hysteresis.

To measure the viscoelastic properties of the specimen, a mirror is attached to the Macor® clamp, and a HeNe laser beam is reflected off the mirror into a split-diode position detector. The signal from the position detector is fed into a lock-in amplifier to determine the amplitude of the reflected beam and the phase lag of the reflected beam with respect to the driving frequency of the magnetic coils. The amplitude of the reflected beam is a proxy for the dynamic compliance of the specimen while the phase lag gives the mechanical damping in terms of the loss tangent. Wojnar's thesis [Wojnar, 2014] gives the detailed derivations of the conversion between raw measured data and the viscoelastic properties of relative compliance (or stiffness) and loss tangent ($\tan\delta$), whose final forms are reproduced here.

Relative compliance is determined from measured output voltages as

$$\frac{|S|}{|S_0|} = \frac{V_{comp}}{V_{comp,0}}, \tag{1.12}$$

where S_0 is the dynamic compliance of the specimen when no e-field is applied, i.e. $\boldsymbol{e} = 0$, S is the dynamic compliance during cycling, $V_{comp,0}$ is the voltage output of the amplitude channel of the lock-in amplifier at $\boldsymbol{e} = 0$ and V_{comp} is the voltage output during cycling.

Loss tangent is calculated from measured output voltages as

$$\tan\delta = \tan(18^\circ \times V_{damp} + \phi), \tag{1.13}$$

where V_{damp} is the voltage output of the phase delay channel of the lock-in amplifier, 18° is the instrument's built-in conversion constant, and ϕ is the phase delay due to impedance in the solenoids.

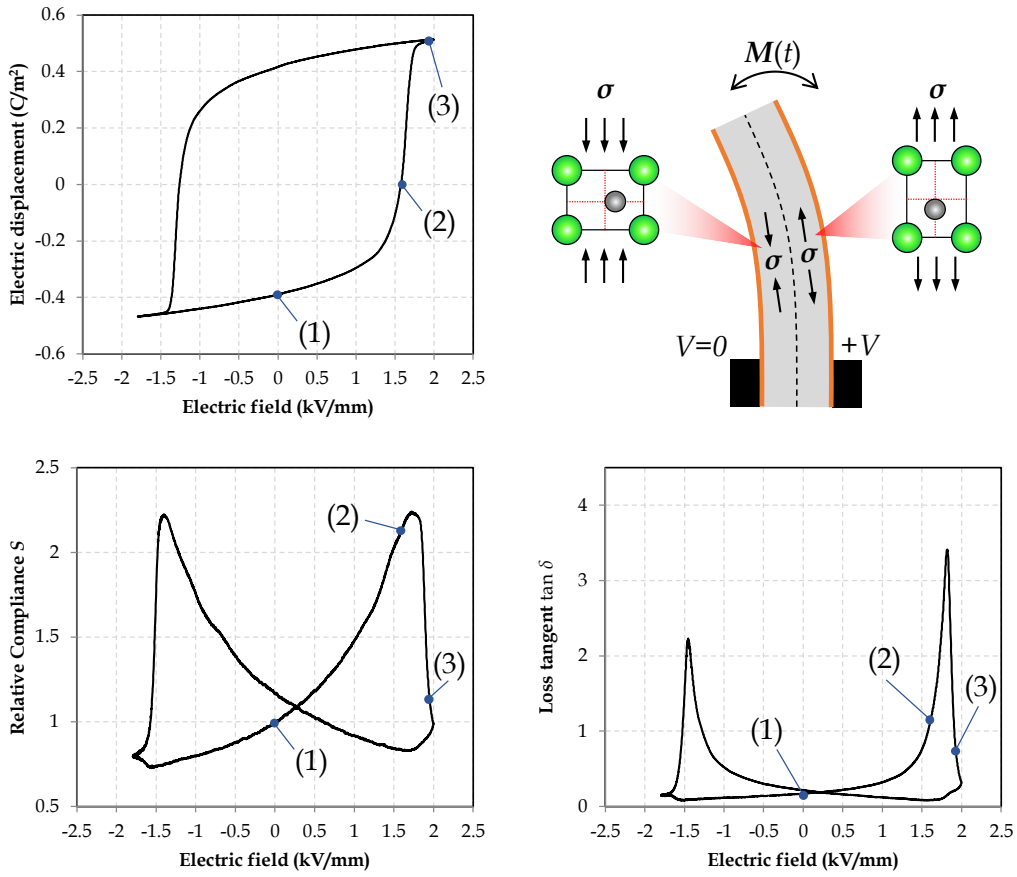

Figure 1.14: Representative hysteresis curves of electric displacement (*top left*), relative compliance (*bottom left*) and damping (*bottom right*) of PZT-5A as measured by the BES apparatus. A schematic (*top right*) of the stress state of the beam specimen under bending shows the associated mechanically induced domain switching processes when the specimen is under electrical loading close to the coercive field.

Figure 1.14 shows representative curves of electric displacement, relative compliance and damping of a specimen of PZT-5A, and a schematic of the beam specimen. The features of the relative compliance and damping hysteresis curves are the result of domain switching induced by mechanical stress (to be differentiated from domain switching induced by the application of an e-field, although both stimuli act in concert).

Beginning at the negatively polarized state (1), as the e-field is increased in the positive direction, the relative compliance increases. Recalling the discussion on strain hysteresis, in a polycrystal, 90° domain switching causes a greater-than-linear change in strain. Similarly in the case of relative compliance, when the specimen is bent, half the specimen is under compression while the other half is

under tension. When no e-field is applied, the stress required to cause switching is far greater than the stress induced by the small amplitude bending. However, as the e-field is increased, this mechanical switching becomes more feasible, leading to switching into z-aligned domains in the compressive half and x-aligned domains in the tensile half, resulting in *further* bending of the beam beyond that of a linear elastic material in bending. This manifests as an apparent increase in compliance. Relative compliance peaks at the coercive field (2) where mechanically induced domain switching can occur with the greatest ease, and rapidly drops again beyond the coercive field (3), where the electric field is now aligned with the dominant polarization direction, hence no longer induces domain switching.

The damping hysteresis curve can be explained in a similar manner. The damping curve measures the amount of *mechanical energy* absorbed by the material. Using the above sequence of domain switching events, and noting that mechanically induced domain switching absorbs mechanical energy, it is immediately clear that the greater the amount of mechanical domain switching, the greater the mechanical energy absorbed, up to the point where the coercive field is exceeded and the damping returns to close to its base $\boldsymbol{e} = 0$ value.

With these two viscoelastic measurements of a bulk ferroelectric taken in situ during e-field cycling, coupled with simultaneous measurements of electric displacement and strain, the BES becomes a powerful tool to non-destructively elucidate domain switching processes as well as other changes in mechanical properties (e.g. microcracking). We are not only able to investigate e-field and mechanical driving frequency dependence [Wojnar et al., 2014], but can also track these properties over hundreds of thousands of cycles to better understand fatigue in the material, as shall be explored in Chapter 3.

Microstructure Imaging

A discussion on the bridging of scales between microstructural origins of domain switching and macroscopic electromechanical properties is of course incomplete without a brief overview of some of the common methods of visualization of ferroelectric domains.

Polarized light microscopy (PLM) was one of the earliest methods of visualization of ferroelectric domains which continues to be used today. As domains are anisotropic, domains of different orientations will exhibit different interference colors, hence at the appropriate cross-polarization angle, domains can be imaged with significant

contrast. It is a non-destructive method which permits in-situ observation of evolving domains, but requires a thin, transparent specimen, and its resolution of domain sizes is limited to microns, as is typical of optical microscopy [Merz, 1954, Lines and Glass, 1977].

A higher resolution method of domain visualization is by ***scanning electron microscopy (SEM)***. Specimens must be etched (often with HF, but many acids can also be used), and different domains at the surface will have different surface charge and energies, thus be etched differentially, creating slight topography which can be resolved in secondary electron mode. A carefully polished surface with minimal etching may sometimes be sufficient, as the differently oriented domains backscatter electrons to different extents, creating subtle contrast in backscatter mode. SEM affords resolution at tens of nanometers, sufficient to resolve laminate patterns within grains in a polycrystal, however the technique is destructive, is limited to surface features, and in-situ evolution observations are extremely challenging.

Transmission electron microscopy (TEM) is among the highest resolution methods of domain visualization. It has atomic-scale to nanometer-scale resolution which offers the unique opportunity to track the displacements of individual atoms from their unit cell centers in order to determine the exact position of domains and domain walls. Gao et al. [2013], Chang et al. [2011] and Sato et al. [2011] are among the several groups who have visualized the growth of domains in situ in the TEM, and have revealed the influence of very thin (~50 nm) laminates on pinning of domain walls during switching. While an extremely powerful technique in studying the mechanisms of domain switching at the smallest of scales, drawbacks of TEM include the thin sample dimensions, difficulty of sample preparation, and the complication of using a high-energy electron beam to study a phenomenon which is electric field-driven.

Finally, ***piezoresponse force microscopy (PFM)*** was developed primarily for the purpose of imaging piezoelectric and ferroelectric domains as miniaturization of devices based on these materials required careful characterization of the domain structure. PFM has an out-of-plane mode which characterizes the vertical displacement in response to an electrical bias applied by the cantilever tip, and an in-plane mode which characterizes the horizontal or shear displacement. Unlike TEM, PFM requires little sample preparation while offering nanometer-scale domain resolution. It is non-destructive, and can also be used to induce in-situ domain switching. However, it is also limited to surface characterization, which may not be representative

of bulk properties [Kalinin et al., 2006].

1.4 Outline

This thesis seeks to shed light on domain switching processes in bulk polycrystalline perovskite ferroelectrics using a combination of computational simulations and macro- and microscale experimental techniques.

The first step in elucidating microscale domain switching processes from macroscale measurements is to develop an efficient bridging of scales such that physics at the microscale can predict salient features in macroscale measurements. Chapter 2 thus aims to formulate one such physics-based constitutive material model for polycrystalline ferroelectrics. The model is then applied to the simulation of polarization, strain and energy dissipation hysteresis curves of single-crystal and polycrystalline barium titanate under different orientations and stress conditions, and results are compared with experimental measurements in the literature.

Chapter 3 tackles an old but perennial issue in ferroelectric ceramics – fatigue. Broadband Electromechanical Spectroscopy (BES) is employed to track not only polarization of PZT as it is fatigued by bipolar electrical cycling, but for the first time, relative compliance and damping as well. The electrical and viscoelastic measurements in concert reveal changes in both electrically induced and mechanically induced domain switching processes, and together serve as a powerful tool for interpreting microscale changes in ferroelectric ceramics during fatigue. BES measurements also enable tracking of mechanical damage in the sample, which is further verified by SEM imaging and determination of microcracking extent.

Finally, BES interpretations of domain switching are applied to understanding domain switching in barium titanate, as Chapter 4 explores. Stark differences in electrical and viscoelastic behavior between PZT and BT are highlighted and discussed. The effects of varying electric field frequency as well as mechanical oscillation frequency are presented, and a hypothesis for the domain switching mechanisms involved is proposed.

Chapter 5 summarizes the key findings of this thesis and discusses remaining open questions and potential future investigations on the topic.

Chapter 2

CONSTITUTIVE MODEL FOR POLYCRYSTALLINE FERROELECTRICS

Research presented in this chapter has been adapted from the following publications:

Tan, W. L., Kochmann, D. M. An effective constitutive model for polycrystalline ferroelectric ceramics: Theoretical framework and numerical examples. *Computational Materials Science*, 136:223-237, 2017.
URL https://doi.org/10.1016/j.commatsci.2017.04.032

2.1 Introduction

We have seen from chapter 1 that the origins of ferroelectric domain switching have been thoroughly investigated at several different scales ranging from the atomic to domain-level to thin films (2D) and most recently in bulk polycrystals (3D). The energetics and hence the equilibrium response of ferroelectrics are thus understood fairly well and have been modeled extensively at each scale, beginning with the seminal works of Landau [1937] and Devonshire [1949, 1951]. On the single crystal level, microscopically-motivated phase field models [Zhang and Bhattacharya, 2005a,b, Su and Landis, 2007, Chen et al., 2008, Xu et al., 2010, Schrade et al.] as well as atomistic [Zhang, 2004, Chen, 2011] or relaxation-based approaches [Shu and Bhattacharya, 2001, Kinderlehrer, 1987] have given insight into the electromechanical coupling and the (quasistatic) electrical hysteresis [Hwang et al., 1995, Chen and Lynch, 1998, Huber and Fleck, 2001, Huber, 2005, Elhadrouz et al., 2005, Zhang and Bhattacharya, 2005a,b, Su and Landis, 2007, Arockiarajan and Sansour, 2008]. The macroscopic behavior of polycrystalline ferroelectrics has been investigated by both phenomenological [Cocks and McMeeking, 1999, Kamlah and Tsakmakis, 1999, Yu et al., Pasco and Berry, 2004, Landis] and thermodynamics-based approaches [Bassiouny et al., 1988a,b, Bassiouny and Maugin, 1989a,b, Schröder and Romanowski, 2005, Arockiarajan et al., 2006, Miehe and Rosato, 2011], see also Kamlah [2001], Landis [2004] for reviews. Models and experiments have also highlighted the dependence of the electrical hysteresis on the material's microstructure, see, e.g. [Merz, 1954, Little, 1955, Arlt and Sasko, 1980, Ahluwalia and Cao, 2001, Cheng et al., 1996]. In contrast to the quasistatic performance,

the temperature-, electric field-, and stress-dependent kinetics of the rate-dependent domain switching process have left many open questions. A major focus has been on *thin films* whose behavior was studied computationally [Zhang and Bhattacharya, 2005a, Gao et al., 2013, 2014, Pálová et al., 2007] and experimentally [Hong et al., 1999, Gao et al., 2013, 2014] and is affected by the free surfaces. In particular for the macroscopic scale of polycrystalline-polydomain *bulk* ferroelectric ceramics, only a few models exist that efficiently and accurately describe the nonlinear electrical hysteresis and the associated physics of domain switching [Uetsuji et al., 2015].

Here, we present a variational constitutive model for polycrystalline ferroelectric ceramics which describes the electro-mechanically-coupled performance under externally applied bias electric fields and stresses under isothermal conditions; the model can further be extended to capture structural transitions such as the martensitic transformation at the Curie temperature of perovskites (although this is not the focus here). Our goal is to retain as much microstructural information as possible (e.g., resolving the individual domain volume fractions in each grain of the polycrystal) but to formulate a model that is sufficiently efficient to be used in macroscopic simulations at the structural and device level, as demonstrated by finite element calculations. Existing models based on microscale physics, such as phase field and FE^2 models, are too expensive to efficiently simulate specimen- or device-level geometries. Conversely, macroscale phenomenological models do not capture all aspects of microscale origins of domain switching. We overcome these limitations in computational expense by applying an entropy-based energy minimization scheme at the grain scale to model the domain switching processes in a single crystal, and apply Taylor homogenization of randomly oriented grains to give the bulk material response. Results show that these simplifications do not have significant adverse effects on the physics that the model is able to capture.

While the general model outlined here is versatile and sufficiently general to be applied to various materials systems, it is specialized for the description of tetragonal perovskites and applied to simulate the response of $BaTiO_3$. In Section 2.2 we summarize the constitutive model (starting on the single-domain level and advancing to a polycrystal-polydomain model). Section 2.3 describes the specific assumptions and material parameters for $BaTiO_3$. Section 2.4 gives an overview of simulation results, and Section 2.5 concludes this contribution.

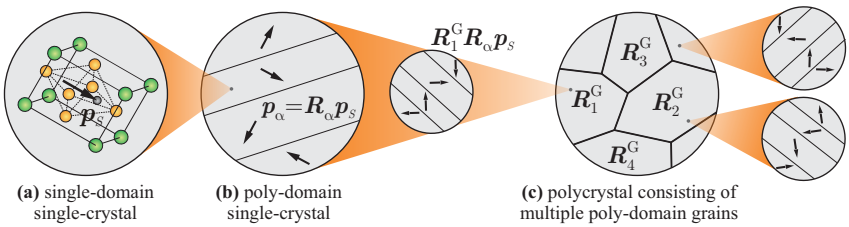

Figure 2.1: Constitutive model construction from single-domain single crystals to multi-domain polycrystals of tetragonal perovskites.

2.2 Constitutive model

In the following, we discuss the basic concepts of the constitutive model with increasing complexity, starting with a single ferroelectric domain, extending the former to single crystals containing multiple domains, and finally relaxing the single crystal model into an effective polycrystal description; see the schematic in Fig. 2.1. Throughout, we focus on ferroelectric ceramics whose typically small strains allow for the use of linearized kinematics. In addition, we start by assuming isothermal conditions as well as loading scenarios sufficiently slow for assuming quasistatic governing equations (i.e., we capture rate effects but neglect the influence of inertia and resonance phenomena; the extension to dynamics is straight-forward because it does not affect the constitutive model but is handled at the finite element level). We note that for the electro-mechanical field variables we choose common continuum-mechanics notation (other communities may prefer another set of symbols).

Single crystal single-domain description of ferroelectrics

Consider a single crystal consisting of only a single ferroelectric domain described by the polarization vector $\boldsymbol{p}$, electric field vector $\boldsymbol{e} = -\operatorname{grad}\varphi$ (where φ denotes the electric potential), and a uniform infinitesimal strain tensor $\boldsymbol{\varepsilon}$. The stored energy density of the crystal (usually referred to as the *electric enthalpy*) is assumed to additively decompose into mechanical and electrical energy density [Zhang and Bhattacharya, 2005a, Su and Landis, 2007], i.e.,

$$W(\boldsymbol{\varepsilon}^e, \boldsymbol{e}, \boldsymbol{p}) = \frac{1}{2}\boldsymbol{\varepsilon}^e \cdot \mathbb{C}(\boldsymbol{e}, \boldsymbol{p})\, \boldsymbol{\varepsilon}^e - \frac{\epsilon}{2}\, \boldsymbol{e} \cdot \boldsymbol{e} - \boldsymbol{e} \cdot \boldsymbol{p}, \tag{2.1}$$

where

$$\boldsymbol{\varepsilon}^e = \boldsymbol{\varepsilon} - \boldsymbol{\varepsilon}^r \tag{2.2}$$

is the elastic contribution to the total strain tensor $\boldsymbol{\varepsilon}$, and $\boldsymbol{\varepsilon}^r = \boldsymbol{\varepsilon}^r(\boldsymbol{e}, \boldsymbol{p})$ is the remanent strain tensor. In general, the elastic modulus tensor $\mathbb{C}$ is anisotropic and depends on both the applied electric field $\boldsymbol{e}$ and the polarization $\boldsymbol{p}$, see Liu and Huber

[2007], so that the two energetic contributions are strongly coupled. For simplicity (and because this is approximately the case in the studied materials systems), we assume an orientation-independent electric permittivity ϵ.

The infinitesimal stress tensor $\boldsymbol{\sigma}$ follows from the electric enthalpy density by differentiation, viz.

$$\boldsymbol{\sigma} = \frac{\partial W}{\partial \boldsymbol{\varepsilon}} = \mathbb{C}\,(\boldsymbol{e}, \boldsymbol{p})\ (\boldsymbol{\varepsilon} - \boldsymbol{\varepsilon}^r), \tag{2.3}$$

Note that Maxwell stresses are negligible in ferroelectric ceramics at small strains, which is why they are neglected here. Linear momentum balance in the absence of body forces or inertial effects requires

$$\operatorname{div} \boldsymbol{\sigma} = \mathbf{0}. \tag{2.4}$$

Similarly, the electric displacement vector $\boldsymbol{d}$ and the thermodynamic driving force $\boldsymbol{y}$ conjugate to the polarization are, respectively,

$$\boldsymbol{d} = -\frac{\partial W}{\partial \boldsymbol{e}} = \epsilon\, \boldsymbol{e} + \boldsymbol{p}, \qquad \boldsymbol{y} = -\frac{\partial W}{\partial \boldsymbol{p}}, \tag{2.5}$$

and Gauss' law for quasistatics (assuming no free charges are present) implies that

$$\operatorname{div} \boldsymbol{d} = \mathbf{0}. \tag{2.6}$$

The above constitutive framework must be completed by a kinetic relation for the evolution of the polarization $\boldsymbol{p}$, which is generally a dissipative process. Examples of phenomenological kinetic laws can be found in Miehe and Rosato [2011] or Idiart [2014].

We note that, if the stress tensor $\boldsymbol{\sigma}$ is known instead of the strains, it is convenient to introduce the (full) enthalpy density

$$W^*(\boldsymbol{\sigma}, \boldsymbol{e}, \boldsymbol{p}) = \frac{1}{2}\boldsymbol{\sigma} \cdot \mathbb{C}^{-1}\,(\boldsymbol{e}, \boldsymbol{p})\,\boldsymbol{\sigma} - \frac{\epsilon}{2}\,\boldsymbol{e} \cdot \boldsymbol{e} - \boldsymbol{e} \cdot \boldsymbol{p}. \tag{2.7}$$

Single crystal poly-domain description of ferroelectrics

Next, we consider a single crystal that consists of multiple ferroelectric domains differing by their polarization vectors. Such domain structures have been observed experimentally and primarily arrange in laminate patterns [Arlt and Sasko, 1980, Hu et al., 1986, Tsou et al., 2011] and (less frequently) vortices [Gruverman et al., 2008, Chen et al., 2012] to satisfy geometric and electrical compatibility at domain interfaces. Here, as an efficient approximation, we relax this constraint and neglect

the exact geometric arrangement. Of course, this is a strong assumption but we must make compromises between accuracy and efficiency.

Assume a ferroelectric ceramic is in its tetragonal, polar phase with a spontaneous polarization vector $\boldsymbol{p}_s$ of magnitude $p_s = |\boldsymbol{p}_s|$. The orientation of $\boldsymbol{p}_s$ depends on the local crystallography of the ferroelectric ceramic. Consider n different tetragonal domain variants $\alpha = 1, \dots, n$ whose polarization vectors are given by $\boldsymbol{R}_\alpha \boldsymbol{p}_s$, where $\boldsymbol{R}_\alpha \in SO(d)$ are admissible rotations. In two dimensions ($d = 2$) we have $n = 4$ domains, for $d = 3$ we have $n = 6$. The domains occupy volume fractions λ_α, which satisfy the constraints

$$0 \leq \lambda_\alpha \leq 1 \qquad \text{and} \qquad \sum_{\alpha=1}^{n} \lambda_\alpha = 1. \tag{2.8}$$

An *effective* or *macroscopic* polarization vector may be defined as the volume average:

$$\langle \boldsymbol{p} \rangle = \frac{1}{V} \int_\Omega \boldsymbol{p} \, \mathrm{d}v = \sum_{\alpha=1}^{n} \lambda_\alpha \, \boldsymbol{R}_\alpha \boldsymbol{p}_s. \tag{2.9}$$

Note that the constraints (2.8) along with $\boldsymbol{R}_\alpha \in SO(d)$ ensure that $|\langle \boldsymbol{p} \rangle| \leq p_s$. In phenomenological continuum models this constraint is oftentimes enforced by introducing a remanent penalty energy density [Miehe and Rosato, 2011], which is not required here.

By adopting the single-domain formulation of Section 2.2, the electric enthalpy density of domain α is now given by

$$W_\alpha(\boldsymbol{\varepsilon}^e, \boldsymbol{e}) = W_{\text{elas.},\alpha}(\boldsymbol{\varepsilon}^e, \boldsymbol{e}) + W_{\text{elec.},\alpha}(\boldsymbol{e}) \tag{2.10}$$

with the elastic and electric contributions, respectively,

$$W_{\text{elas.},\alpha}(\boldsymbol{\varepsilon}^e, \boldsymbol{e}) = \frac{1}{2} \boldsymbol{\varepsilon}^e \cdot \mathbb{C}_\alpha(\boldsymbol{e}) \, \boldsymbol{\varepsilon}^e, \qquad W_{\text{elec.},\alpha}(\boldsymbol{e}) = -\frac{\epsilon}{2} \, \boldsymbol{e} \cdot \boldsymbol{e} - \boldsymbol{e} \cdot \boldsymbol{p}_\alpha. \tag{2.11}$$

The polarization vector, remanent strains, and elastic modulus tensor of domain α are defined as, respectively,

$$\begin{aligned} &\boldsymbol{p}_\alpha = \boldsymbol{R}_\alpha \boldsymbol{p}_s, \qquad \boldsymbol{\varepsilon}^r_\alpha(\boldsymbol{e}) = \boldsymbol{R}_\alpha^\mathsf{T} \boldsymbol{\varepsilon}^r(\boldsymbol{R}_\alpha^\mathsf{T} \boldsymbol{e}, \boldsymbol{p}_s) \boldsymbol{R}_\alpha, \\ &\mathbb{C}_{\alpha,ijkl}(\boldsymbol{e}) = R_{im} \, R_{jn} \, R_{ko} \, R_{lp} \, \mathbb{C}_{mnop}(\boldsymbol{R}_\alpha^\mathsf{T} \boldsymbol{e}, \boldsymbol{p}_s) \end{aligned} \tag{2.12}$$

with the anisotropic elastic modulus tensor $\mathbb{C}$ defined in the reference domain defined by the unrotated polarization vector $\boldsymbol{p}_s$. Note that $\boldsymbol{e}$ is rotated back to the same reference state because that is where $\boldsymbol{\varepsilon}^r$ and $\mathbb{C}$ were defined.

Based on the above single-domain electric enthalpy, there are several possible choices for the *effective* enthalpy density of a poly-domain single crystal. The most prominent choices are discussed in the following.

Voigt bound (Taylor's assumption)

By assuming that each domain experiences the same total strain tensor $\boldsymbol{\varepsilon}$, the electric enthalpy density becomes the volumetric average, i.e.

$$W(\boldsymbol{\varepsilon}, \boldsymbol{e}, \boldsymbol{\lambda}) = \sum_{\alpha=1}^{n} \lambda_\alpha \, W_\alpha\big(\boldsymbol{\varepsilon} - \boldsymbol{\varepsilon}^r_\alpha(\boldsymbol{e}), \boldsymbol{e}\big). \tag{2.13}$$

This assumption implies that stresses are discontinuous across domains, which provides an upper bound on the stored strain energy density. It therefore yields a response that can be expected to be too stiff. Yet, it is conceptually and, above all, computationally convenient. Note that here and in the following we use the abbreviation $\boldsymbol{\lambda} = \{\lambda_1, \ldots, \lambda_n\}$.

The stress tensor is computed as

$$\boldsymbol{\sigma}(\boldsymbol{\varepsilon}, \boldsymbol{e}, \boldsymbol{\lambda}) = \frac{\partial W}{\partial \boldsymbol{\varepsilon}}(\boldsymbol{\varepsilon}, \boldsymbol{e}, \boldsymbol{\lambda}) = \sum_{\alpha=1}^{n} \lambda_\alpha \, \mathbb{C}_\alpha(\boldsymbol{e}) \left(\boldsymbol{\varepsilon} - \boldsymbol{\varepsilon}^r_\alpha\right), \tag{2.14}$$

so that a stress-free configuration requires

$$\boldsymbol{\varepsilon} = \left(\sum_{\beta=1}^{n} \lambda_\beta \, \mathbb{C}_\beta\right)^{-1} \sum_{\alpha=1}^{n} \lambda_\alpha \mathbb{C}_\alpha \boldsymbol{\varepsilon}^r_\alpha = \langle \mathbb{C} \rangle^{-1} \langle \boldsymbol{\sigma}^r \rangle. \tag{2.15}$$

with the average stiffness tensor and average residual stresses defined by, respectively,

$$\langle \mathbb{C} \rangle = \sum_{\beta=1}^{n} \lambda_\beta \mathbb{C}_\beta, \qquad \langle \boldsymbol{\sigma}^r \rangle = \sum_{\alpha=1}^{n} \lambda_\alpha \mathbb{C}_\alpha \boldsymbol{\varepsilon}^r_\alpha = \sum_{\alpha=1}^{n} \lambda_\alpha \boldsymbol{\sigma}^r_\alpha, \tag{2.16}$$

If only one variant α exists (i.e., $\lambda_\beta = \delta_{\alpha\beta}$), then $\boldsymbol{\varepsilon} = \boldsymbol{\varepsilon}^r_\alpha$. By contrast, if multiple elastically isotropic domains exist, then zero stresses imply $\boldsymbol{\varepsilon} = \langle \boldsymbol{\varepsilon}^r \rangle = \sum_\alpha \lambda_\alpha \boldsymbol{\varepsilon}^r_\alpha$. Note that here and in the following we drop the dependence of the elastic moduli and the remanent strains on polarization and electric field (unless when emphasizing this dependence), since these are obvious from the above definitions.

In order to compare with experimental results, it will be convenient to reformulate the above relations for the case that the total stress state is known while the total

strains are not. If an external stress $\boldsymbol{\sigma}$ is enforced, then the observed total strain (experienced by each domain) is

$$\tilde{\boldsymbol{\varepsilon}}(\boldsymbol{\sigma}, \boldsymbol{e}, \boldsymbol{\lambda}) = \langle \mathbb{C} \rangle^{-1} \left(\sum_{\alpha=1}^{n} \lambda_\alpha \mathbb{C}_\alpha \boldsymbol{\varepsilon}_\alpha^r + \boldsymbol{\sigma} \right) \tag{2.17}$$

and the effective enthalpy density follows as

$$\begin{aligned} W^*(\boldsymbol{\sigma}, \boldsymbol{e}, \boldsymbol{\lambda}) &= \sum_{\alpha=1}^{n} \lambda_\alpha \, W_\alpha \big(\tilde{\boldsymbol{\varepsilon}}(\boldsymbol{\sigma}, \boldsymbol{e}, \boldsymbol{\lambda}) - \boldsymbol{\varepsilon}_\alpha^r, \boldsymbol{e} \big) \\ &= W_0^*(\boldsymbol{e}, \boldsymbol{\lambda}) + \frac{1}{2} \boldsymbol{\sigma} \cdot \langle \mathbb{C} \rangle^{-1} \boldsymbol{\sigma} + \sum_{\alpha=1}^{n} \lambda_\alpha \, W_{\text{elec.},\alpha}(\boldsymbol{e}), \end{aligned} \tag{2.18}$$

where

$$W_0^*(\boldsymbol{e}, \boldsymbol{\lambda}) = \frac{1}{2} \sum_{\alpha=1}^{n} \lambda_\alpha \, \boldsymbol{\varepsilon}_\alpha^r \cdot \mathbb{C}_\alpha \, \boldsymbol{\varepsilon}_\alpha^r - \frac{1}{2} \langle \boldsymbol{\sigma}^r \rangle \cdot \langle \mathbb{C} \rangle^{-1} \langle \boldsymbol{\sigma}^r \rangle \tag{2.19}$$

is a strain energy contribution independent of the applied stresses or strains (the particular form (2.13) shows that strain energy is stored even if $\boldsymbol{\varepsilon} = \mathbf{0}$; likewise, an overall stress-free configuration implies stored strain energy in this formulation).

The thermodynamic driving force on volume fraction α is computed as

$$y_\alpha(\boldsymbol{\sigma}, \boldsymbol{e}, \boldsymbol{\lambda}) = -\frac{\partial W^*}{\partial \lambda_\alpha} = - W_\alpha \big(\tilde{\boldsymbol{\varepsilon}}(\boldsymbol{\sigma}, \boldsymbol{e}, \boldsymbol{\lambda}) - \boldsymbol{\varepsilon}_\alpha^r, \boldsymbol{e} \big) - \boldsymbol{\sigma} \cdot \frac{\partial \tilde{\boldsymbol{\varepsilon}}}{\partial \lambda_\alpha} \tag{2.20}$$

with

$$\begin{aligned} \frac{\partial \tilde{\varepsilon}_{ij}}{\partial \lambda_\alpha} &= \Big(\langle \mathbb{C} \rangle^{-1} \mathbb{C}_\alpha \, \boldsymbol{\varepsilon}_\alpha^r \Big)_{ij} - \langle \mathbb{C} \rangle^{-1}_{ik} \mathbb{C}_{\alpha,kl} \langle \mathbb{C} \rangle^{-1}_{nl} \left[\sum_{\alpha=1}^{n} \lambda_\alpha \, \mathbb{C}_\alpha \boldsymbol{\varepsilon}_\alpha^r - \boldsymbol{\sigma} \right]_{nj} \\ &= \left[\langle \mathbb{C} \rangle^{-1} \mathbb{C}_\alpha (\boldsymbol{\varepsilon}_\alpha^r - \boldsymbol{\varepsilon}^*) \right]_{ij}, \end{aligned} \tag{2.21}$$

where we tacitly assumed symmetric stiffness tensors and Voigt notation for simplicity of differentiation, and we use conventional index notation. Altogether, we arrive at

$$y_\alpha(\boldsymbol{\sigma}, \boldsymbol{e}, \boldsymbol{\lambda}) = - W_\alpha \left[\boldsymbol{\varepsilon}(\boldsymbol{\sigma}, \boldsymbol{e}, \boldsymbol{\lambda}) - \boldsymbol{\varepsilon}_\alpha^r, \boldsymbol{e}, \boldsymbol{p}_\alpha \right] + \boldsymbol{\sigma} \cdot \langle \mathbb{C} \rangle^{-1} \mathbb{C}_\alpha \left(\boldsymbol{\varepsilon} - \boldsymbol{\varepsilon}_\alpha^r \right) \tag{2.22}$$

and therefore in a stress-free configuration

$$y_\alpha^0(\boldsymbol{e}, \boldsymbol{\lambda}) = -\frac{1}{2} \left[\langle \mathbb{C} \rangle^{-1} \langle \boldsymbol{\sigma}^r \rangle - \boldsymbol{\varepsilon}_\alpha^r \right] \cdot \mathbb{C}_\alpha \left[\langle \mathbb{C} \rangle^{-1} \langle \boldsymbol{\sigma}^r \rangle - \boldsymbol{\varepsilon}_\alpha^r \right] + \boldsymbol{e} \cdot \boldsymbol{p}_\alpha. \tag{2.23}$$

Mixed effective formulation

A number of authors have proposed models based on effective remanent strains, polarizations, and elastic moduli and have used the effective polarization as an internal variable, see, e.g., Huber et al. [1999], Huber and Fleck [2004], Miehe and Rosato [2011], Idiart [2014]. In our formulation, this amounts to introducing effective field quantities via averaging:

$$\boldsymbol{p}_{\text{eff.}}(\boldsymbol{\lambda}) = \langle \boldsymbol{p} \rangle, \qquad \boldsymbol{\varepsilon}^r_{\text{eff.}}(\boldsymbol{e}, \boldsymbol{\lambda}) = \langle \boldsymbol{\varepsilon}^r_\alpha(\boldsymbol{e}) \rangle \qquad \text{and} \qquad \mathbb{C}_{\text{eff.}}(\boldsymbol{e}, \boldsymbol{\lambda}) = \langle \mathbb{C} \rangle\,, \tag{2.24}$$

so that an effective electric enthalpy density may be defined as

$$W(\boldsymbol{\varepsilon}, \boldsymbol{e}, \boldsymbol{\lambda}) = \frac{1}{2}(\boldsymbol{\varepsilon} - \boldsymbol{\varepsilon}^r_{\text{eff.}}) \cdot \mathbb{C}_{\text{eff.}}(\boldsymbol{\varepsilon} - \boldsymbol{\varepsilon}^r_{\text{eff.}}) - \frac{\epsilon}{2}\, \boldsymbol{e} \cdot \boldsymbol{e} - \boldsymbol{e} \cdot \boldsymbol{p}_{\text{eff.}} \tag{2.25}$$

Note that, due to linearity, the electric contribution remains unchanged from the above Voigt bound.

For a stress-based formulation we use $\boldsymbol{\sigma} = \mathbb{C}_{\text{eff.}}(\boldsymbol{\varepsilon} - \boldsymbol{\varepsilon}^r_{\text{eff.}})$ to obtain

$$W^*(\boldsymbol{\sigma}, \boldsymbol{e}, \boldsymbol{\lambda}) = \frac{1}{2}\boldsymbol{\sigma} \cdot \langle \mathbb{C} \rangle^{-1} \boldsymbol{\sigma} + \langle W_{\text{elec.},\alpha}(\boldsymbol{e}) \rangle, \tag{2.26}$$

so that stress-free conditions yield the observed total strain $\boldsymbol{\varepsilon} = \boldsymbol{\varepsilon}^r_{\text{eff.}}$. The driving force on volume fraction α is

$$y_\alpha(\boldsymbol{\sigma}, \boldsymbol{e}, \boldsymbol{\lambda}) = \frac{1}{2}\boldsymbol{\sigma} \cdot \langle \mathbb{C} \rangle^{-1} \mathbb{C}_\alpha \langle \mathbb{C} \rangle^{-1} \boldsymbol{\sigma} + \boldsymbol{e} \cdot \boldsymbol{p}_\alpha, \tag{2.27}$$

so that in a stress-free configuration the mechanical strain energy plays no role.

One may argue that this approach, though simple and intuitive, is harder to interpret physically than the others because strains and elasticities are lumped into effective average tensors. Thus, important effects such as the elastic anisotropy or strain energy stored in individual domains is accounted for only in an average sense.

Convexification-based model (Reuss bound)

The Voigt construction of Section 2.2 has a clear physical interpretation but the assumption of equal strains is too strong and the considerable amount of stored strain energy in case of zero stresses is little physical, as we will show later. As an alternative, we may introduce the relaxed electric enthalpy density

$$W(\boldsymbol{\varepsilon}, \boldsymbol{e}, \boldsymbol{\lambda}) = \inf_{\boldsymbol{\varepsilon}_1, \ldots, \boldsymbol{\varepsilon}_n} \left\{ \sum_{\alpha=1}^{n} \lambda_\alpha W_\alpha(\boldsymbol{\varepsilon}_\alpha - \boldsymbol{\varepsilon}^r_\alpha, \boldsymbol{e}) \;:\; \sum_{\alpha=1}^{n} \lambda_\alpha \boldsymbol{\varepsilon}_\alpha = \boldsymbol{\varepsilon} \right\}, \tag{2.28}$$

which includes the convex hull of the elastic strain energy density that requires minimization with respect to the domain strains $\boldsymbol{\varepsilon}_\alpha$ (for closed-form expressions see A). Note that we do not employ full convexification which would also imply minimization with respect to the domain volume fractions (those are asasumed to evolve in a dissipative manner and kinetic laws for their evolution will be discussed later).

Stationarity requires that

$$\frac{\partial W}{\partial \boldsymbol{\varepsilon}_\alpha}(\boldsymbol{\varepsilon}, \boldsymbol{e}, \boldsymbol{\lambda}) = \mathbf{0} \qquad \text{for all } \alpha = 1, \dots, n. \tag{2.29}$$

If more than one variant exists (i.e., $\lambda_\alpha \in (0,1)$ for at least one α), then we may rewrite

$$\boldsymbol{\varepsilon}_\alpha = \frac{1}{\lambda_\alpha}\boldsymbol{\varepsilon} - \sum_{\beta\neq\alpha} \frac{\lambda_\beta}{\lambda_\alpha}\boldsymbol{\varepsilon}_\beta \tag{2.30}$$

so that, by using stationarity, the stress tensor becomes (for arbitrary α with $\lambda_\alpha \neq 0$)

$$\boldsymbol{\sigma} = \frac{\partial W}{\partial \boldsymbol{\varepsilon}} = \lambda_\alpha \mathbb{C}_\alpha \frac{1}{\lambda_\alpha}\left(\frac{1}{\lambda_\alpha}\boldsymbol{\varepsilon} - \sum_{\beta\neq\alpha}\frac{\lambda_\beta}{\lambda_\alpha}\boldsymbol{\varepsilon}_\beta - \boldsymbol{\varepsilon}^r_\alpha\right) = \mathbb{C}_\alpha\left(\boldsymbol{\varepsilon}_\alpha - \boldsymbol{\varepsilon}^r_\alpha\right) = \boldsymbol{\sigma}_\alpha. \tag{2.31}$$

That is, each domain experiences the same stress tensor (viz. the applied one), which corresponds to Sach's construction of Reuss' lower bound with a uniform stress across all domains (and incompatible strains). The effective enthalpy density thus becomes

$$W^*(\boldsymbol{\sigma}, \boldsymbol{e}, \boldsymbol{\lambda}) = \frac{1}{2}\boldsymbol{\sigma} \cdot \langle \mathbb{C}^{-1} \rangle\, \boldsymbol{\sigma} + \langle W_{\text{elec.},\alpha}(\boldsymbol{e}) \rangle. \tag{2.32}$$

We observe that, as in the previous case, a stress-free configuration results in a vanishing effect of the elastic energy. If macroscopic stresses $\boldsymbol{\sigma}$ are imposed, then the observed total strain is the weighted domain average, viz.

$$\tilde{\boldsymbol{\varepsilon}}(\boldsymbol{\sigma}, \boldsymbol{e}, \boldsymbol{\lambda}) = \langle \boldsymbol{\varepsilon}_\alpha \rangle = \sum_{\alpha=1}^{n} \lambda_\alpha \left[\boldsymbol{\varepsilon}^r_\alpha + \mathbb{C}^{-1}_\alpha \boldsymbol{\sigma}\right], \tag{2.33}$$

so that in case of a stress-free configuration we recover $\boldsymbol{\varepsilon} = \langle \boldsymbol{\varepsilon}^r_\alpha \rangle$.

In analogy to the previous case, the thermodynamic driving force on volume fraction α here becomes

$$y_\alpha(\boldsymbol{\sigma}, \boldsymbol{e}, \boldsymbol{\lambda}) = -W_\alpha(\mathbb{C}^{-1}_\alpha \boldsymbol{\sigma}, \boldsymbol{e}, \boldsymbol{p}_\alpha) = -\frac{1}{2}\boldsymbol{\sigma} \cdot \mathbb{C}^{-1}_\alpha(\boldsymbol{e}, \boldsymbol{p}_\alpha)\, \boldsymbol{\sigma} + \boldsymbol{e} \cdot \boldsymbol{p}_\alpha, \tag{2.34}$$

so that in a stress-free configuration we recover the driving force (2.27).

Rank-one-convexification-based model

The above model allows for different strains across domains but does not ensure geometric compatibility across domain interfaces in the sense of Hadamard [1903]. This can be resolved by using the rank-one-convex hull of the strain energy density instead of the convex hull, see, e.g., Ball and James [1987], Bhattacharya [2003], Kochmann and Hackl [2011]. For compatibility, the enthalpy density (2.28) is amended by the additional constraint of rank-one connectivity of the individual domain strains:

$$W(\boldsymbol{\varepsilon}, \boldsymbol{e}, \boldsymbol{\lambda}) = \inf_{\substack{\boldsymbol{\varepsilon}_1,\dots,\boldsymbol{\varepsilon}_n,\\ \{\boldsymbol{a}_{\alpha\beta}\}}} \Bigg\{ \sum_{\alpha=1}^{n} \lambda_\alpha W_\alpha(\boldsymbol{\varepsilon}_\alpha - \boldsymbol{\varepsilon}^r_\alpha, \boldsymbol{e}, \boldsymbol{p}_\alpha) \;:\; \sum_{\alpha=1}^{n} \lambda_\alpha \boldsymbol{\varepsilon}_\alpha = \boldsymbol{\varepsilon} \\ \wedge\; \boldsymbol{\varepsilon}_\alpha - \boldsymbol{\varepsilon}_\beta = \boldsymbol{a}_{\alpha\beta} \otimes \boldsymbol{n}_{\alpha\beta} \;\forall\; \alpha \neq \beta \Bigg\}, \tag{2.35}$$

where $\boldsymbol{n}_{\alpha\beta}$ is the unit normal between phases α and β, which is known here from electric compatibility. 180°-domain walls are commonly parallel to the polarization, whereas 90° domain walls are known to occur under 45° angles with respect to the polarization vectors. Thus, for a given interface between domains α and β, there exist only two admissible domain wall orientations $\pm\boldsymbol{n}_{\alpha\beta}$. For conciseness we abbreviated $\{\boldsymbol{a}_{\alpha\beta}\} = \{\boldsymbol{a}_{ij} \,|\, i \neq j,\ 1 \leq i, j \leq n\}$. Rank-one-convexification in a general setting of n domain variants is cumbersome and goes beyond the efficiency envisioned for the proposed model. Therefore, we do not pursue this avenue further but include it here for completeness and to facilitate discussion. Note that more complex domain patterns can be obtained by sequential lamination [Aubry et al., 2003], resulting in higher-order laminate patterns.

Domain mixing: entropic contributions

All of the above formulations of the effective enthalpy densities of poly-domain single crystals included mechanical and electrical energy. One additional contribution that may gain importance during domain switching as well as during phase transitions is configurational entropy. We consider the entropy of mixing for n variants [Partington, 1949], viz.

$$S = -k \sum_{\alpha=1}^{n} \lambda_\alpha \log \lambda_\alpha, \tag{2.36}$$

with a material constant k (e.g., the specific gas constant times the number of moles in case of ideal gases). Here, we will interpret (2.36) as a regularizing energy

contribution with a material parameter k that governs the distribution of domains (and $k = 0$ removes all entropic contributions). The free energy density now follows as

$$F(\boldsymbol{\varepsilon}, \boldsymbol{e}, \boldsymbol{\lambda}) = W(\boldsymbol{\varepsilon}, \boldsymbol{e}, \boldsymbol{\lambda}) + k\,T \sum_{\alpha=1}^{n} \lambda_\alpha \log \lambda_\alpha \tag{2.37}$$

with T being the absolute temperature and W one of the above choices for the energy density. While stresses and strains derived above remain unaffected, the driving force on volume fraction λ_α is augmented by an entropic component:

$$q_\alpha(\boldsymbol{\varepsilon}, \boldsymbol{e}, \boldsymbol{\lambda}) = -\frac{\partial F}{\partial \lambda_\alpha}(\boldsymbol{\varepsilon}, \boldsymbol{e}, \boldsymbol{\lambda}) = y_\alpha(\boldsymbol{\varepsilon}, \boldsymbol{e}, \boldsymbol{\lambda}) - k\,T\,(\log \lambda_\alpha + 1)\,. \tag{2.38}$$

Energy-minimizing domain structures

If the domain volume fractions may change without dissipation, the equilibrium domain structure is obtained from minimization of the free energy. This is physically unrealistic but will be beneficial to review briefly in order to understand the dissipative solutions in subsequent sections.

For the particular cases of Voigt and Reuss constructions (Sections 2.2 and 2.2, respectively), the free energy density of a poly-domain single crystal has the general form

$$F(\boldsymbol{\varepsilon}, \boldsymbol{e}, \boldsymbol{\lambda}) = \sum_{\alpha=1}^{n} \lambda_\alpha \big[W_\alpha(\boldsymbol{\varepsilon}, \boldsymbol{e}) + k\,T \log \lambda_\alpha \big], \tag{2.39}$$

where the definition of W_α depends on the particular formulation for the energy density (Voigt, Reuss, etc.). It is important to note that even if the form of W_α is quite different in case of, e.g., convexification-based approaches where $W_\alpha = W_\alpha(\boldsymbol{\varepsilon}_\alpha - \boldsymbol{\varepsilon}^r_\alpha, \boldsymbol{e})$, the unifying feature of all those energy densities is that

$$\frac{\partial F}{\partial \lambda_\alpha} = W_\alpha(\boldsymbol{\varepsilon}, \boldsymbol{e}) + k\,T(\log \lambda_\alpha + 1), \tag{2.40}$$

since $\partial W_\alpha / \partial \boldsymbol{\varepsilon}_\alpha = 0$ by definition due to stationarity, see Eqs. (2.28) and (2.35).

Energy-minimizing patterns now correspond to the condensed energy density

$$F_{\text{cond.}}(\boldsymbol{\varepsilon}, \boldsymbol{e}) = \inf_{\lambda_1, \ldots, \lambda_n} \left\{ \sum_{\alpha=1}^{n} \lambda_\alpha \big[W_\alpha(\boldsymbol{\varepsilon}, \boldsymbol{e}) + k\,T \log \lambda_\alpha \big] \;:\; \text{subject to (2.8)} \right\}. \tag{2.41}$$

Enforcing constrains (2.8) can be accomplished either by the introduction of Lagrange multipliers (whose Karush-Kuhn-Tucker conditions become numerically inconvenient) or by the following trick. Let us introduce variables $E_\alpha \in \mathbb{R}$

($\alpha = 1, \ldots, n$) and define

$$\lambda_\alpha(\boldsymbol{E}) = \frac{\exp(-E_\alpha)}{\sum_{\beta=1}^{n} \exp(-E_\beta)} \tag{2.42}$$

so that constraints (2.8) are satisfied automatically. After insertion into (2.41), the minimizers $E_1^*, \ldots, E_n^*$ are obtained from stationarity:

$$\begin{aligned} \frac{\partial F}{\partial E_\alpha} &= \sum_{\beta=1}^{n} \frac{\partial F}{\partial \lambda_\beta} \frac{\partial \lambda_\beta}{\partial E_\alpha} \\ &= \sum_{\beta \neq \alpha} \left[W_\beta + kT(\log \lambda_\beta + 1) \right] \lambda_\alpha \lambda_\beta - \left[W_\alpha + kT(\log \lambda_\alpha + 1) \right] \lambda_\alpha (1 - \lambda_\alpha) = 0 \end{aligned} \tag{2.43}$$

which can be solved for

$$\lambda_\alpha^* = \frac{\exp(-W_\alpha / kT)}{\sum_{\beta=1}^{n} \exp(-W_\beta / kT)}. \tag{2.44}$$

Notice the analogy to the probability distribution of a discrete system in statistical mechanics [Partington, 1949].

Obviously, the lowest-enthalpy domain is assigned the largest volume fraction and vice-versa. Insertion of (2.44) into (2.39) yields the condensed free energy density

$$F_{\text{cond.}}(\boldsymbol{\varepsilon}, \boldsymbol{e}) = F(\boldsymbol{\varepsilon}, \boldsymbol{e}, \boldsymbol{\lambda}^*) = -kT \log \sum_{\alpha=1}^{n} \exp\left(-\frac{W_\alpha(\boldsymbol{\varepsilon}, \boldsymbol{e})}{kT} \right). \tag{2.45}$$

As discussed, the Reuss and Voigt constructions make no assumption about the spatial arrangement of ferroelectric domains, which is confirmed by the condensed energy density that does not differentiate between a collection of domains at the same level or domains organized in a hierarchical fashion, see B.

The solution (2.45) highlights the influence of the entropic term. Rewriting (2.44) as

$$\lambda_\alpha^* = \frac{1}{1 + \sum_{\beta \neq \alpha} \exp\left(-\frac{W_\beta - W_\alpha}{kT} \right)} \tag{2.46}$$

shows that in the limit of $kT \to 0$ only one domain (with the lowest energy) or a uniform mixture of domains (in case of equal energies) survives:

$$\lim_{kT \to 0} \lambda_\alpha^* = \begin{cases} 1, & \text{if } W_\beta > W_\alpha \text{ for all } \beta \neq \alpha, \\ 0, & \text{if there is at least one } W_\beta < W_\alpha, \\ 1/n, & \text{if all } n \text{ energies are equal: } W_\beta = W_\alpha \forall\, \beta. \end{cases} \tag{2.47}$$

In the opposite limit of large values of kT, we expect a uniform domain mixture irrespective of the individual domain energies since

$$\lim_{kT\to\infty} \exp\left(-\frac{W_\beta - W_\alpha}{kT}\right) = 1 \qquad \Rightarrow \qquad \lim_{kT\to\infty} \lambda_\alpha^* = \frac{1}{n}. \tag{2.48}$$

Domain switching

The above framework only applies if the domain switching process is elastic and does not involve dissipation. However, the motion of domain walls (as well as the nucleation of domains) dissipates energy, so that volume fractions λ_α ($\alpha = 1, \dots, n$) change in a dissipative manner. Let us write the associated kinetic law as [Biot, 1965, Ortiz and Stainier, 1999, Carstensen et al., 2002]

$$\frac{\partial F}{\partial \lambda_\alpha} + \frac{\partial \phi^*}{\partial \dot{\lambda}_\alpha} = 0, \tag{2.49}$$

where ϕ^* is the dual (kinetic) potential which we assume to be continuously differentiable to account for rate-dependent behavior without hard thresholds (otherwise, (2.49) is to be replaced by a differential inclusion). In this case, the above evolution law can be cast into variational form, viz.

$$\dot{\lambda}_\alpha = \arg\min \left\{ \dot{F} + \phi^* \right\}. \tag{2.50}$$

A temporal discretization is introduced which assumes constant time increments $t_{j+1} - t_j = \Delta t$ so that $\boldsymbol{\lambda}_j = \boldsymbol{\lambda}(t_j) = \boldsymbol{\lambda}(j\,\Delta t)$ and $t_0 = 0$. Following Ortiz and Stainier [1999] and writing $\boldsymbol{\lambda}_{j+1} = \boldsymbol{\lambda}_j + \Delta\boldsymbol{\lambda}$, the evolution of $\boldsymbol{\lambda} = \{\lambda_1, \dots, \lambda_n\}$ is thus governed by

$$\Delta\boldsymbol{\lambda} = \arg\min \left\{ F(\boldsymbol{\lambda}_j + \Delta\boldsymbol{\lambda}) - F(\boldsymbol{\lambda}_j) + \Delta t\, \phi^* \left(\frac{\Delta\boldsymbol{\lambda}}{\Delta t} \right) \right\}, \tag{2.51}$$

which motivates the definition of the incremental potential

$$\mathcal{F}(\boldsymbol{\lambda}_{j+1}, \boldsymbol{\lambda}_j) = F(\boldsymbol{\lambda}_{j+1}) + \Delta t\, \phi^* \left(\frac{\boldsymbol{\lambda}_{j+1} - \boldsymbol{\lambda}_j}{\Delta t} \right), \tag{2.52}$$

where we dropped the energy $F(\boldsymbol{\lambda}_j)$ at the old time step since it does not affect the minimization with respect to $\boldsymbol{\lambda}_{j+1}$ (and we also omitted the explicit dependence of $\mathcal{F}$ on all other fields for brevity). Now, the incremental updates of the volume fractions follow from

$$\Delta\boldsymbol{\lambda} = \arg\min \mathcal{F}(\boldsymbol{\lambda}_j + \Delta\boldsymbol{\lambda}, \boldsymbol{\lambda}_j). \tag{2.53}$$

Domain switching in ferroelectrics is an intricate process governed by the domain wall kinetics. Theoretical insight and experimental evidence confirm differences in

the kinetics of 90°- vs. 180°-domain wall motion. In particular, 180°-domain walls display a significantly-higher resistance to motion than 90°-domain walls under applied electric fields [Liu et al., 2016]. To properly account for such phenomena, consider an increment $\Delta\lambda_{\alpha\beta}$ which denotes the volume fraction whose polarization $\boldsymbol{R}_\alpha \boldsymbol{p}_s$ is changing into $\boldsymbol{R}_\beta \boldsymbol{p}_s$. Consequently $\Delta\lambda_{(\alpha\alpha)} = 0$ and $\Delta\lambda_{\alpha\beta} = -\Delta\lambda_{\beta\alpha}$, also

$$\lambda_{\alpha,j+1} = \lambda_{\alpha,j} + \sum_{\beta\neq\alpha} \Delta\lambda_{\alpha\beta}. \tag{2.54}$$

To differentiate between 90°- and 180°-domain wall motion, let us define the dual potential

$$\phi^* = \sum_{(\alpha,\beta)\in\mathcal{S}_1} \frac{\eta_1 \dot{\lambda}_1}{m_1+1} \left(\frac{|\Delta\lambda_{\alpha\beta}|}{\dot{\lambda}_1 \, \Delta t} \right)^{m_1+1} + \sum_{(\alpha,\beta)\in\mathcal{S}_2} \frac{\eta_2 \dot{\lambda}_2}{m_2+1} \left(\frac{|\Delta\lambda_{\alpha\beta}|}{\dot{\lambda}_2 \, \Delta t} \right)^{m_2+1}, \tag{2.55}$$

where $\mathcal{S}_1$ and $\mathcal{S}_2$ denote all pairs (α,β) whose transition corresponds to 90°- and 180°-domain wall motion, respectively, and the associated kinetic parameters also carry subscripts 1 and 2. η_i and $\dot{\lambda}_i$ are viscosities and reference rates, respectively, and m_i represent the corresponding rate sensitivity exponents, see, e.g., Miehe and Rosato [2011].

Together with (2.54) and (2.55), (2.53) now defines the incremental kinetic updates (for $\alpha,\beta = 1,\dots,n$ and $\alpha \neq \beta$)

$$\Delta\lambda_{\alpha\beta} = \arg\min \mathcal{F}(\boldsymbol{\lambda}_j + \Delta\boldsymbol{\lambda}, \boldsymbol{\lambda}_j), \tag{2.56}$$

which, exploiting (2.54), translates into the kinetic relation for $\Delta\lambda_{\alpha\beta} = -\Delta\lambda_{\beta\alpha}$:

$$\sum_{\alpha\neq\beta} \frac{\partial F}{\partial \lambda_\alpha} \frac{\partial \lambda_\alpha}{\partial \Delta\lambda_{\alpha\beta}} - \sum_{\beta\neq\alpha} \frac{\partial F}{\partial \lambda_\beta} \frac{\partial \lambda_\beta}{\partial \Delta\lambda_{\beta\alpha}} + \Delta t \, \frac{\partial \phi^*}{\partial \Delta\lambda_{\alpha\beta}} = 0. \tag{2.57}$$

Following analogous strategies as in Section 2.2 for energy minimization, the above flow rule finally leads to (for both the Reuss and Voigt constructions; if $\Delta\lambda_{\alpha\beta} \neq 0$)

$$W_\alpha + kT \log \lambda_\alpha - \left(W_\beta + kT \log \lambda_\beta \right) + \eta_i \left(\frac{|\Delta\lambda_{\alpha\beta}|}{\dot{\lambda}_i \, \Delta t} \right)^{m_i} \operatorname{sign}(\Delta\lambda_{\alpha\beta}) = 0 \tag{2.58}$$

for all $\alpha,\beta = 1,\dots,n$. Note that in case of the mixed energy formulation of Section 2.2, the above form requires changes since (2.40) no longer applies and the driving force must be modified.

For uniqueness, we solve only for those updates $\Delta\lambda_{\alpha\beta}$ with $\alpha < \beta$. An explicit solution strategy, e.g., results in the incremental updates

$$\Delta\lambda_{\alpha\beta} = \dot{\lambda}_i \, \Delta t \left[\frac{|q_\alpha - q_\beta|}{\eta_i} \right]^{\frac{1}{m_i}} \operatorname{sign}(q_\alpha - q_\beta) \tag{2.59}$$

with $q_\alpha = -\partial F/\partial \lambda_\alpha = -W_\alpha - kT(\log \lambda_\alpha + 1)$.

As an example, consider the motion of a particular domain wall, i.e., we assume there are only two domains active in a particular grain. Assume a domain switching process with $\lambda_{\alpha\beta} > 0$. The domain wall motion is governed by

$$\frac{\Delta \lambda_{\alpha\beta}}{\Delta t} = \dot{\lambda}_i \left\{ \frac{1}{\eta_i} \left[W_\beta - W_\alpha + kT \log \left(\frac{\lambda_\beta}{\lambda_\alpha} \right) \right] \right\}^{\frac{1}{m_i}} . \tag{2.60}$$

If the body is approximately stress-free and the volume fractions are approximately equal ($\lambda_\alpha \approx \lambda_\beta$), then this reduces to

$$\frac{\Delta \lambda_{\alpha\beta}}{\Delta t} = \dot{\lambda}_i \left[\frac{\epsilon}{2\eta_i} \boldsymbol{e} \cdot (\boldsymbol{p}_\alpha - \boldsymbol{p}_\beta) \right]^{\frac{1}{m_i}} \tag{2.61}$$

If $m_i = 1$ this yields the gradient flow model often assumed in phase field theory for ferroelectrics [Zhang and Bhattacharya, 2005a,b, Su and Landis, 2007, Chen et al., 2008, Nadkarni et al., 2016]:

$$\frac{\eta_i}{\dot{\lambda}_i} \frac{\Delta \lambda_{\alpha\beta}}{\Delta t} = -\frac{\epsilon}{2} \boldsymbol{e} \cdot (\boldsymbol{p}_\beta - \boldsymbol{p}_\alpha). \tag{2.62}$$

Finally, note that specific details of the domain wall kinetics can be incorporated into the above framework by adjusting the reference wall speed $\dot{\lambda}_i$. For example, the experimentally-observed Merz law [Merz, 1956] for the electric-field dependence of the average domain wall speed along with the temperature dependence of domain wall motion can be reproduced by defining, e.g.,

$$\dot{\lambda}_i(T, \boldsymbol{e}, \boldsymbol{p}) = \dot{\lambda}_{i,0} \exp \left(-\frac{e_{i,0}(T)}{|\boldsymbol{e} \cdot \boldsymbol{p}|} \right) \tag{2.63}$$

with a thermal activation energy $e_{i,0}$.

Phase Transformation

The above constitutive model can be extended to describe the temperature-induced structural transitions in ferroelectric ceramics (although not the focus here). For example, the martensitic, second-order transformation from the (polar) tetragonal to the (non-polar) cubic phase at the Curie temperature (for PZT near $T_c = 308°\mathrm{C}$ [Jona and Shirane, 1962]) can be modeled by including one additional volume fraction, viz. that of the high-temperature cubic phase which is characterized by $\boldsymbol{\varepsilon}^r_{\text{cubic}} = \boldsymbol{0}$ and $\boldsymbol{p}_{\text{cubic}} = \boldsymbol{0}$ as well as an isotropic incremental tangent tensor $\mathbb{C}_{\text{cubic}}$. The single crystal free energy density is now defined as

$$F(\cdot, \boldsymbol{e}, \boldsymbol{\lambda}, T) = \sum_{\alpha=1}^{n+1} \lambda_\alpha \left[W_\alpha(\cdot, \boldsymbol{e}) + kT \log \lambda_\alpha + \Psi_\alpha(T) \right]. \tag{2.64}$$

Ψ_α is the chemical potential of variant α, which is the same for all tetragonal variants ($\Psi_\alpha = \Psi_{\text{tetr.}}(T)$) but different for the cubic phase ($\Psi_\alpha = \Psi_{\text{cubic}}(T)$). Obviously, for $T > T_c$ we must have $\Psi_{\text{cubic}} < \Psi_{\text{tetr.}}$, and for $T < T_c$ physics demands that $\Psi_{\text{cubic}} > \Psi_{\text{tetr.}}$

If no electric field is applied and the body is stress-free, energy minimization leads to a sharp phase transition at T_c. That is, above the transition temperature the entire crystal is in its non-polar cubic phase, whereas below the Curie point the crystal breaks into tegragonal domains of equal volume fractions if no bias electric field is applied. Thus, we see a volumetric change in the remanent strain which is $\boldsymbol{\varepsilon}^r = \mathbf{0}$ if $T \geq T_c$ and $\boldsymbol{\varepsilon}^r = \langle \boldsymbol{\varepsilon}^r_\alpha \rangle$ if $T < T_c$.

In reality, the phase transition is dissipative, leading to hysteresis. To this end, we introduce an additional dual (dissipation) potential $\phi^*_{\text{trans.}}$ that only accounts for volume fraction changes from the high-temperature phase ($n + 1$) to the low-temperature variants $(1, \ldots, n)$, viz.

$$\phi^*_{\text{trans.}} = \sum_{\alpha=1}^{n} \Psi_{\text{trans}} \left(\frac{\Delta \lambda_{n\alpha}}{\Delta t} \right). \tag{2.65}$$

Polycrystalline ferroelectrics

Having established the theoretical framework for single crystals, we extend the above model to polycrystalline ferroelectrics. Consider a polycrystal containing n_{G} grains, each of which being composed of, in principle, $n = 2d$ domains (in d dimensions), each described by the above single crystal model. Let the grain orientations be defined by rotations $\boldsymbol{R}^{\text{G}}_i \in SO(d)$ $(i = 1, \ldots, n_{\text{G}})$. To model the effective response of the polycrystalline aggregate, we choose a simple Taylor model analogous to Section 2.2, i.e., we assume that the effective response is the average across all grains which are subjected to the same strains and electric fields. The obtained effective material behavior will only present an upper bound to the actual response, but it is a numerically-efficient approximation commonly employed in, e.g., models of polycrystal plasticity [Chang and Kochmann, 2015]. The total free energy of the polycrystal is thus

$$W(\boldsymbol{\varepsilon}, \boldsymbol{\lambda}, \boldsymbol{e}) = \frac{1}{n_{\text{G}}} \sum_{i=1}^{n_{\text{G}}} \left[\sum_{\alpha=1}^{n} \lambda_{i,\alpha} W_\alpha(\boldsymbol{\varepsilon}, \boldsymbol{e}) + kT \lambda_{i,\alpha} \log \lambda_{i,\alpha} \right] \tag{2.66}$$

where $\lambda_{i,\alpha}$ denotes the volume fraction of domain α inside grain i. (We note that a Reuss-type lower bound can be constructed analogously.) The overall constitutive

model thus uses the constant-strain Taylor model for the polycrystal, while the domain behavior within each grain follows the constant-stress Reuss bound.

In the polycrystal shown in Fig. 2.1, we now have remanent strains and polarizations given by, respectively,

$$\boldsymbol{\varepsilon}^r_{i,\alpha} = \boldsymbol{R}^{\mathrm{G}}_i \boldsymbol{\varepsilon}^r_\alpha \left(\boldsymbol{R}^{\mathrm{G}}_i\right)^{\mathsf{T}} = \boldsymbol{R}^{\mathrm{G}}_i \boldsymbol{R}_\alpha \, \boldsymbol{\varepsilon}^r(\boldsymbol{p}_s) \left(\boldsymbol{R}^{\mathrm{G}}_i \boldsymbol{R}_\alpha\right)^{\mathsf{T}} \qquad \text{and} \qquad \boldsymbol{p}_{i,\alpha} = \boldsymbol{R}^{\mathrm{G}}_i \boldsymbol{R}_\alpha \boldsymbol{p}_s . \tag{2.67}$$

In order to simulate domain switching, we resort to the same kinetic laws of Section 2.2. Here, the evolution equations for the domain volume fractions are applied within each grain individually, and the effective response is obtained from averaging over all grains. This allows us to solve the variational problem within each grain independently and thus more efficiently.

2.3 Material-specific model parameters and relations

The theory summarized in the previous sections was for general ferroelectrics and free of material-specific assumptions. Here, we introduce formulations specific to ferroelectric ceramics of the perovskite crystal structure such as barium titanate ($BaTiO_3$) or lead zirconate titanate (PZT). These have an unpolar cubic structure above the Curie temperature and a tetragonal or rhombohedral-tetragonal structure, respectively, at lower temperature. The model so far has been sufficiently general and we make the following specifications only with the aim of presenting numerical results for the response of (tetragonal) PZT polycrystals.

We assume the link between remanent strain and polarization within a domain to be given by

$$\boldsymbol{\varepsilon}^r(\boldsymbol{p}, \boldsymbol{e}) = \left[\left(\alpha_{||} + \alpha_\perp\right) \frac{\boldsymbol{p}}{p_s} \otimes \frac{\boldsymbol{p}}{p_s} - \alpha_\perp \boldsymbol{I} \right] \left(1 + \xi \, \frac{\boldsymbol{e}}{e_c} \cdot \frac{\boldsymbol{p}}{p_s} \right), \tag{2.68}$$

where the last term can be linked to the piezoelectric strain coefficients by

$$h_{ijk} = \frac{\partial \varepsilon^r_{ij}}{\partial e_k} = \frac{1}{e_c} \left[\left(\alpha_{||} + \alpha_\perp\right) \frac{p_i \, p_j}{p_s^2} - \alpha_\perp \delta_{ij} \right] \xi \, \frac{p_k}{p_s}. \tag{2.69}$$

$\alpha_{||}$ and $\alpha_\perp$ are strain-coupling constants [Miehe and Rosato, 2011] such that the spontaneous strains in the absence of an applied electric field are given by $\alpha_{||}$ and $-\alpha_\perp$ parallel and perpendicular to the direction of polarization, respectively. e_c is the coercive electric field. Note that e_c appears merely as a scaling parameter (it could alternatively be absorbed into the constant ξ), so that the experimentally-observed coercive field is not an input to the model but will be a model outcome.

For example, if the domain is poled in the x_3-direction (i.e., $\boldsymbol{p} = p_s \boldsymbol{e}_3$) the remanent strain–electric field relation in Voigt notation becomes

$$\begin{bmatrix} \varepsilon_{11} \\ \varepsilon_{22} \\ \varepsilon_{33} \\ \varepsilon_{12} \\ \varepsilon_{13} \\ \varepsilon_{23} \end{bmatrix} = \begin{bmatrix} 0 & 0 & -\alpha_\perp \xi \\ 0 & 0 & -\alpha_\perp \xi \\ 0 & 0 & \alpha_{||} \xi \\ 0 & 0 & 0 \\ 0 & 0 & 0 \\ 0 & 0 & 0 \end{bmatrix} \begin{bmatrix} e_1 \\ e_2 \\ e_3 \end{bmatrix}, \tag{2.70}$$

and we may conclude that the piezoelectric constants are determined from

$$d_{31} = d_{32} = -\alpha_\perp \xi, \qquad d_{33} = \alpha_{||} \xi. \tag{2.71}$$

Obviously, the above form neglects shear strains arising from applied electric fields ($d_{15} = d_{24} = 0$). Since the shear strains are small compared to the longitudinal and transverse components and because we are primarily interested in the ferroelectric phenomena, one may justify this assumption for many practical scenarios. A refined formulation can be found, e.g., in Miehe and Rosato [2011]; here, this would require changing the coupling term in (2.68) without significant complication.

For a tetragonal crystal structure the six domain variants in three dimensions are defined by the rotations

$$\begin{aligned} \boldsymbol{R}_1 &= \begin{pmatrix} 1 & 0 & 0 \\ 0 & 1 & 0 \\ 0 & 0 & 1 \end{pmatrix}, \qquad \boldsymbol{R}_2 = \begin{pmatrix} -1 & 0 & 0 \\ 0 & -1 & 0 \\ 0 & 0 & 1 \end{pmatrix}, \\ \boldsymbol{R}_3 &= \begin{pmatrix} \cos \pi/2 & \sin \pi/2 & 0 \\ -\sin \pi/2 & \cos \pi/2 & 0 \\ 0 & 0 & 1 \end{pmatrix}, \qquad \boldsymbol{R}_4 = \begin{pmatrix} \cos \pi/2 & -\sin \pi/2 & 0 \\ \sin \pi/2 & \cos \pi/2 & 0 \\ 0 & 0 & 1 \end{pmatrix}, \\ \boldsymbol{R}_5 &= \begin{pmatrix} \cos \pi/2 & 0 & \sin \pi/2 \\ 0 & 1 & 0 \\ -\sin \pi/2 & 0 & \cos \pi/2 \end{pmatrix}, \qquad \boldsymbol{R}_6 = \begin{pmatrix} \cos \pi/2 & 0 & -\sin \pi/2 \\ 0 & 1 & 0 \\ \sin \pi/2 & 0 & \cos \pi/2 \end{pmatrix}. \end{aligned} \tag{2.72}$$

The rotation matrices associated with the grain orientations are generally arbitrary and can be generated from experimental pole figures or from a known mean orientation and standard deviation (as in some of the following simulations).

A list of all material parameters used in subsequent simulations is summarized in Table 2.1 along with the relevant references. The only material parameters that

C_{11}	211.7 GPa [Li et al., 1991]	m_1	2
C_{12}	107.4 GPa [Li et al., 1991]	m_2	0
C_{13}	114.7 GPa [Li et al., 1991]	η_1	5
C_{33}	160.6 GPa [Li et al., 1991]	η_2	1
C_{44}	56.2 GPa [Li et al., 1991]	$\dot{\lambda}_1$	2000
C_{66}	126.4 GPa [Li et al., 1991]	$\dot{\lambda}_2$	0
$d_{31} = d_{32}$	−50 pC/N [Li et al., 1991]	k	$3.0 \cdot 10^{-6}$
d_{33}	106 pC/N [Li et al., 1991]	ξ	$6.436 \cdot 10^{-9}$
d_{15}	580 pC/N [Li et al., 1991]	e_c	0.5 MV/m [Huber and Fleck, 2004]
p_s	26 μC/cm^2 [Burcsu, 2001]	$\varepsilon_s^{\parallel *}$	0.82% [Burcsu, 2001]
ϵ	36.3 nF/m [Li et al., 1991]	$\varepsilon_s^{\perp *}$	−0.27% [Burcsu, 2001]

Table 2.1: Room-temperature $BaTiO_3$ material parameters used in all simulations (parameters without citation were obtained by fitting to experimental data); *under stress-free conditions and zero strains otherwise.

cannot directly be obtained from experimental or theoretical data are those associated with the kinetic laws (i.e., viscosities, reference rates, and rate sensitivity exponents) as well as the entropic coefficient k.

2.4 Representative results and comparison to experiments

We apply the constitutive model to single- and polycrystalline $BaTiO_3$ under combined electro-mechanical loading, for which numerical results can be compared to experimental data of, e.g., Shieh et al. [2009].

Electrical hysteresis, strain hysteresis and dissipation

Applying an electric field to an unconstrained sample results in the well-known electrical hysteresis and associated butterfly curve illustrating the remanent strain during each cycle. Damping caused by energy dissipation from domain wall motion is a measurable indicator of domain-switching kinetics [Wojnar et al., 2014, Le Graverend et al., 2015].

Single crystal

We apply the single crystal constitutive model described above (using the Sachs lower-bound construction for the domain mixture) to describe a six-domain $BaTiO_3$ sample under stress-free conditions. Figure 2.2 shows the simulated electromechanical response of $BaTiO_3$ single crystals whose c-axes are tilted at different angles with respect to an applied electric field in the x-direction. The electric field ampli-

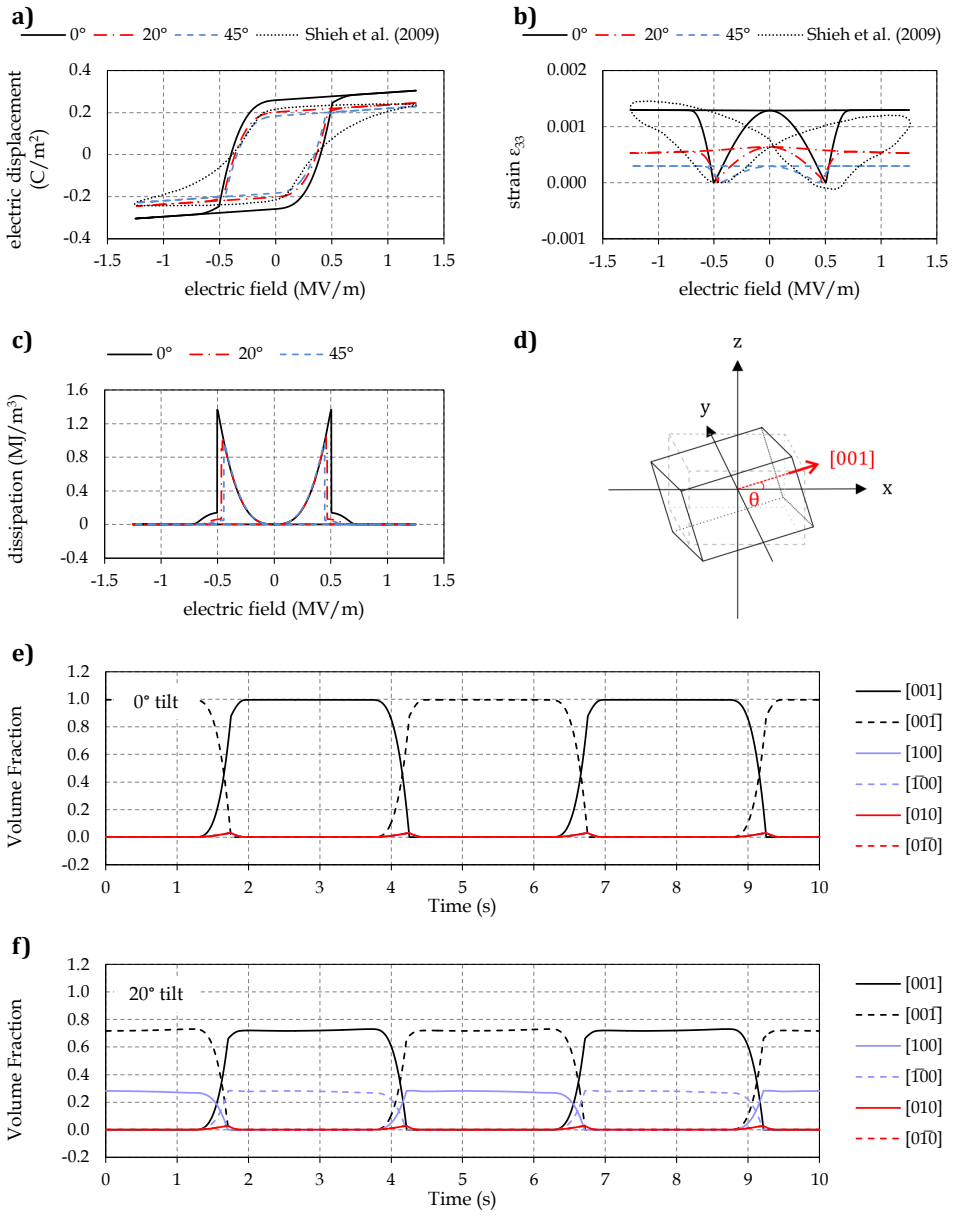

Figure 2.2: a) Electrical hysteresis, b) strain hysteresis and c) dissipation of single-crystalline $BaTiO_3$ at c-axis tilts θ of 0°, 20° and 45° with respect to the applied electric field direction. Dotted lines in a) and b) show experimental single crystal data by Shieh et al. [2009]; d) illustrates the tilt angle. e) and f) show the domain evolution of an untilted and a 20°-tilted crystal, respectively.

tude of ±1.25 MV/m and frequency of 0.2 Hz were chosen to mimic experimental conditions of Shieh et al. [2009]. Kinetic parameters were chosen to give the best fit to the experimentally measured behavior in Shieh et al. [2009] (fitting was performed with respect to the best mean deviation of both full electrical and mechanical hystereses). Interestingly, it appears that the best fit is attained from pure 90°-domain switching with little to no direct 180°-switching (as apparent in Table 2.1 from the choice $m_2 = 0$ and $\dot{\lambda}_2 = 0$). One may indeed expect the 180°-domain wall mobility to be lower than that of 90°-walls, which is reflected by this choice. (We note that the chosen material parameters are the result of fitting to experimental data and hence not necessarily unique.)

Computed electrical hystereses and butterfly curves are shown in Figure 2.2a) and b). The saturated electric displacement and the maximum remanent strain drop dramatically between a fully-aligned and a 20°-tilted sample, with minimal decrease upon further tilting to 45°. This is visualized by the plot of domain volume fractions vs. time in Figure 2.2e) and f), where a 20°-tilt results in an approximately 30-70% distribution between [001] and [100] domains at maximum electric field.

Figure 2.2c illustrates the energy dissipation caused by domain switching, which peaks just beyond the coercive field, at the point where electric displacement saturates. This qualitative behavior closely corresponds to experimental measurements of damping in PZT using Broadband Electromechanical Spectroscopy (BES) by Wojnar et al. [2014] and Le Graverend et al. [2015] as seen in Figure 2.3d; unfortunately, no such experimental measurements have yet been performed for $BaTiO_3$ but the qualitative behavior is expected to be the same.

Polycrystal

Unlike in the case of the single crystal, decreasing the degree of texturing in the polycrystal greatly reduces the width of the electric displacement hysteresis curve, as seen in Figure 2.3. The smaller coercive field indicates that switching occurs more readily, which is attributed to the significant internal mechanical stresses that arise at grain boundaries and from domain switching of grains of different tilts. The butterfly curves also have greater curvature compared to the single crystal case, as switching occurs gradually over a larger range of applied electric field strengths due to the different grain orientations. However, the overall conclusion that the greater the grain misorientation, the smaller the maximum remanent strain, remains valid.

In reality, most ferroelectric devices are polycrystalline and fairly untextured. To

explore the difference in ferroelectric response due to texturing in polycrystals, we simulate a polycrystal containing 100 grains of random orientations within a tilt cone of $0-45°$. The distribution of orientations is given in the pole figures of Figure 2.4. We chose a volume element with 100 grains as representative to sufficiently capture the averaging effect of random orientations while maintaining efficiency. Figure 2.5 shows the convergence of the polycrystal behavior with increasing number of grains in the simulation, indicating only little deviation beyond 100 grains.

Finally, the dissipated energy in the polycrystal (shown in Figure 2.4c) decreases sharply with decreasing texture, indicating that the sample retains much of its energy in the form of internal constraints instead of dissipating it, as in the case of the unconstrained single crystal. Peak height drops by 70% with just a 10° random off-axis tilt, and peaks gradually become flatter as texture decreases. Overall, the observed variation of the dissipation vs. applied electric field qualitatively matches experimental findings for PZT [Wojnar et al., 2014, Le Graverend et al., 2015].

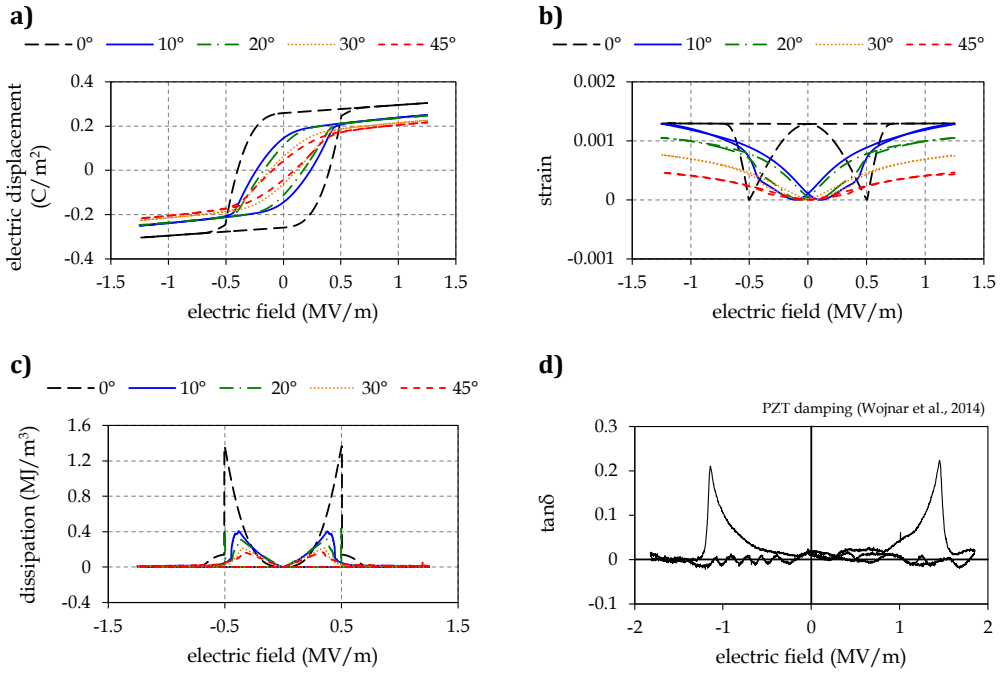

Figure 2.3: a) Electrical hysteresis, b) strain hysteresis and c) dissipation of polycrystalline $BaTiO_3$ simulated with 100 grains of random orientation within cones of various angles. d) Experimental measurements of damping (viscoelastic loss tangent) in polycrystalline PZT by Wojnar et al. [2014] shows qualitatively similar behavior to calculated dissipation curves.

Stress-dependent domain switching

Experiments have revealed a strong influence of applied compressive stresses on the domain switching mechanisms, see, e.g., Chaplya and Carman [2002a,b], Shieh et al. [2009]. Here, we investigate the stress-dependent electromechanical material response of the model described above.

Single crystal

We use the same parameters as for the single crystal in Section 2.4 and apply a compressive pre-stress ranging from 0 MPa to 1.5 MPa. Figure 2.6b) shows a clear increase in remanent strain with increasing precompression. The magnitude of the strain also corresponds well with experimental results by Shieh et al. [2009]. In our simulation, the maximum remanent strains at 1.0 MPa and 1.5 MPa precompression are, respectively, 0.21% and 0.33%, while experiments on $BaTiO_3$ single crystals showed 0.21% and 0.39% for precompression levels of 0.9 MPa and 1.7 MPa.

Further, we note in Figure 2.6c) and d) that damping peaks decrease slightly with precompression, but have wider tails beyond the coercive field due to a retention of 90°-switched states caused by the compression, which require larger electric fields

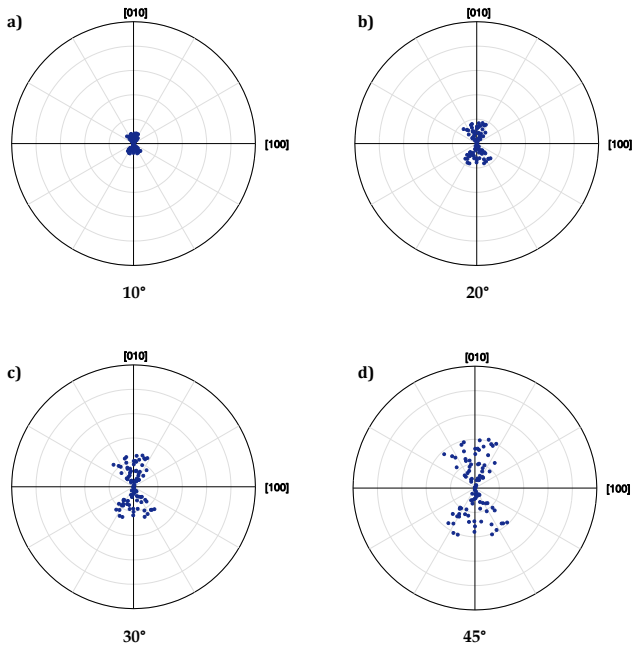

Figure 2.4: Distribution of grain orientations in simulated polycrystal.

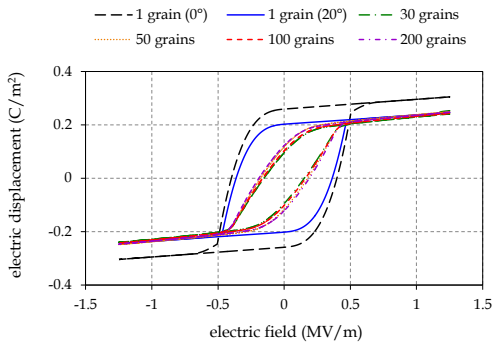

Figure 2.5: Comparison of the electrical hystereses obtained from simulations with different numbers of grains. All grains are randomly oriented within a 20° cone similar to the distribution shown in Figure 2.4b.

to overcome.

Polycrystal

In contrast to the pronounced effect of precompression on the strain behavior in single crystals, the polycrystalline case shows minimal change in electric displacement, strain hysteresis and energy dissipation. Figure 2.7 shows results for a polycrystal with 100 grains at random tilts within a 20°-cone. The data show that the trend of decreasing electric displacement hysteresis width and increasing remanent strain with increasing precompression still exists for polycrystals, but it is much less pronounced. This is consistent with the observation that fine-grained $BaTiO_3$ has smaller d_{33}-dependence on precompression than coarse-grained $BaTiO_3$ [Damjanovic and Demartin, 1997] (unfortunately, no experimental data showing precompressed results for bulk polycrystalline $BaTiO_3$ are available).

Boundary value problems via finite elements

The constitutive framework outlined above is sufficiently efficient for its implementation in finite element (FE) simulations. Therefore, going beyond the previous material point calculations, we now use the same model in an FE framework to solve electro-mechanically-coupled boundary value problems. We use a variational in-house code that uses trilinear brick elements with mixed nodal degrees of freedom to discretize the displacement and electric potential fields in three dimensions. The coupled governing equations are solved implicitly (using Newton-Raphson iteration) for the electric and mechanical fields, whereas the domain volume fractions

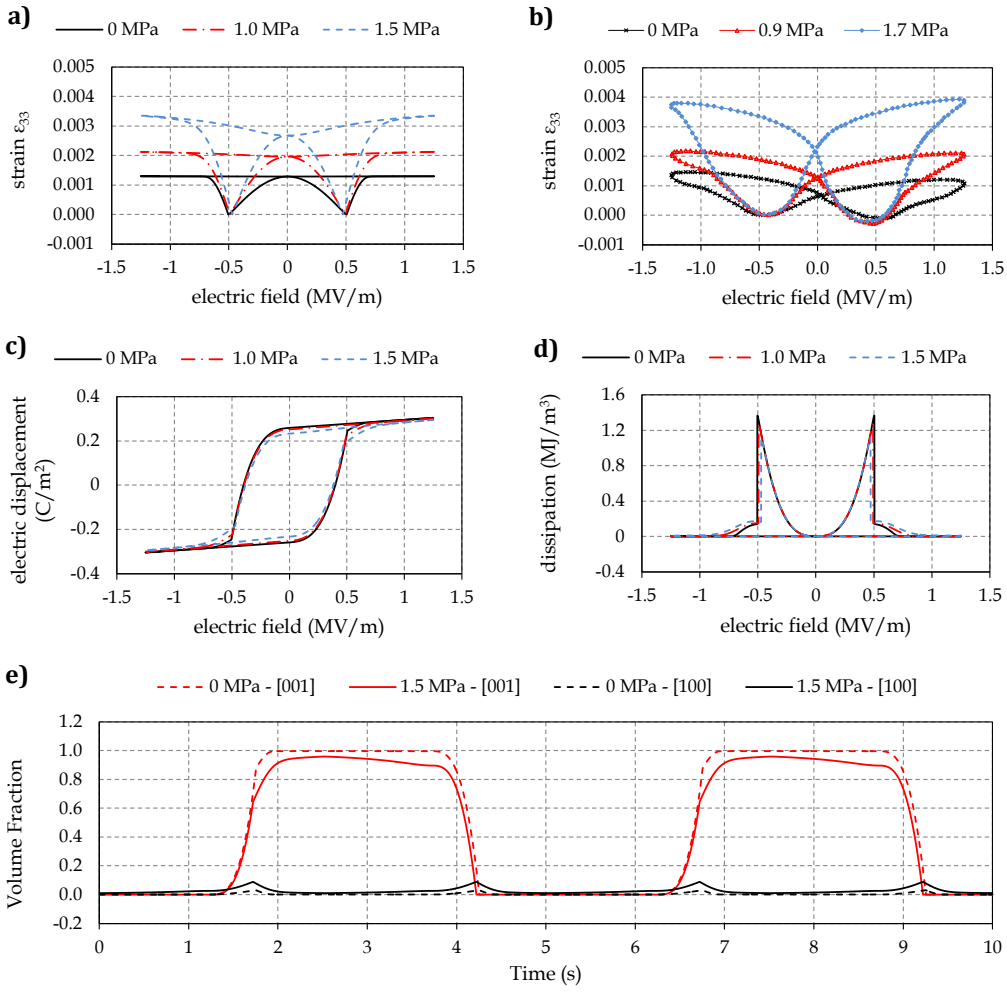

Figure 2.6: a) Calculated strain, b) experimental strain hysteresis data by Shieh et al. [2009] for comparison, c) calculated electrical hysteresis, and d) calculated energy dissipation of unrotated single crystalline $BaTiO_3$ at precompression levels of 0 MPa, 0.5 MPa and 1.5 MPa. e) shows the domain evolution in an untilted crystal with precompression (solid line) and without (dashed).

are updated explicitly in a staggered manner after electro-mechanical equilibration. For sufficiently small time steps (as those chosen here), this is legitimate and converges since all fields vary sufficiently slowly so that electrical and mechanical fields may be assumed to evolve quasistatically (we use a time step of 10^{-4} s and a rate of 0.2 Hz).

We choose the example of a cantilever beam (dimensions $1 \times 3 \times 15$ mm) clamped at the bottom up to 20% of its length, which reproduces the configuration of sam-

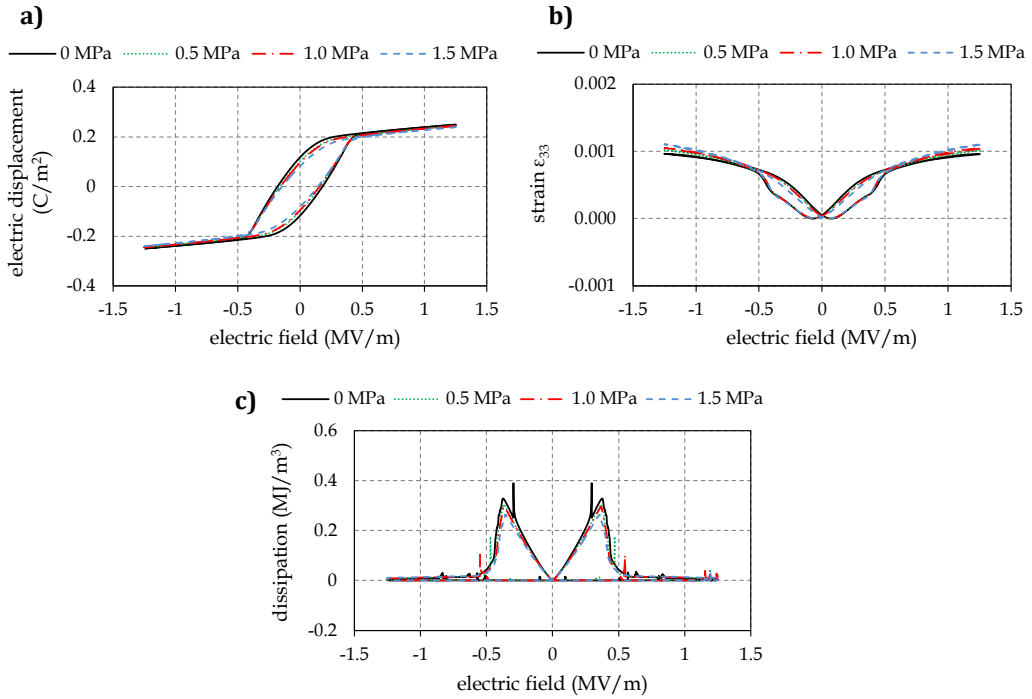

Figure 2.7: a) Electrical hysteresis, b) strain hysteresis and c) dissipation of polycrystalline $BaTiO_3$ under precompression, simulated with 100 grains of random orientations within a 20°-misorientation cone.

ples used for BES measurements [Wojnar et al., 2014, Le Graverend et al., 2015]. Fig. 2.8 illustrates the effective electric hysteresis and butterfly curve as obtained from averaging over the whole specimen along with visualizations of the stress and strain distributions at different stages of the electric hysteresis. The clamping inhibits displacements of the surfaces in contact with the clamp, hence reducing domain switching and causing a sharp increase in strain at the transition between the clamped and the free surface, as seen in Figure 2.8. Thus, the overall magnitude of electric displacements and remanent strains across the sample during cyclic electric field loading is reduced compared to an unconstrained sample (dotted line), but the shape remains unchanged. Also visible is the impact of the clamped boundary conditions onto the effective sample response as compared to a free-standing sample (which is important information for the interpretation of BES results).

2.5 Conclusions

We have presented a constitutive model for polycrystalline ferroelectric ceramics and applied it to simulate the response of single- and polycrystalline barium titanate

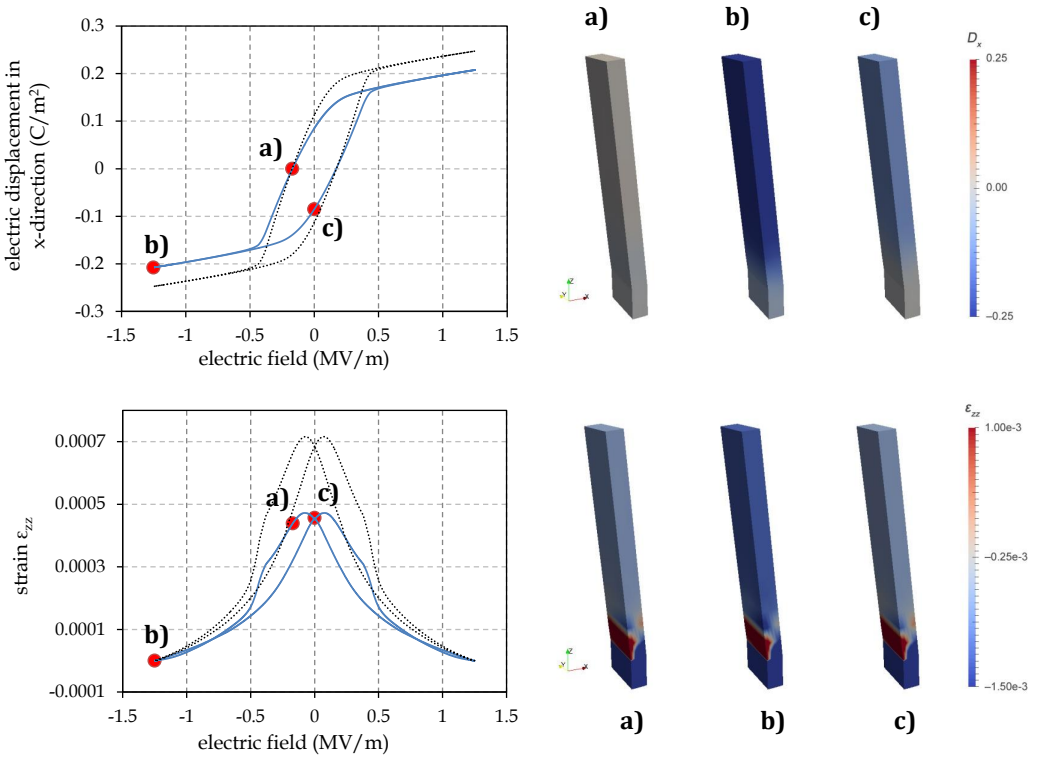

Figure 2.8: Electrical and strain hysteresis of a polycrystalline $BaTiO_3$ beam clamped at the bottom, simulated with 100 grains of random orientation within a 20° cone. Spatial distribution of electric displacement and strain in the z-direction are shown at various points in the electric field loading cycle: a) at the coercive field, b) at maximum electric field amplitude and c) at 0 applied electric field. Dotted lines represent electric displacement and remanent strain for the unconstrained case.

($BaTiO_3$). By starting from a single ferroelectric domain in a single crystal, we gradually expanded the model to describe poly-domains (by convexification) as well as polycrystals (via a Taylor model). The variational model can account for thermo-electro-mechanical coupling as well as for some salient features of the intricate domain switching kinetics (including differences in 90°- and 180°-domain wall motion and electric-field and temperature-dependent domain wall velocities, although the latter are not investigated here). In addition, the model includes entropic contributions of domain mixing and admits the extension to describe phase transformations. All material parameters have been identified from experimental or theoretical data; kinetic model parameters have been obtained from fitting to experimental results. Simulated results included the stress-dependent electrical hysteresis of single- and polycrystals, the associated butterfly curve of remanent

strain vs. electric field, and the influence of experimental boundary conditions on the effective response of clamped samples in recent BES experiments. While the examples have focused on $BaTiO_3$, the presented model is sufficiently general to be extended to, in principle, any ferroelectric ceramic and beyond (with potential for modeling ferromagnetic or multiferroic coupling). In contrast to competing models, the proposed framework is simple and therefore efficient (instead of energy relaxation or lamination, a simple mixing of domain variants is used; polycrystals are approximated by the Taylor construction instead of full-field homogenization), while key microstructural mechanisms and characteristics are retained (instead of an effective, phenomenological polarization field, we account for domain mixtures and avoid the introduction of an empirical remanent energy density that is often used to constrain the effective polarization vector). Of course, this model does not provide local microstructural details nor does it account for, e.g., domain–grain boundary interactions. However, it is sufficiently efficient to admit large-scale finite-element calculations.

Chapter 3

MECHANICAL DAMAGE DURING BIPOLAR ELECTRICAL FATIGUE OF PZT

Research presented in this chapter has been adapted from the following publications:

Tan, W. L., Faber, K. T., Kochmann, D. M. In-situ observation of evolving microstructural damage and associated effective electro-mechanical properties of PZT during bipolar electrical fatigue. *Acta Materialia*, 164:704-713, 2019.
URL https://doi.org/10.1016/j.actamat.2018.10.065

3.1 Introduction

Polycrystalline lead zirconate titanate ($Pb[Zr_xTi_{1-x}]O_3$, or PZT) is ubiquitous in actuators, sensors and memory devices due to its superior piezoelectric and ferroelectric properties [Uchino, 1997, Haertling, 1999, Takasu, 2000]. During operation such components are frequently subjected to sustained cyclic electrical and mechanical loading, which causes fatigue and an eventual degradation of the mechanical properties and device performance. Fatigue is especially detrimental during bipolar electrical loading, which prevents ferroelectric ceramics like PZT and barium titanate ($BaTiO_3$) from being more widely used for large strain actuation [Burcsu et al., 2004] as well as in memory applications and for set-and-hold actuation [Uchino, 1997, Lynch et al., 1995].

Ferroelectric fatigue is a complex process since mechanisms of both mechanical and electrical fatigue are involved, and it manifests itself through changes to the material's microstructure as well as changes in the effective electro-mechanically-coupled performance [Lupascu, 2004]. Observable effects of bipolar electrical fatigue include (*i*) a decrease in amplitude of the polarization hysteresis loop indicating a loss in polarizability, (*ii*) a decrease in amplitude of the butterfly strain hysteresis implying a loss in ferroelectric actuation strain, (*iii*) macroscopic sample cracking especially near electrodes and interfaces, and (*iv*) micro-cracking within the bulk of the polycrystal preferably in an intragranular fashion [Nuffer et al., 2000, Lupascu, 2004, Balke et al., 2007, Zhukov et al., 2016]. While the latter have clear consequences on the mechanical material behavior, the creation of free surfaces also affects the distribution of electrical charges and thereby the ferroelectric perfor-

mance. It is well-established that the progression of crack growth and mechanical damage depend strongly on the cycling frequency of the bias electric field, as is the evolution of the ferroelectric hysteresis and butterfly curve during fatigue. Even though those effects have been qualitatively observed [Shieh et al., 2002, Zhou et al., 2004, Promsawat et al., 2017], they have not been quantified in a systematic fashion.

The origin of the effects of ferroelectric fatigue are collectively attributed to a decrease in domain switching capability with increasing numbers of cycles as well as macro- and micro-cracking within the body [Shang and Tan, 2001, Zhenhua et al., 2011, Hinterstein et al., 2014, Genenko et al., 2015]. These effects are neither independent, nor have they thus far been quantified extensively. Chemical or structural causes of reduced domain switching include the pinning of domain walls at charged defects as well as at oxygen vacancies and other domain walls [Zhou et al., 2004, Robels and Arlt, 1993, Brennan, 2010, Kontsos and Landis, 2009, Rojac et al., 2010, Guo et al., 2015, Fan and Tan, 2018], a decrease in nucleation sites for the formation of new domain walls [Tagantsev and Stolichnov, 1999, Zhang and Bhattacharya, 2005a], development of internal fields [Ozgul et al., 2004, 2008, Zhukov et al., 2010] and internal damage leading to conductive corrosion paths [Duiker et al., 1990]. Mechanical causes of fatigue include macro-crack formation and delamination (particularly near interfaces), micro-cracking within the body (especially along grain boundaries and regions of high internal stresses), as well as domain pinning due to mechanical stresses [Lynch et al., 1995, Shieh et al., 2002, Promsawat et al., 2017, Cao and Evans, 1994].

It is experimentally challenging to isolate and observe the effects of any one of the aforementioned causal mechanisms. Nuffer et al. [2000] employed acoustic emission to observe and classify domain switching in PZT (PIC 151) over 10^8 cycles at 50 Hz. Since acoustic emission events occur due to abrupt local stress or strain changes within a material, acoustic emission events of different amplitudes were attributed to ‘difficult’ and ‘easy’ domain wall motion, which occur at different applied electric fields and are affected by agglomeration of point defects. They also differentiated domain wall motion from micro-cracking events because the latter are two orders of magnitude higher in amplitude. However, that study did not quantify micro-cracking events during fatigue.

A proper quantification of the mechanical damage accrued during ferroelectric fatigue at different bipolar cycling frequencies can serve as the basis for differentiating domain wall pinning due to cracks or internal stresses versus domain wall pinning

caused by point defects and chemical alterations of the material. Physics-based and phenomenological models for the evolution of mechanical fatigue in ferroelectrics due to bipolar electric field cycling have been developed by assuming growth of micro-cracks [Arias et al., 2006, Lange and Ricoeur, 2016], but thus far experimental validation of those models is sparse. Additionally, preliminary theoretical studies [Kim and Jiang, 1996, Sze and Sheng, 2005] investigating the effect of micro-cracking on the decrease in polarization amplitude have shown that mechanical damage contributes to a polarization decrease, but this effect is over an order of magnitude smaller than the observed changes in polarization.

Here, we aim to add new qualitative and quantitative insight into the frequency-dependent ferroelectric fatigue of PZT-5A ($Pb[Zr_{0.52}Ti_{0.48}]O_3$). We use a combination of Broadband Electromechanical Spectroscopy (BES) [Le Graverend et al., 2015], 3D Digital Image Correlation (3D-DIC), and statistical analysis of micro-cracks using scanning electron microscopy (SEM) to isolate and quantify the occurrence of micro-cracking as well as the degradation of the mechanical properties of PZT-5A during bipolar electrical fatigue at various cycling frequencies. BES allows for the simultaneous application of low-frequency high-voltage electrical cycling and high-frequency contactless mechanical vibrational excitation. The former serves to characterize the electrical hysteresis and, in combination with 3D-DIC, the butterfly curve vs. the number of electric cycles. The latter enables the measurement of the dynamic compliance and viscoelastic damping throughout the electrical hysteresis after selected numbers of electric cycles, thus capturing changes in mechanical properties as well as a decrease in microstructural ferroelectric switching since the measured damping correlates with the kinetics of domain wall motion [Wojnar et al., 2014]. The remainder of this investigation is structured as follows. Section 3.2 summarizes the experimental methods, followed by a presentation and discussion of results in Section 3.3, before Sections 3.4 and 3.5, respectively, discuss and conclude this study.

3.2 Materials and Methods

Material Samples

We characterize the microstructure as well as the ferroelectric and viscoelastic properties of lead zirconate-titanate (PZT-5A) beam specimens (H × W × T = 38 mm × 3 mm × 1 mm) obtained from Piezo Systems, Inc. (Woburn, MA, USA). As-obtained samples were poled through-thickness with an average grain size of ∼2 μm (as found by SEM inspection). For electrical testing, samples had sputtered

nickel electrodes covering their two largest, opposite faces.

Broadband Electromechanical Spectroscopy (BES)

We measure the electrical and viscoelastic properties of the PZT-5A samples using a setup of Broadband Electromechanical Spectroscopy (BES) [Le Graverend et al., 2015, Wojnar et al., 2014], schematically shown in Figure 3.1. Beam specimens are clamped at the base by electrically isolated grip electrodes through which a triangle waveform bipolar electric field is applied with a peak-to-peak amplitude of 3.8 kV/mm across the sample's thickness (for reference, the coercive field of the as-received PZT-5A is 1.18 kV/mm [Hooker, 1998]). Connected to a Sawyer-Tower circuit, the electrodes also serve to measure the total electric displacement in terms of accumulated surface charges. Knowledge of the thus obtained average electric displacement and the applied bias electric field yields the electrical hysteresis, which is characterized at electric-field cycling frequencies from 0.2 Hz to 10 Hz. A permanent magnet (neodymium-boron-iron, 6.35 mm × 6.35 mm × 2.54 mm, 12 N maximum pull) is attached to the sample's top end via a stiff Macor® clamp. By enclosing the magnet by a pair of vertical magnetic coils (driven electronically at 100 Hz AC), we exert an oscillating transverse force on the beam's tip in a contactless fashion, resulting in beam bending [Lakes and Quackenbusch, 1996]. By choosing the vibrational frequency significantly higher than the electri-

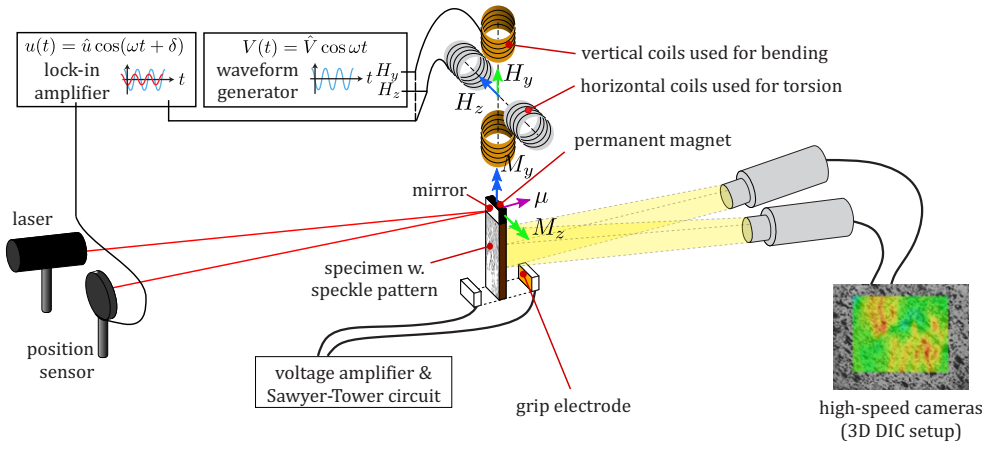

Figure 3.1: Schematic of the combined Broadband Electromechanical Spectroscopy (BES) and 3D Digital Image Correlation (DIC) setup. While 3D-DIC is used to extract the permanent strain in the sample for construction of the ferroelectric butterfly curve, BES is used to characterize the effective viscoelastic properties and the ferroelectric hysteresis across each electric cycle.

cal cycling frequency (yet sufficiently lower than the natural frequency of the beam sample to avoid resonance), we aim for a decoupling of the mechanical and electrical measurements; i.e., while the bias electric field slowly traverses the full electrical hysteresis approximately quasistatically, fast mechanical vibrations are used to extract the viscoelastic response at each point on the electrical hysteresis. To quantify the viscoelastic properties, a HeNe laser is reflected off the beam's tip by a mirror attached to the magnet clamp and onto a split-diode position sensor whose signal is fed into a lock-in amplifier to determine its amplitude and phase lag (with respect to the vibrational driver). The resulting signals admit characterizing the dynamic compliance and the damping (in terms of the loss tangent) of the specimen [Lakes, 2004]. All viscoelastic measurements are taken at 0.1 Hz electric field cycling after a stabilization period of six cycles to reduce any kinetic effects on the measured electro-mechanical data [Wojnar et al., 2014]. That is, even though electric cycling is performed at different frequencies, those frequencies are temporarily changed to 0.1 Hz for the duration of each viscoelastic characterization. Since specimens are tested over large numbers of electric cycles, changing the electric-cycling frequency for only a few cycles in order to obtain clean viscoelastic measurements is expected to not significantly affect the overall response. Furthermore, all measurements are performed in air to allow for full-field strain measurements via Digital Image Correlation (described below). It was verified that differences in viscoelastic measurements taken in air vs. vacuum are negligible for bending at 100 Hz. To investigate the fatigue behavior, each sample is cycled electrically between 10^5 to 10^6 times while recording the above information (with viscoelastic measurements taken only at selected numbers of cycles without interrupting the electrical cycling and without remounting the sample).

3D Digital Image Correlation (3D-DIC)

Three-dimensional Digital Image Correlation is used to obtain full-field, contactless strain measurements of the specimen during electrical cycling. Two high-speed cameras (IL5 from Fastec Imaging, San Diego, CA, USA) are used for imaging at 25 frames per second for a duration of 12.5s for each data point, and images are processed using VIC-3D v.8 (Correlated Solutions, Inc., Irmo, SC, USA) to obtain the in-plane strain and out-of-plane displacement on the sample's back surface. Samples are spray-coated with a black and white speckle pattern, which is used to identify changes in displacements during loading [Sutton, 2008].

In the cantilever beam configuration chosen here to admit vibrational viscoelastic

measurements, we use 3D-DIC in order to differentiate the in-plane strains from the effects of out-of-plane movement of the sample which causes an apparent change in strain of similar magnitude. We note that the strain component thus obtained and reported in the subsequent butterfly curves is perpendicular to the direction of the applied electric field, whereas most reported strain data in the literature are parallel to the applied electric field. Nevertheless, those two remanent strain components are crystallographically coupled, so that the same qualitative conclusions may be drawn.

Micro-Crack Statistics

Scanning Electron Microscopy (SEM)

In addition to samples fatigued for the full 10^5 to 10^6 cycles, we also investigate the evolution of micro-cracking by electrically cycling specimens up to intermediate numbers of cycles, followed by determining micro-crack statistics on images obtained from scanning electron microscopy (ZEISS 1550VP Field Emission SEM). Samples used for ex-situ micro-crack analysis must be prepared with care so as not to introduce additional cracks during the preparation process. For each sample, the nickel coating is removed via hand polishing using alumina polishing paper followed by four hours of vibro-polishing using colloidal silica. Unlike typical polishing and etching procedures using HF, colloidal silica vibro-polishing does not etch pristine, uncracked grain boundaries or differentially etch domains within a grain. This yields a low surface roughness with high topographic contrast in micro-cracked regions. Polished surfaces are imaged using SEM in backscattered electron mode (BSE) at 10 kV with 7000× magnification at a working distance of 7.3mm. BSE gives high contrast from cracked regions, which allows for automated edge detection of micro-cracks and cataloging of crack length and density for quantitative statistics. Figure 3.2 shows a representative SEM image of a fatigued PZT sample with clearly visible grain boundaries, some ferroelectric domains, voids and cracks. Cracks were cataloged automatically using ImageJ's *Analyze Particle* function (size: 30-Infinity pixels, circularity: 0.0-0.5) [Schneider et al., 2012]. Eight images per sample were taken and independently evaluated to yield statistically representative data.

Kachanov Model

In order to correlate the measured micro-crack density with macroscopic mechanical properties, homogenization models are a suitable avenue. A simple analytical

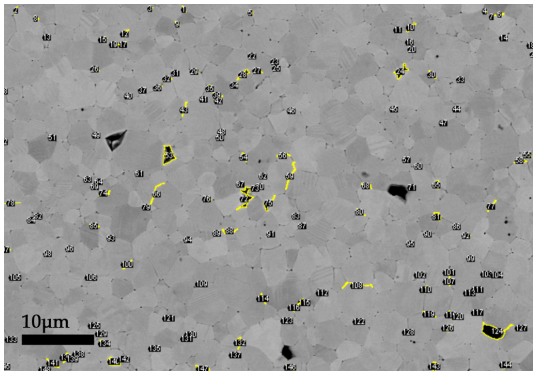

Figure 3.2: Representative SEM micrograph of micro-cracks in a fatigued PZT-5A sample with automatic edge recognition and size measurement for quantitative statistics.

homogenization of a cloud of micro-cracks to give the macroscopic compliance is the model by Kachanov [1992], which assumes a cloud of planar micro-cracks of random orientations, embedded in an isotropic material. Here, we may approximate the polycrystalline, untextured bulk PZT as isotropic. However, micro-cracks along grain boundaries follow a tortuous path and their measured length is not equivalent to the length of a straight-line crack. We hence account for this tortuosity by establishing an effective length L_R, defined as the diameter of the circle which fully bounds each micro-crack. The macroscopic compliance S as a function of the micro-crack density is then approximated by

$$\frac{S}{S_0} = 1 + \frac{16\left(1-\nu_0^2\right)\left(1-\frac{3\nu_0}{10}\right)}{9\left(1-\frac{\nu_0}{2}\right)}\rho, \tag{3.1}$$

where the crack density ρ is defined by

$$\rho = \frac{1}{A}\sum_{i=1}^{n} L_{R_i}^2. \tag{3.2}$$

S_0 and ν_0 are the undamaged base material's compliance and Poisson's ratio (for isotropic polycrystalline PZT, $\nu_0 = 0.35$ as per vendor specification), A is the area of the image, and L_{R_i} is the length of the i-th crack (with n cracks in total).

3.3 Results

Evolution of the Electro-Mechanically Coupled Hystereses

Figure 3.3 shows representative hysteresis curves of electric displacement, relative dynamic compliance and relative damping for specimens cycled at 0.2, 1, 5 and

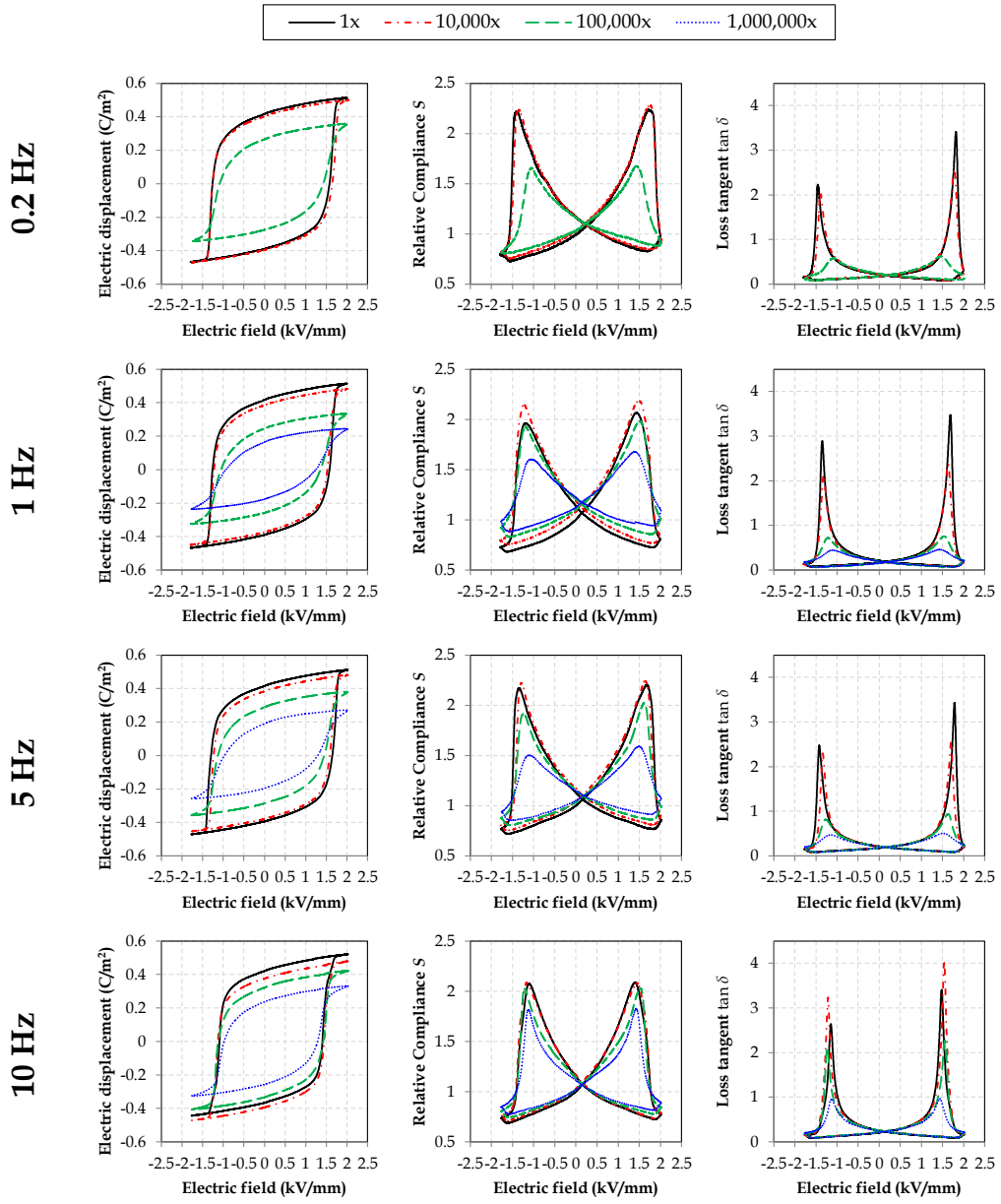

Figure 3.3: Broadband Electromechanical Spectroscopy (BES) hysteresis curves of electric displacement (*left column*), relative compliance S (*middle column*) and normalized loss tangent $\tan\delta$ (*right column*) for different electric cycling frequencies, measured after 1, 10^4, 10^5 and 10^6 cycles.

10 Hz. Curves obtained after 1, 10^4, 10^5 and 10^6 cycles are shown for each electric cycling frequency to highlight qualitative and quantitative changes in material behavior. Key trends evident from these curves include the following: (*i*) The polarization magnitude (i.e., the difference between positive and negative remanent polarization at zero applied electric field) decreases with prolonged bipolar electrical cycling across all frequencies. (*ii*) The peak height of the relative compliance decreases with cycling across all frequencies. (*iii*) The peak height of the loss tangent decreases with cycling across all frequencies. (*iv*) The relative compliance at zero applied electric field (measured at the transition from negative to positive e-field) increases slightly with electric cycling across all frequencies. (*v*) The viscoelastic loss tangent at zero applied electric field does not change significantly with cycling.

Trends (*i*), (*ii*) and (*iii*) are attributed to the extent of domain switching induced either electrically, mechanically or both, while trends (*iv*) and (*v*) reflect the base material property at zero applied electric field where no domain switching occurs. To further characterize the differences in degradation behavior at different electric field cycling frequencies, we track the above five parameters continually over the course of 10^5 to 10^6 cycles for each electric cycling frequency.

Electrical Hysteresis

As a standard metric for establishing electrical degradation in ferroelectrics during fatigue, we track the polarization hysteresis curve height at an applied electric field of $E = 0$ kV/mm. As Figure 3.4 shows, the decrease in polarization magnitude (and thus in polarizability) occurs most rapidly at lower cycling frequencies and approaches a lower tail-off than at higher frequencies. The curves showing the polarization magnitude also appear to converge with decreasing cycling frequencies, where the difference between the 1 Hz and 5 Hz trend is smaller than the difference between the 5 Hz and 10 Hz, while 0.2 Hz[1] behaves very similarly to 1 Hz.

The observed decrease in polarization magnitude is a well-known phenomenon of bipolar electrical fatigue, which is often attributed to the agglomeration of point defects and the resulting obstruction of domain wall motion [Robels and Arlt, 1993, Brennan, 2010, Zhou et al., 2004, Kontsos and Landis, 2009, Rojac et al., 2010, Guo et al., 2015]. The frequency dependence of the rate of degradation has also been observed before in various ferroelectric ceramics [Zhang et al., 2001, Zhou et al.,

[1] We chose to conduct experiments in air to enable the combined use of BES and 3D-DIC, which unfortunately results in mechanical sample failure especially at low frequencies; therefore, the 0.2 Hz data in Figure 3.4 end prematurely upon sample failure after close to 10^5 cycles.

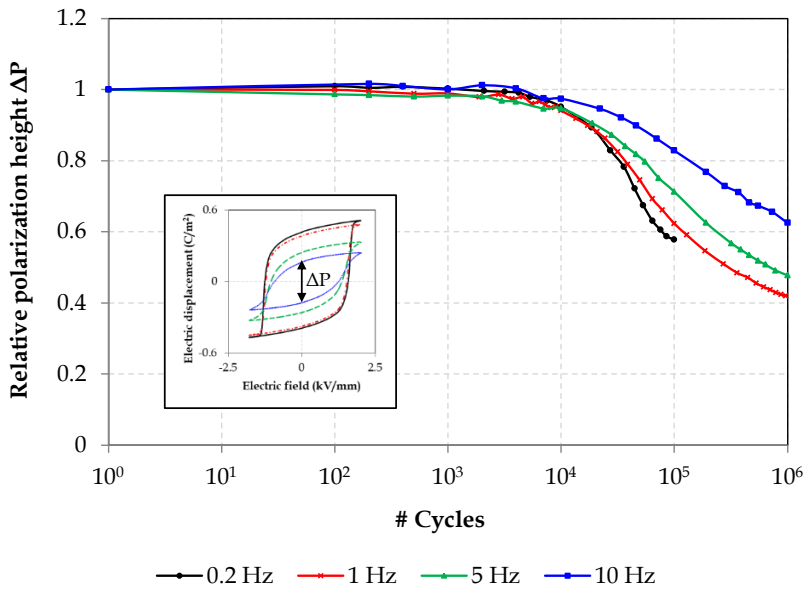

Figure 3.4: Relative polarization magnitude (i.e., height of the electric hysteresis loop at 0 kV/mm applied electric field) over 10^6 cycles of bipolar electrical fatigue for electric cycling frequencies of 0.2 – 10 Hz.

2004, Promsawat et al., 2017], and it is believed to be due to kinetic limitations. At higher frequencies, full switching may not occur, which reduces internal mechanical damage caused by lattice mismatch during 90°-switching. High frequencies also slow down the migration of charged defects, which in turns slows down the aggregation of point defects and hence delays the degradation of the polarization arising from domain wall pinning. This is consistent with the observation that at lower frequencies below 5 Hz (where full switching is achieved) the change in rate of degradation between one frequency and the next decreases and the reported data eventually appear to converge.

Viscoelastic Properties

It has been shown [Wojnar et al., 2014] that ferroelectric ceramics exhibit changes in viscoelastic properties when undergoing electric field cycling. In particular, the mechanical compliance and damping both peak near the coercive field, which has been attributed to, respectively, the mechanically induced domain switching and the dissipative effects of domain wall motion during ferroelectric switching. Specifically, as the electric hysteresis is traversed slowly by the applied electric field, the high-frequency vibrations admit characterizing mechanical damping which is tied to mechanisms of internal friction (here, of domain switching kinetics). Changes

in the measured loss tangent are hence linked to ferroelectric switching activity and can thus provide information about the inhibition of ferroelectric switching as a consequence of fatigue, independent of any signs of mechanical fatigue. In order to assess both the mechanical changes and the dissipative effects of domain wall motion, we here track the compliance at $E = 0$ kV/mm, further the peak compliance, the loss tangent at $E = 0$ kV/mm, and the peak damping over 10^5 to 10^6 cycles for different electric cycling frequencies.

Dynamic Compliance

Peaks in dynamic compliance occur close to the coercive field because a small additional mechanical load can easily overcome the energy barrier between domain orientations and induce domain switching. When a bending moment is applied, the side of the specimen in tension switches into a vertical a-domain structure perpendicular to the applied electric field direction, while the side in compression switches into a horizontal c-domain structure parallel to the applied electric field. This mechanically induced domain switching increases the magnitude of bending of the specimen, manifesting as an apparent increase in dynamic compliance.

Figure 3.5a shows the change in peak relative compliance with cycling at different electric field frequencies. The shaded yellow region indicates the extent of machine noise relative to the measured signal. Similar to trends in polarization magnitude, the peak relative compliance remains fairly stable until 10^4 cycles before dropping steeply (depending on electric cycling frequency), then plateauing as it approaches 10^6 cycles. Note that this drop in peak relative compliance is approximately half that of the decrease in polarization magnitude. Additionally, the shapes of the curves differ significantly for 10 Hz and 0.2 Hz, and the lower frequencies do not converge. These differences suggest that, although both polarization magnitude and peak relative compliance are related to the extent of domain switching, the former is primarily a function of changes in electrical properties in the ceramic while the latter is more closely related to the mechanical properties; hence, the nature of their fatigue behavior differs.

The base dynamic compliance taken at $E = 0$ kV/mm is indicative of changes in the mechanical properties of the specimen independent of domain switching phenomena. A primary cause for changes in compliance in ceramics is the occurrence of macro- and micro-cracking [Gu and Faber, 1995]. Figure 3.5b shows that the base dynamic compliance of the specimen without applied electric field

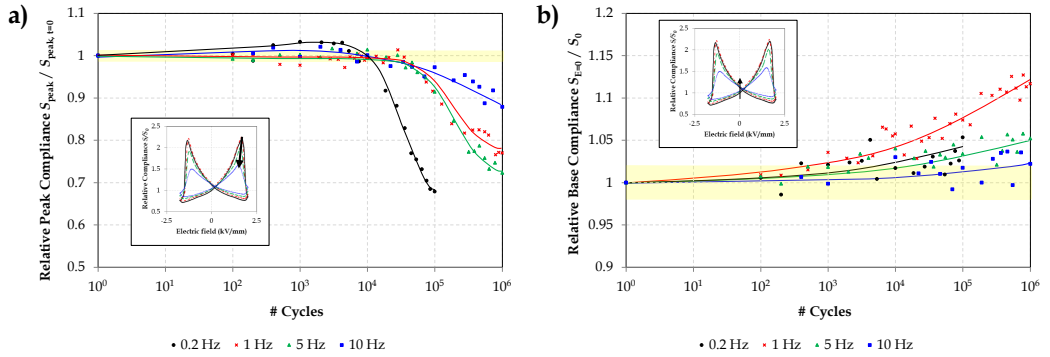

Figure 3.5: a) Relative peak compliance and b) relative base compliance at E = 0 kV over 10^6 cycles of bipolar electrical fatigue at electric cycling frequencies of 0.2 – 10 Hz. In both figures, the shaded yellow region represents the magnitude of machine noise relative to data.

increases by more than 10% over 10^6 cycles of electric field loading at 1 Hz, likely due to micro-mechanical damage accumulating over time. Higher frequencies of electric loading yield smaller increases in compliance, with 5 Hz increasing by approximately 5% and 10 Hz by only about 2%. These trends suggest that greater mechanical degradation occurs for lower electrical cycling frequencies, similar to the higher electrical property degradation at lower cycling frequencies observed via polarization magnitude in Section 3.3. The lowest frequency measurements do not appear to follow this trend, likely due to complications from holding a high e-field for long durations, which damages the specimen non-uniformly close to and away from clamped regions. We note that the changes in mechanical base compliance (Figure 3.5b) are significantly smaller than those of the switching-related peak compliance (Figure 3.5a).

Damping

Damping, i.e., the loss tangent (denoted by $\tan\delta$), is a measure of mechanical energy absorption through internal friction mechanisms [Lakes, 1999]. Peaks in damping are observed close to the coercive field and occur due to the energy absorbed by mechanically induced domain switching during mechanical vibrations. Figure 3.6a shows the change in peak damping with cycling at different electric field frequencies. Peak damping degradation trends once again mirror those of the polarization magnitude and relative compliance, with higher frequencies exhibiting less degradation. However, the decrease in energy absorption is of much greater magnitude than either polarization magnitude or relative compliance, decreasing to

<30% of its original state after 10^6 cycles. This dramatic decrease suggests that mechanically induced domain switching suffers more greatly from the effects of fatigue than does electrically induced domain switching.

The base damping taken at $E = 0$ kV/mm measures the mechanical energy absorption in the specimen independent of domain switching phenomena. At zero applied electric field, no additional absorption of mechanical energy due to domain switching is expected to occur. Figure 3.6b shows the relative change in base damping of the specimen at $E = 0$ kV/mm. There is a moderate change of ±5% over 10^6 cycles. However, as damping is very low, this scatter lies within the noise margin as shown by the shaded region. This small change in damping at zero electric field with little to no cycling frequency dependence is consistent with the understanding that energy absorption occurs due to mechanically induced domain switching, which is absent at $E = 0$ kV/mm.

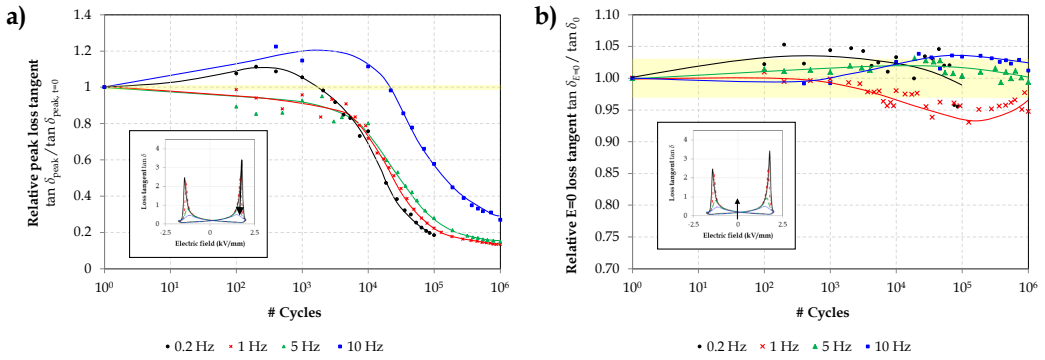

Figure 3.6: a) Relative peak damping and b) relative base damping at $E = 0$ kV/mm over 10^6 cycles of bipolar electrical fatigue at electric cycling frequencies of 0.2 – 10 Hz. The shaded yellow region represents the magnitude of noise relative to the data.

Strain Hysteresis

The ϵ_{yy}-strain hysteresis ('butterfly') curves obtained from DIC for electrical cycling at 5 Hz is shown in Figure 3.7a for 10^3, 10^4, 10^5 and 10^6 cycles. As with the hysteresis curves of the other electromechanical properties shown in Figure 3.3, the magnitude of the strain hysteresis decreases with cycling. This change in strain is due to ferroelastic switching, so this trend is consistent with other indicators of a reduction in domain switching during fatigue. As these measurements were taken without mechanical loading of the specimen, the domain switching underlying this data is purely electrically induced.

The magnitude of strain change per cycle is measured and plotted in Figure 3.7b for 0.2, 5 and 10 Hz. Shapes and trends of the strain magnitude fatigue curves exhibit significant similarity to the polarization magnitude fatigue curves (see Figure 3.4), and both sets of curves exhibit similar magnitudes of decrease ranging from 40−60% after 10^6 cycles. This is consistent with the understanding that both properties originate from purely electrically induced domain switching and are directly related to each other crystallographically.

Micro-Cracks

Figure 3.8 shows SEM micrographs of specimens (a) before and (b) after $2 \cdot 10^6$ cycles of fatigue. Micro-cracks appear to form primarily along grain boundaries, but examples of intra-granular fracture are also visible. Crack densities were measured using images of polished surfaces for 0, 10^4, 2×10^4, 10^5, 2×10^5 and 10^6 cycles, cycled electrically at 1 Hz and 10 Hz as representative frequencies. Figure 3.9 shows the relative crack density evolution for 1 Hz and 10 Hz cycling. Small fluctuations in early data points, in particular the apparent decrease between 0 and 10^4 cycles at 1 Hz, are due to sampling and have a T-test P-value of 0.961, and thus are not statistically different.

Both show an increase in crack density, with the slower 1 Hz cycling exhibiting a larger (7%) increase in crack density while the faster 10 Hz cycling only shows a 4% increase. This difference is consistent with macroscopic BES measurements which suggest that lower-frequency fatigue results in higher levels of degradation both electrically and mechanically.

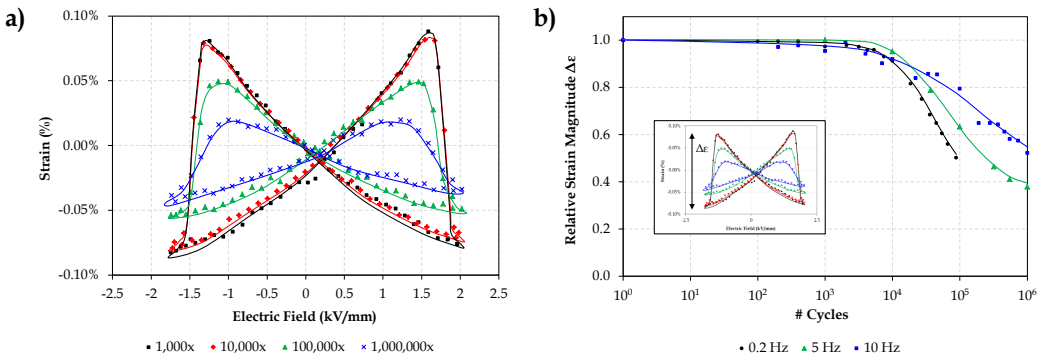

Figure 3.7: (a) In-plane y-direction (vertical relative to beam) strain hysteresis curves after different numbers of electric cycles for the representative electric cycling frequency of 5 Hz; (b) evolution of the peak-to-peak strain magnitude over 10^6 cycles of bipolar electrical fatigue for all tested frequencies from 0.2 − 10 Hz.

3.4 Discussion

Our BES and DIC measurements as well as micro-crack statistics are aimed at shedding light onto the impact of mechanical fatigue (primarily manifesting in micro-crack and void formation on the microscale of the brittle ceramic) versus electrical fatigue (stemming from a combination of mechanisms that include domain wall pinning, chemical alterations, and charge accumulation). While both fatigue

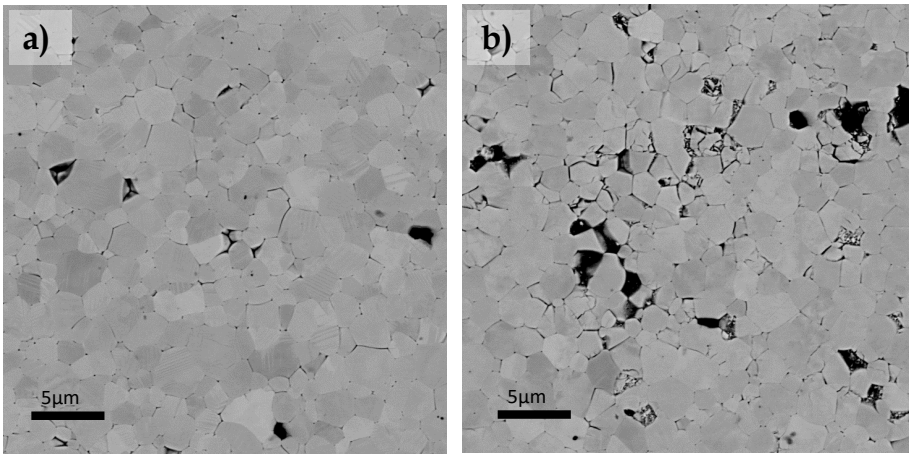

Figure 3.8: a) Polished surface of an as-received, pre-poled PZT specimen, b) polished surface of a PZT specimen after 2×10^6 bipolar electrical cycles at 1 Hz.

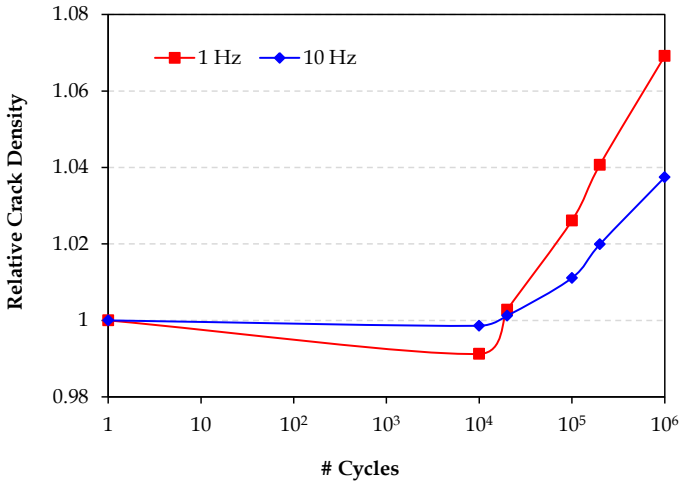

Figure 3.9: Comparison of the relative crack density evolution during fatigue for the two representative cases of 1 Hz and 10 Hz bipolar electrical cycling.

phenomena occur simultaneously and in a coupled fashion, they affect the measured properties in different ways, which is why the presented data help improve our understanding of the domain switching behavior and crack growth during bipolar electric field cycling of ferroelectric ceramics. In the following sections, we first establish a correlation between the measured mechanical compliance data and the formation of micro-cracks, followed by a discussion of the evolution of electrical vs. mechanical fatigue.

Micro- vs. Macroscale Mechanical Properties

In order to quantify the mechanical damage that occurs due to electric cycling, we have tackled the problem from both the macroscopic scale and the microscopic scale. On the one hand, using BES we have obtained macroscopic data of the base viscoelastic properties (viz., compliance and damping) of the entire specimen at $E = 0$ kV/mm while fatigue is progressing. On the other hand, by terminating the electric field cycling after various intermediate numbers of cycles, we have measured the evolving micro-crack density. Using the model described in Section 3.2, we can independently calculate and anticipate the decrease in the macroscopic compliance based on the increasing concentration of micro-cracks. Figure 3.10 shows the comparison between the two compliance metrics, viz. the macroscopic BES measurements and the microstructurally-informed, calculated compliance based on the measured micro-crack density for two representative frequencies. The magnitudes of change as well as the slopes of both methods are in convincing agreement, suggesting that the macroscopic changes in dynamic compliance are, to a large extent, indeed due to bulk micro-cracking and not any other effect which could potentially alter the compliance, such as changes in domain structure or purely surface and electrode-interface macro-cracking. The presented compliance data thus allow us to interpret the changes in mechanical properties during fatigue with good confidence.

Domain Switching

The magnitude of the polarization hysteresis over time has been the most common proxy to describe fatigue in ferroelectrics. It indicates the degree of domain switching occurring and has a well-established logarithmic decrease with cycling, which we have verified via the BES measurements in Figure 3.4. Wojnar et al. [2014] argued that the strong increase in mechanical compliance and damping near the coercive field are similarly due to domain switching. Our simultaneous BES measurements

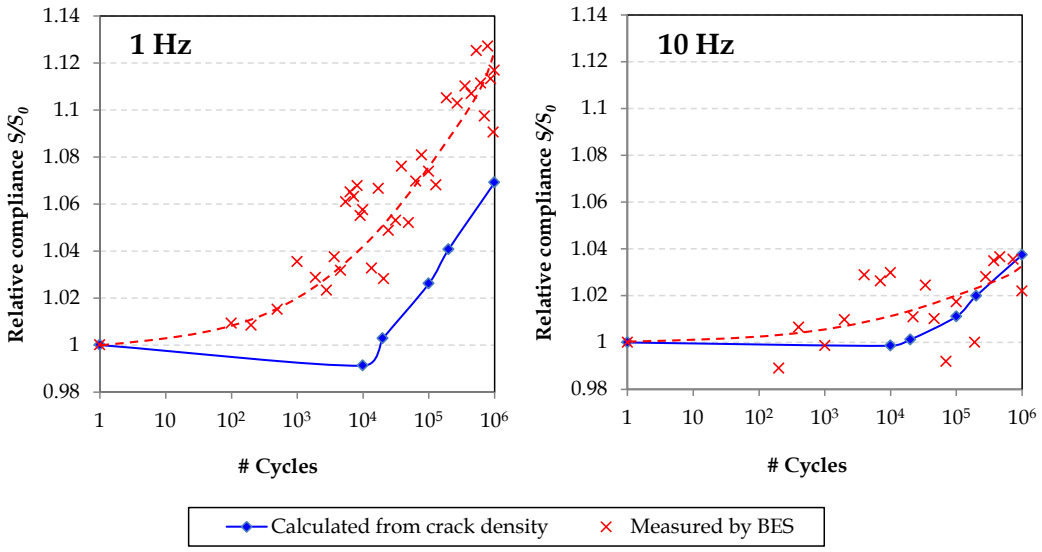

Figure 3.10: Comparison of the normalized compliance $S_{E=0}/S_0$ measured via BES at $E = 0$ kV/mm (*red cross markers*) and the relative compliance calculated from the micro-crack statistics (*blue diamond markers*) at electric field cycling frequencies of 1 Hz (*left*) and 10 Hz (*right*). The shown relative compliance data are normalized by the respective base values during the first cycle.

of the polarization, peak dynamic compliance, and peak damping at various times during electric cycling (as shown in Figures 3.4, 3.5 and 3.6, respectively) confirm a remarkable similarity in the time evolution of these three properties. This indeed suggests a common underlying cause and corroborates the argument that the motion of domain walls changes the viscoelastic properties of the ferroelectric under varying electric field, most pronounced when close to the coercive field where domain wall mobility is highest. For all three measured properties, a lower electric cycling frequency leads to a steeper and larger overall decrease in each property. For the polarization and strain magnitudes, the effect of further lowering the cycling frequency below 5 Hz diminishes quickly, suggesting that electrically induced domain switching kinetics occurs on a similar timescale that is independent of the cycling frequency in this slow, quasistatic regime. By contrast, the peak compliance and peak damping trends differ from those polarization and strain trends in both magnitude and shape, which supports the hypothesis that both properties are associated with mechanically induced domain switching instead. While lower-frequency cycling appears to degrade more quickly, there is no clear trend of convergence for the peak compliance in the quasistatic limit, since, e.g., the 0.2 Hz peak compliance

data decreases more rapidly than those reported for 1 and 5 Hz. This suggests that – unlike electrical fatigue whose signs tends to converge in the low-frequency limit – a different mechanical degradation mechanism becomes dominant at low frequencies (or that the specimen is mechanically degraded non-uniformly at lower frequencies). Since we could isolate the purely mechanical effects of fatigue through the $E = 0$ kV/mm viscoelastic properties of the specimen (which correlate with the ex-situ micro-crack density measurements, as shown in Section 3.4), it is natural to conclude that micro-cracking is responsible for the mechanical degradation and that the latter is hence more sensitive to frequency in the low-frequency range.

We note that the peak compliance data also exhibit a small increase in peak height until about 10^4 cycles before decreasing logarithmically. The mechanism for this small increase is unclear but could be a result of the interplay between micro-crack formation and increasing alignment of the domain structure of grains resulting in more mechanically induced domain switching.

Base Viscoelastic Properties

In order to quantify the effect of mechanical degradation on the overall decrease in ferroelectric performance of the specimen, we examine the change in the base (i.e., $E = 0$ kV/mm) viscoelastic properties of the specimen, as described in Section 3.3. Figure 3.5b shows a clear increase of the dynamic compliance with time across all electric loading frequencies, which is in agreement with the formation of micro-cracks during bipolar electric cycling, hypothesized to be due to internal stresses caused by strain mismatch across grains during domain switching. In general[2], the measured compliance appears to increase faster for lower frequencies, which could be due to more complete domain switching increasing the internal mechanical stresses and hence generating more micro-cracking. Low frequencies are also more likely to result in charge build-up and internal discharge, which also triggers cracking. We note that damping at $E = 0$ kV/mm remains within the level of noise throughout cycling (see Figure 3.6b), which verifies that mechanically induced domain switching does not occur far from the coercive field, and that any changes in internal stresses do not cause significant changes in internal friction of the ceramic material.

[2]We note that, as discussed before, the results at 0.2 Hz electric cycling frequency deviate from some of the trends discussed here for the viscoelastic properties. This was attributed to complications associated with applying large e-fields over long times, which damages the specimen non-uniformly close to and away from clamped regions.

3.5 Conclusions

Viscoelastic and electrical properties of PZT-5A were measured in-situ during bipolar electrical loading at 0.2, 1, 5 and 10 Hz. The hysteresis curves of polarization, compliance, damping and strain showed significant degradation over 10^6 cycles, with higher frequencies degrading less than lower frequencies. Polarization magnitude and strain magnitude, both associated with electrically induced domain switching, decreased by 40-60%. Properties arising from mechanically induced domain switching such as the peak compliance decreased by 10-30%, while the peak damping (associated with the domain wall kinetics) decreased by 80-90%. While attribution of causes of domain switching degradation was not possible, the extent of mechanical damage could be accurately quantified by correlating macroscopic dynamic compliance and micro-crack density evolution, which showed good agreement and confirmed that compliance changes during fatigue were primarily due to micro-cracking. Interestingly, results indicate that electrical fatigue (i.e., the degradation of domain switching processes as seen in the changes of the polarization magnitude and strain amplitude as well as in the peak damping indicative of domain switching activity) converges to a low-frequency limit that is independent of electric cycling frequency, whereas mechanical fatigue (surfacing in the measured compliance data and supported by SEM crack counting) strongly depend on frequency even in the low-frequency limit. This hints at separate mechanisms at play, which may guide further (particularly micro-scale) experimentation as well as model development. We note that our study did not probe the micro-mechanical effects of domain wall pinning, defect agglomeration, oxygen vacancies and other chemical effects; we cannot assess to what extent each of those individually contributes to the decrease in domain switching during fatigue.

Chapter 4

VISCOELASTIC MEASUREMENTS OF POLYCRYSTALLINE BARIUM TITANATE

4.1 Introduction

Barium titanate (BT) was the first ferroelectric oxide to be discovered in 1945, more than 20 years after the discovery of the phenomenon of ferroelectricity in Rochelle salts and a decade after the discovery of ferroelectricity in the potassium dihydrogen phosphate (KDP) family of crystals [Rosen et al., 1954]. It is not only of historical significance, but is also commonly viewed as the archetypal perovskite ferroelectric. Although BT is no longer prevalent as a piezoceramic due to its relatively low piezoelectric constant compared to newer materials like PZT, PMN and PLZT, its simple tetragonal structure makes it an attractive material of study to understand ferroelectric switching mechanisms [Polking et al., 2012, Gao et al., 2013] and to model [Kamlah, 2001, Landis, 2004].

Our experiments thus far have focused on PZT due to its ubiquity in modern applications. PZT is most commonly fabricated at its morphotropic phase boundary where its tetragonal and rhombohedral phases co-exist, and this coexistence of phases allows it to accommodate greater strain and gives it its superior piezoelectric performance [Haertling, 1999, Hooker, 1998, Li et al., 2005]. However, most computational models of ferroelectric switching (including our own) use BT, or purely tetragonal symmetries as their basis of formulation, either by defining these as the stable polarization directions *a priori*, or using 6-welled symmetry for the Ginzburg-Landau energy landscape [Kamlah, 2001, Zhang and Bhattacharya, 2005a,b, Su and Landis, 2007, Lange and Ricoeur, 2016]. Such formulations perform well when simulating hysteresis behavior of single-crystals of BT [Zhang and Bhattacharya, 2005a,b], however, polycrystal formulations, depending on the assumptions used e.g., whether or not crystal symmetry is accounted for, may capture characteristic BT behavior [Landis and McMeeking, 2001, Landis] or may more closely resemble experimental polycrystalline PZT hysteresis behavior [Huo and Jiang, 1997, Cocks and McMeeking, 1999, Kamlah and Tsakmakis, 1999, Landis, Schröder and Romanowski, 2005, Miehe and Rosato, 2011].

The origin of different switching behavior in PZT and BT is likely due to the

phenomenon of *strain limits*. The issue of strain limits in ferroelectric switching is usually associated with thin films due to strain mismatch with the substrate during domain reorientation [Cao, 2005]. The constraint on switching leads thin films to have lower saturated polarization and more diffuse, rounded polarization hystereses than an unconstrained single-crystal. Li et al. [2005] demonstrated strain limits in ferroelectric polycrystals of a single crystallographic phase via neutron diffraction experiments, and in early experiments on poling of polycrystalline BT, Subbarao et al. [1957] noted that only 9-13% of domains reoriented during poling, likely due to strain limits.

Most in-situ experimental observations of domain switching processes on the microscale in BT have thus far been performed on thin films and nanocrystals [Gao et al., 2013, Polking et al., 2012], as these sample dimensions are necessary for the characterization methods employed such as transmission electron microscopy (TEM), polarized light microscopy (PLM) and x-ray diffraction (XRD). Alternatively, only the surface may be visualized in techniques such as piezoresponse force microscopy (PFM). Experimental data on domain switching processes in bulk polycrystals is sparse; the mechanical constraints in bulk specimens due to different grain orientations and stresses at grain boundaries are not present in the comparatively unconstrained single-crystals and comparatively more constrained thin films. Thus, they present a different switching environment from the more well-studied geometries. Understanding the nature of domain switching in bulk BT could hence inform future models of perovskite ferroelectrics, particularly with respect to the relative importance of incorporating the effect of mechanical constraints, as well as the importance of crystal symmetry.

Here, the aim is to add new qualitative insight into the frequency-dependent domain switching behavior of BT. A combination of Broadband Electromechanical Spectroscopy (BES) and 3D Digital Image Correlation (3D-DIC) is again used to probe the ferroelectric and viscoelastic behavior of BT. Preliminary microstructural imaging was performed in an effort to understand some surprising and unexpected viscoelastic behavior. Section 4.3 presents the observed viscoelastic behaviors and trends, which are discussed in terms of potential microstructural origins in Section 4.4.

4.2 Materials and Methods

Material Samples

The ferroelectric and viscoelastic properties of polycrystalline barium titanate (BT) beam specimens (H × W × T = 29.6 and 34 mm × 3 mm × 1 mm), obtained in collaboration with Presidio Components Inc. (San Diego, CA, USA), were characterized. Specimens were prepared via ball-milling of TiO_2 and BaO powders in PVB binder, followed by tape-casting of the slurry. Dried tapes were stacked and pressed isostatically, then sintered at 1300° C for 10-15 days with a ramp rate of 10-20° C/h. Sintered plates were cut to shape. As-obtained samples were unpoled, with an average grain size of ~1.5 μm (by SEM inspection). For electrical testing, samples were coated with ~210 nm-thick nickel electrodes by electron beam evaporation on their two largest, opposite faces.

Specimens were prepared for SEM by vibropolishing with 30nm colloidal silica for 4h to obtain a high flatness polish and mild chemical etch to reveal domain structures within grains. Preliminary piezoresponse force microscopy (PFM) images in in-plane mode were taken on the surface of as-prepared, unelectroded specimens.

Broadband Electromechanical Spectroscopy

The same setup as in Section 3.2 for Broadband Electromechanical Spectroscopy (BES) measurements was used for consistency of comparison between specimens of different materials. The dynamic compliance and phase lag of BT specimens of two different lengths were probed across a range of frequencies to determine each specimen's resonant frequency. These were also used as references for each specimen's $E = 0$ kV/mm base viscoelastic properties (Figure 4.1). While experiments were conducted on both lengths of specimens, the higher resonance frequency of the 29.6 mm specimen offered a larger frequency space to investigate frequency-dependent trends, thus results presented in this section are taken from this specimen.

4.3 Results

Figures 4.2 and 4.3 show representative hysteresis curves of electric displacement, relative dynamic compliance and damping for a specimen cycled at 50, 75, 100, 130 and 150 Hz mechanical probe frequency and 0.1, 0.2, 0.5 and 1 Hz e-field frequency, respectively. Key features evident from these curves include the following: (*i*) The polarization of the specimen is insensitive to changes in mechanical probe frequency or e-field driving frequency. (*ii*) There are no sharp peaks in relative compliance or damping. (*iii*) At low e-field frequencies, hysteresis curves are asymmetric. (*iv*) The

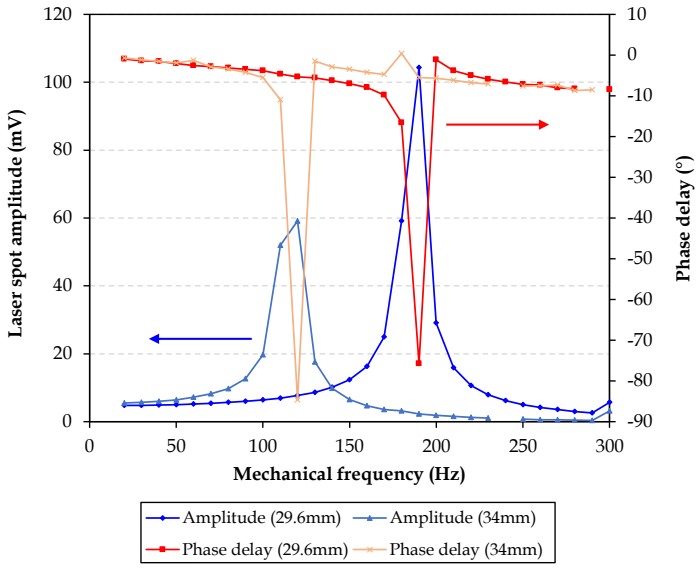

Figure 4.1: Viscoelastic response of BT specimens of different lengths (29.6 mm and 34 mm) showing bending amplitude (*blue lines*) and phase delay (*red lines*) at different mechanical oscillation frequencies to determine resonant frequencies.

shape of the hysteresis of relative compliance and damping change significantly with mechanical probe frequency. (*v*) Positions of peaks and dips in relative compliance and damping shift with e-field frequency.

In pioneering BES work on PZT by Wojnar et al. [2014], relative compliance and damping changes were interpreted as being associated with domain wall motion. Sharp peaks in relative compliance and damping at the coercive fields were thus easily explained, as this is where domain walls are most mobile. This interpretation was later refined in our study of fatigue in PZT, separating electrically induced domain wall motion from mechanically induced (or ferroelastic) domain wall motion, and showing that these quantities evolved differently over time, and hence, were not one and the same feature. Given this paradigm, described here are the key trends in relative compliance and damping observed in BT, and offer a possible interpretation of domain switching mechanisms based on this data in Section 4.4.

Effect of Mechanical Probe Frequency

Figure 4.2 shows the change in hysteresis behavior in electric displacement, relative compliance and damping for a specimen cycled at 0.1 and 1 Hz e-field frequency, respectively, and probed mechanically at 50, 75, 100, 130 and 150 Hz. Previous

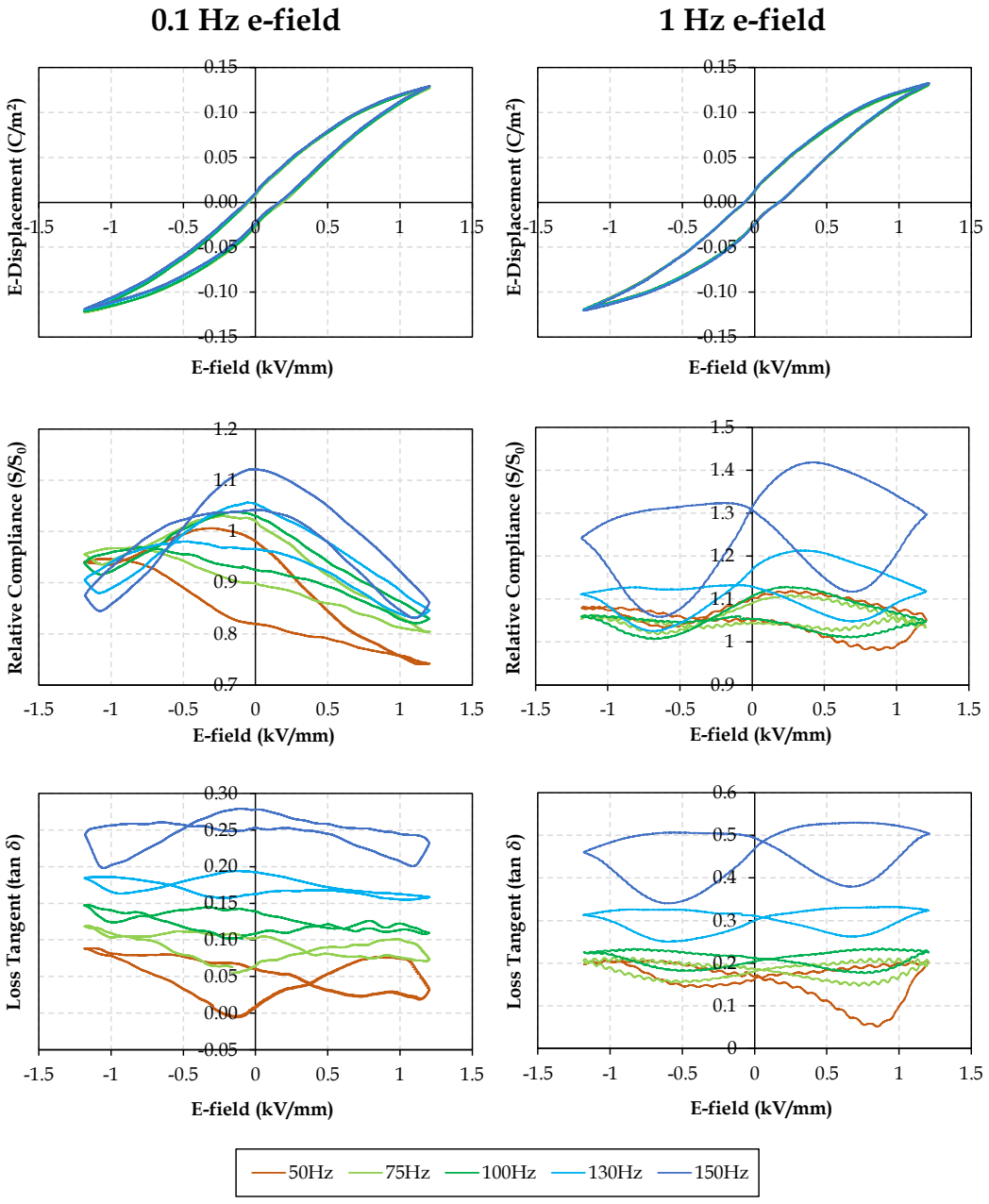

Figure 4.2: Broadband Electromechanical Spectroscopy (BES) hysteresis curves of electric displacement (*top row*), relative compliance (*middle row*) and damping or loss tangent (*bottom row*) for different mechanical probe frequencies at 0.1 Hz (*left colum*) and 1 Hz (*right column*) e-field cycling for barium titanate.

work on PZT had suggested that polarization, relative compliance and damping were relatively insensitive to changes in mechanical probe frequency, affecting only the magnitude of peak heights. This insensitivity is indeed reflected in the electric displacement curves of BT as well, where all curves overlap. However, here new trends in the *viscoelastic* evolution of a ferroelectric ceramic during bipolar electrical cycling are presented.

Relative Compliance

At 0.1 Hz e-field cycling frequency, relative compliance hysteresis curves (Figure 4.2, middle row) are asymmetric, featuring a prominent single peak close to $E = 0$ kV/mm on the positive ramp of the cycle (i.e. ramping from negative to positive e-field). The negative ramp is largely featureless at 50 Hz mechanical probe frequency, but gradually also develops into a single peak close to $E = 0$ kV/mm at higher mechanical probe frequencies. Both the positive ramp peaks and the negative ramp peaks remain in approximately the same position across mechanical probe frequencies; however, their crossover point lies in the negative e-field region, and the position of this crossover point shifts more negative with decreasing mechanical probe frequency.

A second feature of note are small dips which occur shortly after the e-field ramp direction changes. These dips are more prominent at higher mechanical probe frequencies, but can be found at all frequencies. As with the positions of the peaks, the positions of these dips appear to be invariant to mechanical probe frequency.

Overall, relative compliance curves at 0.1 Hz remain close to 1 in magnitude, suggesting that only a small degree of mechanically induced domain switching is occurring at low e-field magnitudes, and this switching is constrained at high e-field magnitudes resulting in relative compliance of < 1.

At 1 Hz e-field cycling frequency, relative compliance hysteresis curves take on a more symmetric, "butterfly" appearance with a distinct crossover point close to $E = 0$ kV/mm. While these curves initially look qualitatively very different from their 0.1 Hz e-field counterparts, they in fact possess the same two peaks on the positive and negative e-field ramps, respectively, the same two dips after e-field changes in direction, and a slightly shifting crossover point. As with the 0.1 Hz e-field case, the positions of the peaks and dips appear to be relatively insensitive to mechanical probe frequency, while the crossover point shifts negative toward lower mechanical probe frequencies.

Overall, the relative compliance at 1 Hz is consistently > 1 in contrast to low e-field frequencies, suggesting that mechanically induced domain switching is more prevalent at all e-field magnitudes at high e-field frequencies, i.e. domain walls are more mobile.

Damping

Damping hysteresis curves (Figure 4.2, bottom row) at 0.1 Hz e-field frequency are comparatively more featureless than those of relative compliance, and also have less of a distinct trend. As the absolute magnitude of the damping is low, particularly for low mechanical probe frequencies, it is difficult to distinguish potential features from slight random viscoelastic property variation due to inhomogeneity in the specimen. Nevertheless, at 150 Hz mechanical probe frequency, there is a hint of the same central peak as well as a slight dip where the e-field ramp direction changes. These features occur at the same positions as the corresponding ones in the relative compliance hysteresis, suggesting that they are correlated and thus likely caused by mechanically induced domain switching.

In contrast, hysteresis curves of damping at 1 Hz e-field frequency once again exhibit a distinct "butterfly" shape and resemble the 1 Hz relative compliance curves very closely, with the exception of the shift of the crossover point. Peaks and dips occur at the same position across mechanical probe frequencies, and also correspond to the associated peak and dip positions in relative compliance. High-frequency oscillatory behavior is evident in some curves (mechanical probe frequency of 50, 75 Hz, at electrical cycling frequency of 1 Hz) as their time scales approach a similar order of magnitude. High-frequency oscillations have not been removed during data processing because the low-frequency trends are still sufficiently clear, and the appearance of these oscillations may present useful information.

Although damping at $E = 0$ kV/mm rises with increasing mechanical probe frequency, this is largely an effect of higher frequencies approaching the resonant frequency of the specimen, as seen from Figure 4.1.

Effect of Electric Field Frequency

Figure 4.3 shows the change in hysteresis behavior in electric displacement, relative compliance and damping for a specimen cycled at 0.1, 0.2, 0.5 and 1 Hz e-field frequency and probed mechanically at 50, and 150 Hz, respectively. Electric field frequency has traditionally been associated with elucidation of domain switching

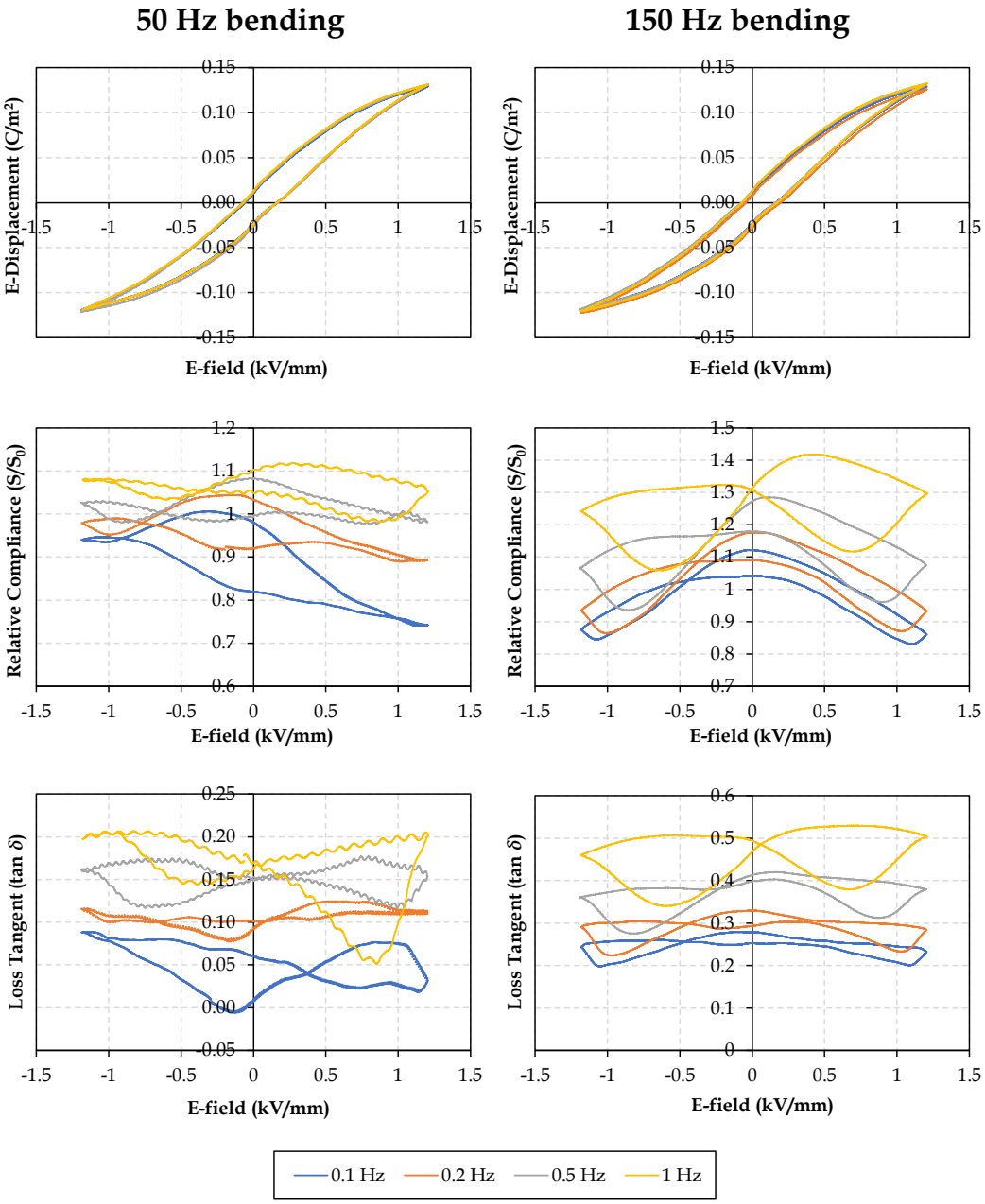

Figure 4.3: Broadband Electromechanical Spectroscopy (BES) hysteresis curves of electric displacement (*top row*), relative compliance (*middle row*) and damping or loss tangent (*bottom row*) for different e-field cycling frequencies at 50 Hz (*left colum*) and 150 Hz (*right column*) mechanical probe frequencies for barium titanate.

kinetics – that if domain switching occurs at a time scale longer than the rate of change of e-field, "viscous" behavior emerges and is reflected as a "stretching" of hysteresis curves, causing key features to occur at higher than expected e-field magnitudes.

In this case, we do not see such kinetic effects, as the electric displacement curves are once again insensitive to changes in e-field cycling frequency, suggesting that domain switching occurs on a time scale shorter than the e-field cycling frequencies we have chosen. Previous work on PZT had attributed differences in viscoelastic properties to the state of polarization because PZT's polarization hysteresis exhibited e-field rate-dependence [Wojnar et al., 2014]. However, here, dramatic e-field rate-dependent changes in viscoelastic properties of BT are presented *without* differences in polarization state, for which the electric displacement curve is a proxy.

Relative Compliance

Both 50 and 150 Hz mechanical probe frequency curves (Figure 4.3, middle row) show a gradual shift of relative compliance hysteresis from a central peak on the positive e-field ramp and either a central peak or trough on the negative ramp at low e-field cycling frequencies to a dual-peak "butterfly" shape at high e-field cycling frequencies. As before, these features are less distinct both at low mechanical probe frequencies and at low e-field cycling frequencies.

The higher central peak at low e-field cycling frequencies which occurs on the positive ramp shifts toward the right (i.e. to more positive e-fields) at higher e-field cycling frequencies. The peak on the negative ramp is also clear in the 150 Hz mechanical probe series of curves, and begins close to $E = 0$ kV/mm then shifts left (i.e. to more negative e-fields) at higher e-field cycling frequencies. Such a peak also exists in the 50 Hz series of curves, beginning at approximately $E = -1$ kV/mm for 0.1 and 0.2 Hz curves, but continues shifting in the negative e-field direction at higher e-field frequencies, hence beyond the amplitude of the applied cyclic e-field. In both series, the position of the crossover point shifts toward more negative e-fields for lower e-field frequencies.

The 150 Hz series shows clear trends in the positions of the dips, which occur close to the point where the e-field switches direction (i.e. high e-field magnitudes) for low e-field frequencies, and move inward towards lower e-field magnitudes at higher e-field frequencies. Once again a similar pattern can be seen in the 50 Hz series, but in a less pronounced fashion.

A final key feature of note is the increasing relative compliance at $E = 0$ kV/mm with increasing e-field frequency, which features prominently in both series, indicating an increased degree of mechanically induced domain switching at higher e-field frequencies.

Damping

Damping hysteresis curves at both mechanical probe frequencies (Figure 4.3, bottom row) appear to mirror their respective relative compliance curves in terms of qualitative features. Both evolve from a central peak to a "butterfly" shape, and exhibit the same trends in movement of peak and dip positions with increasing e-field frequency. Positions of peaks and dips correspond closely to the associated features in the relative compliance curves suggesting a common origin, and can be clearly seen in the 150 Hz mechanical frequency series, while being more subtle in the 50 Hz series, which contains large fluctuations in amplitude as well as the aforementioned high frequency oscillatory signal which masks some of the features.

Damping at $E = 0$ kV/mm also rises with e-field frequency in a manner similar to the rise in relative compliance, supporting the interpretation that higher e-field frequencies enable higher mechanically induced domain wall motion. As evidenced by the electric displacement hysteresis, these polycrystalline BT specimens do not have a distinct coercive field, hence the origin of the peaks, dips and overall rise in relative compliance and damping is more difficult to explain than it was in PZT. However, it is clear that despite a lack of difference in the overall polarization state of the specimen, at higher frequency e-field cycling, domain walls are either more mobile or more abundant, allowing for greater energy absorption. The increase in height of peaks and dips at higher e-field frequencies also suggests that their mobility or abundance correspondingly varies to a greater extent than at low e-field cycling frequencies.

Asymmetry of Mechanical Response

It is of note that almost all viscoelastic hysteresis curves presented thus far have had a high degree of asymmetry, a feature which is not expected in a specimen which is geometrically symmetric, unpoled, and composed of pure undoped BT. Such asymmetry is common in commercially available PZT due to the presence of dopants, secondary phases, and migration of unswitchable charges due to poling. However, this is not the case in the current specimens. To ensure that the asymmetry

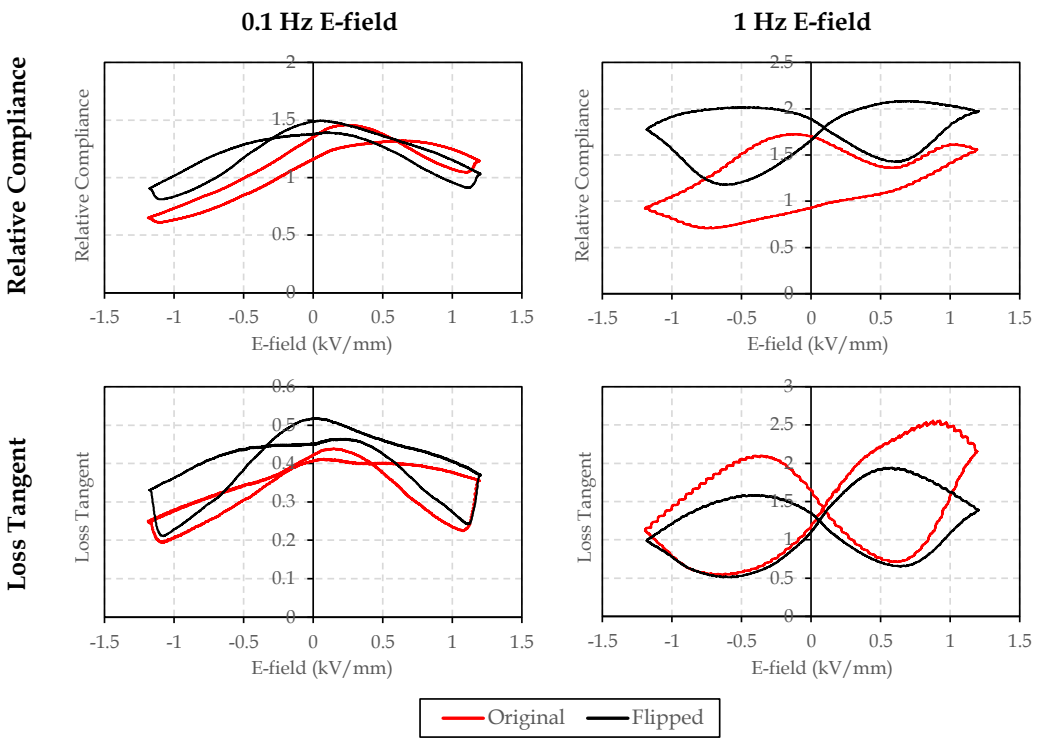

Figure 4.4: Hysteresis curves of relative compliance (*top row*) and damping (*bottom row*) of a polished BT beam specimen in its original position in the BES clamp (*red*), and flipped such that the opposite face faces the laser (*black*). Measurements were taken at both 0.1 Hz (*left*) and 1 Hz (*right*) e-field cycling frequency.

is a feature of the material's switching behavior, procedures to eliminate or reduce the possibility of confounding factors such as experimental setup and microstructural or compositional inhomogeneity were undertaken.

To investigate geometric or experimental setup effects, specimens were polished to remove curvature and BES measurements performed on the same specimen in two orientations – original and flipped about the vertical axis. Representative resulting viscoelastic curves are shown in Figure 4.4. Although the curves differ significantly and are not mirror images of each other, certain key features are mirrored when the specimen is flipped. In particular, the position of the higher central peak as well as the crossover point are reflected in the relative compliance and loss tangent of the 0.1 Hz e-field curves. These results suggest that the asymmetry is inherent in the specimen and is not an artifact of the experimental setup, perhaps due to leakage current or laser geometry.

To elucidate the source of the asymmetry in the specimen, SEM and EDS were

performed on a polished cross-section of the specimen. No variations in grain size were observed through the thickness of the specimen, nor any compositional variation, at least at the spatial resolution and chemical detection sensitivity of the EDS. These observations do not eliminate the possibility of microstructural or compositional variation; however, if such variations exist, they are not significant and appear unlikely to cause the large asymmetry observed in the viscoelastic properties. At present, the origin of the asymmetry is unclear.

Microstructure

To determine the microstructural origin of the e-field frequency dependence of the BT viscoelastic properties, domain structures of an uncycled specimen and specimens electrically cycled at 0.1 Hz and 1 Hz for 1000 cycles were imaged using SEM (Figure 4.5). In each case, most grains exhibit a patchwork-like spinodal domain pattern with no clear laminations. There are also no significant differences in domain morphology between the uncycled specimen and the specimens cycled at different e-field frequencies, suggesting that the process which occurs to give rise to differing domain wall motion during cycling is either not retained upon removal of the e-field, or is perturbed during the polishing process.

More detailed domain structures can be obtained via piezoresponse force microscopy (PFM). Collaborators at ETH Zürich[1] were able to obtain PFM images of the as-sintered surface of our uncycled BT specimens. Without polishing, the topography of the surface prevents imaging of the out-of-plane polarization; however, the in-plane polarization mode, as shown in Figure 4.6, shows clear rank-II laminate patterns on the surface of the grains. At several tens of nanometers in width, rank-II laminates are unlikely to be resolvable through etching, hence the difference in visualized domains between SEM and PFM.

4.4 Discussion

Through BES measurements and microstructural imaging, efforts are made to shed light on the domain switching processes within bulk polycrystalline BT. In Figure 4.7, electric displacement, strain, relative compliance and damping curves of PZT and BT of equivalent dimensions are shown on the same scale. Absolute polarization, strain and damping changes in BT are much smaller compared to PZT, with significantly less hysteresis, suggesting less electrically induced domain switching. It is interesting, however, that relative compliance changes are fairly large, on par

[1] Images were kindly provided by M. Trassin from the M. Fiebig research group at ETH Zürich.

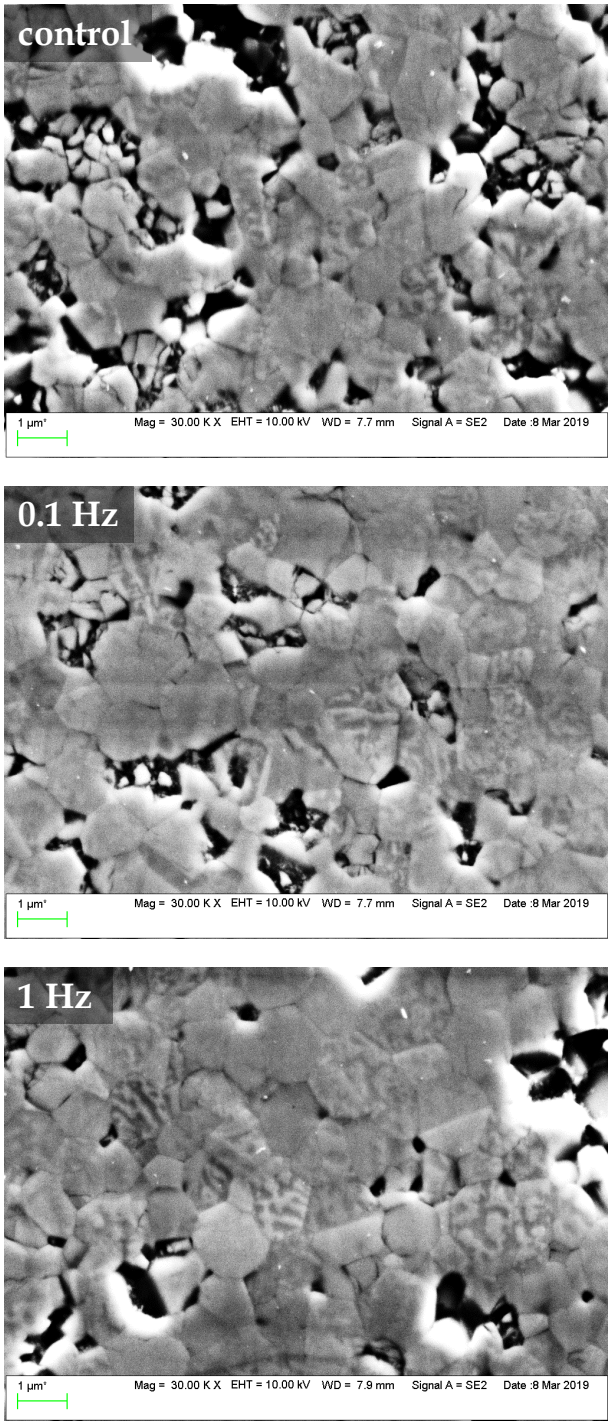

Figure 4.5: Scanning electron microscopy (SEM) micrographs of polished surfaces of BT specimens showing etched domain structures. The control specimen (*top*) was polished as-received. Test specimens were electrically cycled at 0.1 Hz (*middle*) and 1 Hz (*bottom*) for 1000 cycles, then polished and imaged.

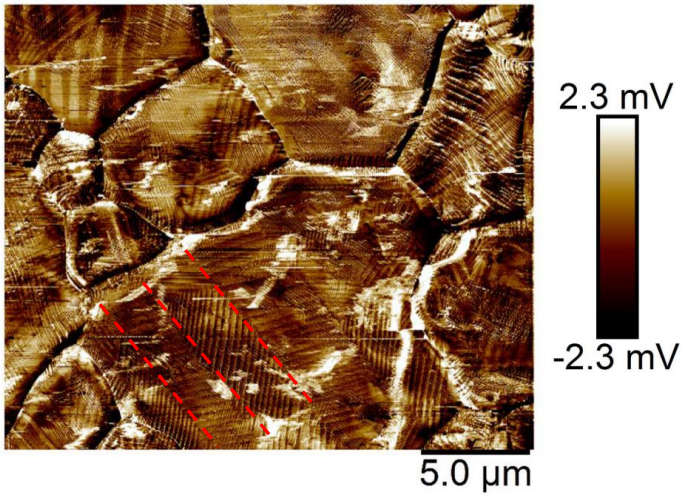

Figure 4.6: In-plane piezoresponse force microscopy (PFM) image of the as-sintered surface of a BT specimen from the same production batch as those tested by BES. Red dotted lines indicate rank-II laminate domain patterns. [Personal communication: V. Kannan and M. Trassin]

with what a PZT specimen exhibits after some electrical fatigue (as per Chapter 3).

Growth vs. Nucleation

To account for all the trends observed in Section 4.3, a ***growth vs. nucleation*** hypothesis of domain switching in polycrystalline BT under differing e-field cycling frequencies is proposed. Figure 4.8 illustrates the crux of this hypothesis – at low e-field cycling frequencies, hence low $\frac{dE}{dt}$, switching occurs via the growth of existing domains. The area of domain walls thus remains largely constant throughout e-field cycling, but the domain wall mobility may vary slightly, giving the offset central peak behavior of relative compliance and damping. At high e-field cycling frequencies, i.e. high $\frac{dE}{dt}$, the nucleation of new domains is theorized, thereby creating new domain walls, thus increasing domain wall area and consequently relative compliance and damping.

Although direct observation of nucleation of new domains has only been done in thin film TEM specimens under a fairly specific sample-substrate configuration [Gao et al., 2013], domain nucleation, coalescence and growth has long been theorized from macroscopic observations and from parallels to other forms of phase transitions [Tagantsev et al., 2010]. First principles atomistic models of domain switching have

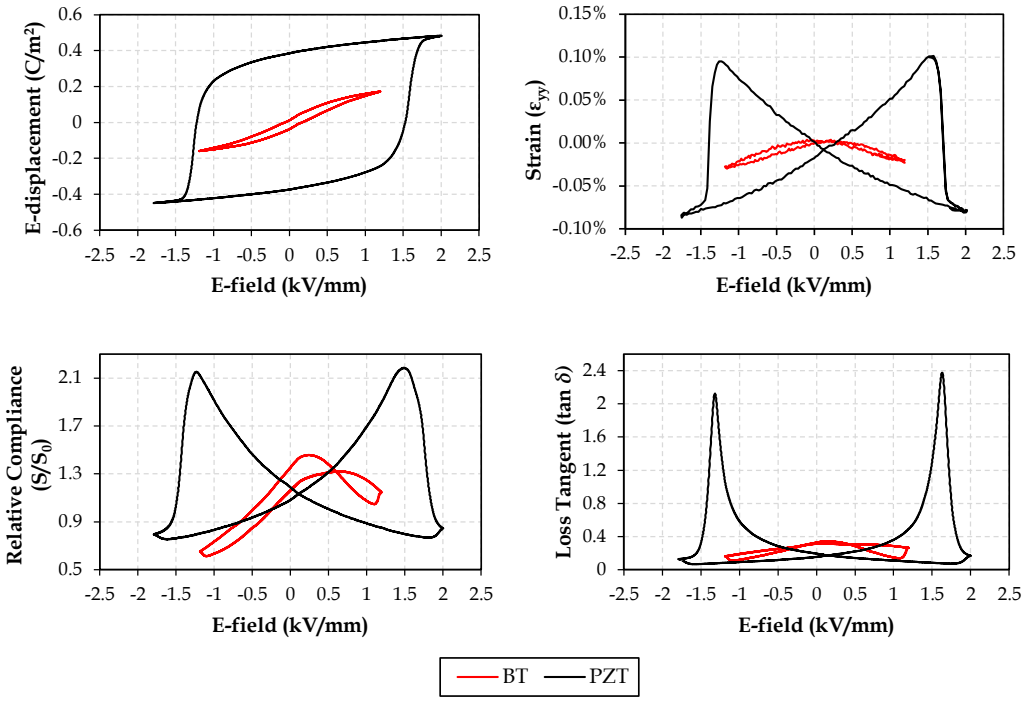

Figure 4.7: Comparison of hysteresis curves of electric displacement (*top left*), strain (*top right*), relative compliance (*bottom left*) and damping (*bottom right*) of PZT (*black*) and BT (*red*). Magnitude of hysteresis of BT is smaller than PZT in all electrical and viscoelastic properties. Curves were taken at 100 Hz mechanical probe frequency and 0.1 Hz e-field cycling frequency on samples of equivalent length.

recently visualized what ferroelectric domain nucleation and growth might look like under different applied e-field strengths [Shin et al., 2007]. One such study by Boddu et al. [2017] is reproduced in Figure 4.9, clearly showing the difference in domain switching behavior under weak and strong e-fields.

The key trends observed in the BES measurements which require explanation are as follows: (*i*) Relative compliance and damping at $E = 0$ kV/mm increase with increasing e-field. (*ii*) Peaks in relative compliance and damping begin at low e-field for low e-field cycling frequencies and move outward toward higher e-fields for high e-field cycling frequencies. (*iii*) Dips in relative compliance and damping occur at high e-fields, almost immediately after the direction of e-field ramp changes for low e-field cycling frequencies, and move inward toward lower e-fields for higher e-field cycling frequencies.

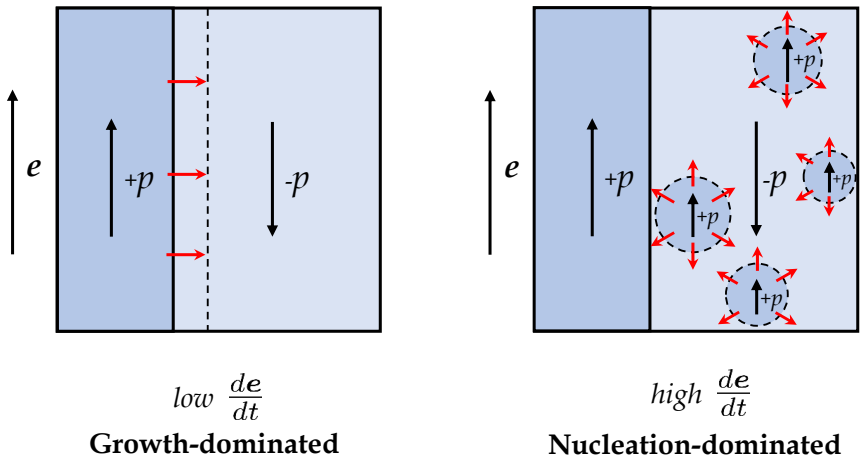

Figure 4.8: Schematic of a growth-dominated mode and nucleation-dominated mode of domain switching under different e-field frequencies. Dotted lines indicate domain walls; the growth-dominated mode retains the same total area of domain walls during switching, while the nucleation-dominated mode increases in total area of domain walls until switched domains merge.

Increasing Base Relative Compliance and Damping

Under the assumption that low e-field cycling frequencies are growth-dominated, large changes in the surface area of domain walls during electrically induced domain switching are not expected, and a low quantity of nucleation also suggests fewer domain walls available for mechanically induced switching to take place. This is consistent with the observed overall low relative compliance and damping during low frequency e-field cycling.

Assuming high e-field cycling frequencies are nucleation-dominated, new domains are expected to constantly nucleate and merge, creating additional domain wall surface area. The additional domain wall surface area allows more mechanically induced domain switching to take place, hence increasing relative compliance and damping due to the increased capacity of mechanical energy absorption. This is consistent with the observed overall higher relative compliance and damping at high frequency e-field cycling.

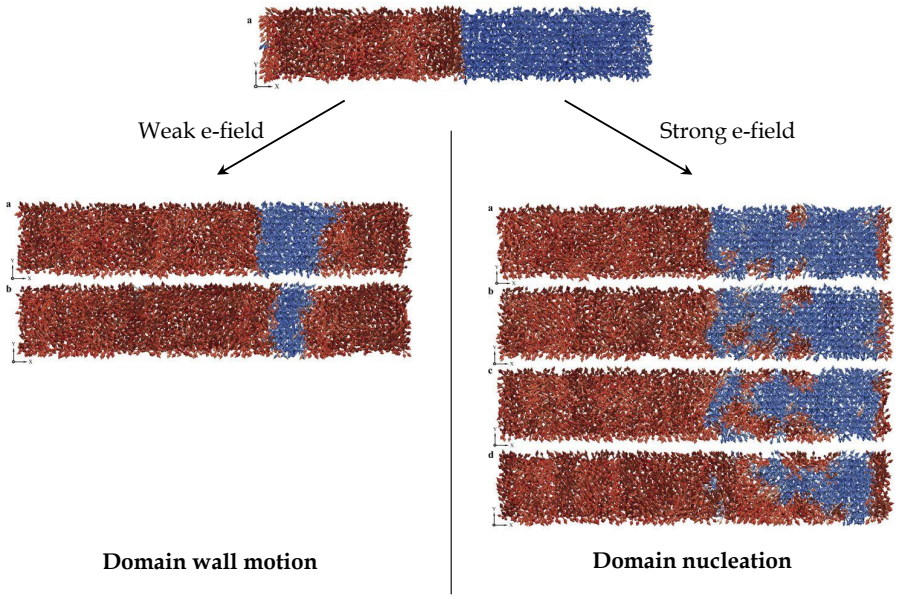

Figure 4.9: A molecular dynamics simulation by Boddu et al. [2017] showing the growth- and nucleation-dominated domain switching mechanisms in single-crystal BT under different applied e-field strengths at a temperature of 310 K. This figure was adapted and reproduced under Open Access.

Peak Divergence

Unlike in PZT where relative compliance and damping peak positions were explained by the position of the coercive field as determined by the electric displacement hysteresis curve, the origin of peaks in polycrystalline BT specimens is less straightforward to identify due to the lack of a sharp coercive field. Instead, increases in relative compliance and damping are postulated to originate from an increase in domain wall surface area.

In a low-frequency, growth-dominated regime, the surface area of domain walls remains relatively constant at all e-field magnitudes, perhaps a slight decrease at high e-fields as some domains may merge. This is reflected in both the relative compliance and damping curves at 0.1 Hz e-field cycling where damping curves are relatively flat, indicating little change in the extent of mechanically induced domain switching.

In a high-frequency, nucleation-dominated regime, the surface area of domain walls would rapidly increase as nucleation takes place, slow down as these nuclei grow and fewer nuclei form, and finally decrease as nuclei merge and domain wall area is lost. This is consistent with the high, fairly symmetric peaks in both e-field ramp

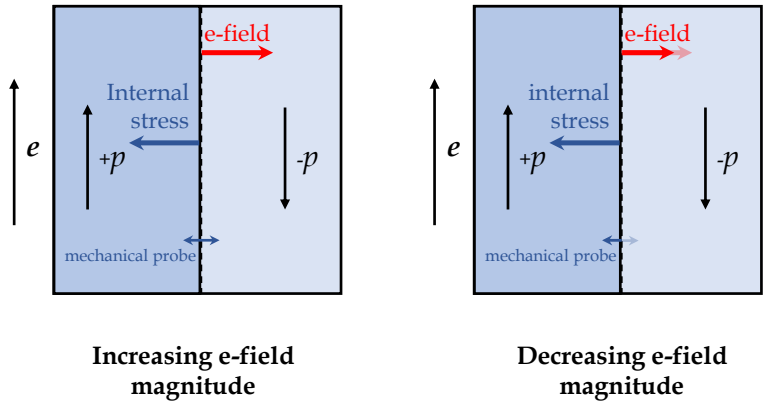

Figure 4.10: Schematic of the effect of e-field ramp direction and internal stress on mechanically induced domain switching activated by applied mechanical oscillation. As the e-field increases (*left*), internal stresses rise to counter the stresses caused by electrically induced switching. As both forces are balanced, external mechanical oscillation can cause switching in both directions. When the e-field decreases (*right*), the large internal stress remains while the e-field induced switching force decreases, resulting in back-switching. As back-switching is mechanically-driven, external mechanical oscillation can no longer induce forward-switching.

directions at 1 Hz e-field cycling frequency. The position of these peaks shifts toward higher e-field magnitude with higher e-field cycling frequency likely due to an increased nucleation probability. The greater the number of nuclei (i.e. highest e-field frequency), the larger the volume fraction of the switched phase can be accommodated within the same volume before merging of nuclei occurs, and hence, the decrease in relative compliance and damping only occurs at higher e-fields.

Strain Limits and Back-switching

Relying solely on a surface area argument overlooks the important fact of strain limits on switching in polycrystalline ferroelectrics, particularly those of single phase which have few avenues of accommodating shape change. Here the effect of back-switching, or internal stress-induced switching which occurs after the removal or reduction of an applied e-field are discussed.

Dip Convergence

Figure 4.10 shows the balance of forces on a domain wall as the applied e-field increases in magnitude, and how those forces change when the applied e-field

switches ramp direction and decreases in magnitude. As the e-field magnitude is increased, the internal stresses rise to counter the force on the domain wall exerted by the e-field. As these forces are balanced, the applied mechanical oscillation can perturb the domain wall in either direction, leading to mechanically induced domain switching. When the applied e-field magnitude is abruptly decreased, as is the case for the triangle waveform used for BES measurements, the internal stresses now exert a greater force on the domain wall than the e-field, leading to internal stress-induced back-switching. The mechanical oscillation now has to counter the force of the internal stress in the forward-switching direction, but not in the back-switching direction. Consequently, only back-switching can be activated by the mechanical oscillation once the e-field magnitude is decreased, hence, the relative compliance and damping, both of which measure the extent of domain switching, drop when the e-field ramp direction changes.

In a low e-field frequency, growth-dominated regime, this dip occurs immediately upon change in direction of e-field ramp as there are no competing factors. The area of the domain walls remains approximately constant. Conversely, in a high e-field frequency, nucleation-dominated regime, the change in e-field direction decreases the domain mobility, but back-switching increases the domain wall area. The former decreases the extent of domain switching while the latter increases it, and this competition is likely what delays the dip in measured relative compliance and damping to lower e-fields.

The dip takes a finite amount of time to occur as internal stresses are relaxed by back-switching while the applied e-field magnitude decreases. When both forces are balanced again, mechanically induced domain switching from the applied mechanical oscillation regains its ability to perturb the domain wall in both directions, causing relative compliance and damping to rise again toward the next peak.

While this hypothesis explains all the salient features of measured BES electrical and viscoelastic results, and is consistent with our current knowledge of domain switching behavior, further verification at the microscale either via in-situ observations of domain evolution or from capturing snapshots of changes in domain morphology ex situ would provide valuable insight to its validity.

4.5 Conclusions

Viscoelastic and electrical properties of unpoled polycrystalline BT were measured in-situ during bipolar electrical loading at 0.1, 0.2, 0.5 and 1 Hz, and mechanical

bending oscillation at 50, 75, 100, 130 and 150 Hz. The electric displacement hysteresis curves were insensitive to both electrical and mechanical loading frequency. Relative compliance and damping hysteresis curves increased in magnitude with increasing mechanical loading frequency, but the positions of key features and turning points were not shifted. However, increasing electrical loading frequency was shown to increase overall magnitude of relative compliance and damping, as well as shift the positions of key features and turning points. These shifts were explained by differences in domain nucleation and growth behavior, where low electrical loading frequency supported growth-dominated domain switching and high frequency supported nucleation-dominated domain switching. The presence of all salient features as well as the directions of their shifts could be explained under this paradigm. Remaining open questions include the determination of the origin of asymmetry of measured hysteresis curves despite specimens having no discernible geometric or microstructural asymmetry, and a microstructural verification of the hypothesized domain switching processes.

Chapter 5

CONCLUSIONS AND OUTLOOK

5.1 Summary

The goal of this thesis was to develop a better understanding of domain switching processes in bulk perovskite ferroelectric ceramics using BT and PZT as representative materials. To do so, microscale physics and macroscale properties needed to be bridged experimentally as well as computationally. The recently-developed technique of Broadband Electromechanical Spectroscopy (BES) [Le Graverend et al., 2015, Kochmann et al., 2014] is one such tool, where elucidation of domain switching processes from macroscale electrical and viscoelastic measurements enabled new insight to be gained into old problems such as the mechanisms of electrical fatigue in PZT ceramics, and the effect of strain limits on domain switching in BT ceramics. Meanwhile, a constitutive material model incorporating microscale domain switching physics was formulated as a step toward predicting macroscale electromechanical properties from microscale processes and vice versa.

In Chapter 2, an efficient, physics-based constitutive model for polycrystalline ferroelectric ceramics was developed and applied towards simulating polarization, strain and energy dissipation hysteresis responses in single-crystal and polycrystalline barium titanate. Physical responses at each scale were taken into account, from the linear piezoelectric properties of the unit cell, to the mixture of 6 tetragonal domains at the single crystal level, to the mixture of randomly oriented grains within a polycrystal. Grains were homogenized via a Taylor model and domains condensed into volume fractions using an entropy-based minimization scheme to enable use of the material model in finite element modeling of real macroscopic specimens. Existing polycrystalline ferroelectric models which capture microscale physics are often too computationally expensive to realize specimen-level simulations. Beam-shaped specimens similar to those used in BES experiments were modeled and exhibited electric field-induced bending due to the base grips, as was also observed in experiments. The effects of precompression on strain hysteresis, of grain texturing on hysteresis curve narrowing, and of the appearance of dissipation hysteresis agreed well qualitatively with experimental observations. This agreement demonstrates that microstructural mechanisms are well-retained, and although the model does not

account for interactions between grains, e.g. internal stress caused by deformation during switching, it shows promise as an efficient way to predict ferroelectric behavior across scales.

Continuing in the vein of scale bridging, the use of Broadband Electromechanical Spectroscopy (BES) together with microstructure imaging of microcracks on PZT specimens undergoing bipolar electrical fatigue enabled the quantification of mechanical damage caused by domain switching in a ferroelectric ceramic in Chapter 3. The electric displacement, relative compliance and damping hysteresis curves of specimens were measured over 1,000,000 bipolar electric field cycles and their key features (e.g. peak heights, $E = 0$ kV/mm values) were tracked. The simultaneous measurement of both electrical and viscoelastic properties demonstrated that electrical properties degraded at a rate far greater than viscoelastic properties did. This prompted the understanding that dissipation by domain wall motion could not be considered under a single umbrella, but had to be differentiated into electrically induced and mechanically induced domain wall motion, the latter of which is measured by the viscoelastic properties of relative compliance and damping. Since fatigue is a complex phenomenon resulting from myriad changes on the microscale ranging from charge migration and domain wall pinning to macro and microcracking, the ability to separate the electrically induced and mechanically induced phenomena using simple macroscale measurements gives valuable insight into the process.

Finally, Chapter 4 employed the above understanding towards interpreting BES measurements of barium titanate. Unlike PZT, barium titanate's electric displacement, relative compliance and damping hysteresis curves were significantly smaller in magnitude, contained no sharp peaks, and generally behaved very differently, qualitatively, from PZT. While it has long been known that PZT on the morphotropic phase boundary is qualitatively different from its single phase compositions and from other tetragonal perovskites like BT due to its crystal structure [Li et al., 2005], this fact is sometimes overlooked, and domain switching in PZT may be discussed in similar terms as that in tetragonal perovskites (i.e. as 90°- and 180°-switching). These results highlighted the flaw in this assumption. Consequently, a new hypothesis on domain switching mechanisms in barium titanate was proposed, incorporating notions of growth-dominated and nucleation-dominated regimes to explain differences in domain switching observed at different electric field cycling frequencies.

In conclusion, the experimental methods presented in this thesis contribute to the understanding of ferroelectric domain switching processes in bulk polycrystals, especially when judiciously paired with microscale observations. Meanwhile the computational methods developed aid in bridging microscale processes to macroscale properties in an approximate but efficient way. Together, they enable a potential pipeline for predicting bulk ferroelectric properties from microscale physics and vice versa.

5.2 Outlook & Future Work

Some remaining open questions and opportunities for future investigations include the following:

- The constitutive model introduced in Chapter 2 could be expanded to include temperature effects via the introduction of a cubic phase and an appropriate temperature-dependent energy term. Given experimental data on fatigue behavior, it could also potentially be adapted to model the degradation of electromechanical properties during fatigue, either with the incorporation of an evolving damage parameter [Lange and Ricoeur, 2016] or an inactive 'void' phase, with the drawback being that this aspect of the model would not be fully physics-based.

- Chapter 3 established that base compliance degradation was directly caused by microcracking. The introduction of cracks in a ferroelectric ceramic under high voltage changes its electrical environment significantly. It would thus be worth modeling the effect of the known density of microcracks on the ferroelectric's polarization hysteresis behavior through FEM to determine how much of polarization degradation is caused by microcracking and how much by internal crystal structure effects, e.g. void formation, domain wall pinning etc.

- The proposed domain switching mechanism in Chapter 4 requires in-situ microstructural verification. Careful design of the sample dimensions and in-situ setup may be necessary to preserve the same domain switching environment as a bulk polycrystal.

- It has been established that grain size affects many properties of a ferroelectric, one of which is domain structure – there exist critical sizes below which

a grain is a monodomain, or can only support rank-I but not rank-II laminates [Arlt, 1990, Schultheiß, 2018]. Testing how grain size affects measured BES properties could give further insight into the domain switching process in barium titanate polycrystals.

- The results in Chapter 4 highlight the importance of crystal symmetry to strain limits, whereby the presence of multiple phases (e.g. tetragonal and rhombohedral in morphotropic PZT) accommodates more strain change and domain switching [Li et al., 2005]. It would thus be interesting to incorporate rhombohedral phases into future models of PZT to verify if the qualitative differences between BT and PZT can be reproduced, especially in high fidelity simulations such as phase field models.

- BT is often subjected to much higher-frequency electrical loads (> 100 Hz) as it is widely used as a capacitor material. Although operating voltages tend to be low, some domain switching may still take place. Thus, investigating its electromechanical response at these frequencies would give valuable information on domain switching processes under normal operating conditions. The BES apparatus is able to apply electrical loads at frequencies of up to 10^4 Hz, however the present setup will need to be redesigned for much higher frequency measurements due to the multiple resonance peaks at high frequencies for samples of the current dimensions.

BIBLIOGRAPHY

S. C. Abrahams, S. K. Kurtz, and P. B. Jamieson. Atomic displacement relationship to curie temperature and spontaneous polarization in displacive ferroelectrics. *Phys. Rev.*, 172:551–553, Aug 1968. doi: 10.1103/PhysRev.172.551. URL http://link.aps.org/doi/10.1103/PhysRev.172.551.

R. Ahluwalia and W. Cao. Computer simulations of domain pattern formation in ferroelectrics. *AIP Conference Proceedings*, 582(1):185–190, 2001. doi: http://dx.doi.org/10.1063/1.1399703. URL http://aip.scitation.org/doi/abs/10.1063/1.1399703.

I. Arias, S. Serebrinsky, and M. Ortiz. A phenomenological cohesive model of ferroelectric fatigue. *Acta Materialia*, 54(4):975–984, 2006. doi: 10.1016/j.actamat.2005.10.035. URL https://doi.org/10.1016/j.actamat.2005.10.035.

G. Arlt and P. Sasko. Domain configuration and equilibrium size of domains in $BaTiO_3$ ceramics. *Journal of Applied Physics*, 51(9), 1980.

G. J. Arlt. Twinning in ferroelectric and ferroelastic ceramics: stress relief. *Journal of Materials Science*, 25:2655, 1990. doi: 10.1007/BF00584864. URL https://doi.org/10.1007/BF00584864.

A. Arockiarajan and C. Sansour. Micromechanical modeling and simulation of rate-dependent effects in ferroelectric polycrystals. *Comp. Mater. Sci.*, 43(4):842–854, 2008. doi: http://dx.doi.org/10.1016/j.commatsci.2008.01.073. URL http://www.sciencedirect.com/science/article/pii/S0927025608000888.

A. Arockiarajan, A. Menzel, B. Delibas, and W. Seemann. Computational modeling of rate-dependent domain switching in piezoelectric materials. *European Journal of Mechanics - A/Solids*, 25(6):950–964, 2006. ISSN 0997-7538. doi: http://dx.doi.org/10.1016/j.euromechsol.2006.01.006. URL http://www.sciencedirect.com/science/article/pii/S0997753806000076.

Sylvie Aubry, Matt Fago, and Michael Ortiz. A constrained sequential-lamination algorithm for the simulation of sub-grid microstructure in martensitic materials. *Computer Methods in Applied Mechanics and Engineering*, 192(26–27):2823 – 2843, 2003. ISSN 0045-7825. doi: http://dx.doi.org/10.1016/S0045-7825(03)00260-3. URL http://www.sciencedirect.com/science/article/pii/S0045782503002603.

M. Avrami. Kinetics of phase change. ii transformation-time relations for random distribution of nuclei. *The Journal of Chemical Physics*, 8(2):212–224, 1940. doi: 10.1063/1.1750631. URL https://doi.org/10.1063/1.1750631.

N. Balke, H. Kungl, T. Granzow, D. C. Lupascu, M. J. Hoffmann, and J. Rödel. Bipolar fatigue caused by feid screening in pb(zr,ti)o_3 ceramics. *Journal of the American Ceramic Society*, 90(12):3869–3874, 2007. doi: 10.1111/j.1551-2916.2007.02041.x. URL https://onlinelibrary.wiley.com/doi/full/10.1111/j.1551-2916.2007.02041.x.

J.M. Ball and R.D. James. Fine phase mixtures as minimizers of energy. *Archive for Rational Mechanics and Analysis*, 100(1):13–52, 1987. ISSN 0003-9527. doi: 10.1007/BF00281246. URL http://dx.doi.org/10.1007/BF00281246.

E. Bassiouny and G. A. Maugin. Thermodynamical formulation for coupled electromechanical hysteresis effects - III. Parameter identification. *International Journal of Engineering Science*, 27(8):975–987, 1989a. ISSN 0020-7225. doi: http://dx.doi.org/10.1016/0020-7225(89)90038-4. URL http://www.sciencedirect.com/science/article/pii/0020722589900384.

E. Bassiouny and G. A. Maugin. Thermodynamical formulation for coupled electromechanical hysteresis effects - IV. Combined electromechanical loading. *International Journal of Engineering Science*, 27(8):989–1000, 1989b. ISSN 0020-7225. doi: http://dx.doi.org/10.1016/0020-7225(89)90039-6. URL http://www.sciencedirect.com/science/article/pii/0020722589900396.

E. Bassiouny, A. F. Ghaleb, and G. A. Maugin. Thermodynamical formulation for coupled electromechanical hysteresis effects - I. Basic equations. *International Journal of Engineering Science*, 26(12):1279–1295, 1988a. ISSN 0020-7225. doi: http://dx.doi.org/10.1016/0020-7225(88)90047-X. URL http://www.sciencedirect.com/science/article/pii/002072258890047X.

E. Bassiouny, A. F. Ghaleb, and G. A. Maugin. Thermodynamical formulation for coupled electromechanical hysteresis effects - II. Poling of ceramics. *International Journal of Engineering Science*, 26(12):1297–1306, 1988b. ISSN 0020-7225. doi: http://dx.doi.org/10.1016/0020-7225(88)90048-1. URL http://www.sciencedirect.com/science/article/pii/0020722588900481.

L. Baudry, I. Lukyanchuk, and V. M. Vinokur. Ferroelectric symmetry-protected multibit memory cell. *Scientific Reports*, 7:42196, 2017. doi: 10.1038/srep42196. URL https://doi.org/10.1038/srep42196.

K. Bhattacharya. *Microstructure of martensite. Why it forms and how it gives rise to the shape-memory effect.* Oxford University Press, Oxford, 2003.

M. A. Biot. *Mechanics of Incremental Deformations*. John Wiley & Sons, New York, 1965.

V. Boddu, F. Endres, and P. Steinmann. Molecular dynamics study of ferroelectric domain nucleation and domain switching dynamics. *Scientific Reports*, 7(806), 2017. doi: 10.1038/s41598-017-01002-0. URL https://doi.org/10.1038/s41598-017-01002-0.

C. Brennan. Model of ferroelectric fatigue due to defect/domain interactions. *Ferroelectrics*, 150(1):199–208, 2010. doi: 10.1080/00150199308008705. URL https://doi.org/10.1080/00150199308008705.

E. Burcsu. *Investigation of Large Strain Actuation in Barium Titanate*. PhD thesis, California Institute of Technology, 2001.

E. Burcsu, G. Ravichandran, and K. Bhattacharya. Large electrostrictive actuation of barium titanate single crystals. *Journal of the Mechanics and Physics of Solids*, 52(4):823–846, 2004. ISSN 0022-5096. doi: http://dx.doi.org/10.1016/j.jmps.2003.08.001. URL http://www.sciencedirect.com/science/article/pii/S0022509603001315.

H. Cao and A.G. Evans. Electric-field-induced fatigue crack growth in piezoelectrics. *Journal of the American Chemical Society*, 77(7):1783–1786, 1994. doi: 10.1111/j.1151-2916.1994.tb07051.x. URL https://doi.org/10.1111/j.1151-2916.1994.tb07051.x.

W. Cao. The strain limits on switching. *Nature Materials*, 4:727–728, 2005. doi: 10.1038/nmat1506. URL https://doi.org/10.1038/nmat1506.

G. P. Carman and G. McKnight. Damping in composite materials through domain wall motion, 01 2002. URL http://appft1.uspto.gov/netacgi/nph-Parser?Sect1=PTO1\&Sect2=HITOFF\&d=PG01\&p=1\&u=/netahtml/PTO/srchnum.html\&r=1\&f=G\&l=50\&s1=20020004543.PGNR. patent.

Carsten Carstensen, Klaus Hackl, and Alexander Mielke. Non-convex potentials and microstructures in finite-strain plasticity. *Proc. R. Soc. London, Ser. A*, 458 (2018):299–317, 2002.

H. Chang, S.V. Kalinin, S. Yang, P. Yu, S. Bhattacharya, P. P. Wu, N. Balke, S. Jesse, L. Q. Chen, R. Ramesh, S. J. Pennycook, and A. Y. Borisevich. Watching domains grow: In-situ studies of polarization switching by combined scanning probe and scanning transmission electron microscopy. *Journal of Applied Physics*, 110(5): 052014, 2011. doi: 10.1063/1.3623779. URL https://doi.org/10.1063/1.3623779.

Yingrui Chang and Dennis M. Kochmann. A variational constitutive model for slip-twinning interactions in hcp metals: Application to single- and polycrystalline magnesium. *International Journal of Plasticity*, 73:39 – 61, 2015. ISSN 0749-6419. doi: http://dx.doi.org/10.1016/j.ijplas.2015.03.008. URL http://www.sciencedirect.com/science/article/pii/S0749641915000637. Special Issue on Constitutive Modeling from Micro-Scale to Continuum in Honor of Prof. Frédéric Barlat.

P. M. Chaplya and G. P. Carman. Investigation of energy absorption capabilities of piezoelectric ceramic. *Proc. SPIE*, 4333:214–220, 2001. doi: 10.1117/12.432759. URL http://dx.doi.org/10.1117/12.432759.

P. M. Chaplya and G. P. Carman. Compression of piezoelectric ceramic at constant electric field: Energy absorption through non-180° domain-wall motion. *Journal of Applied Physics*, 92(3):1504–1510, 2002a. doi: 10.1063/1.1489498. URL http://dx.doi.org/10.1063/1.1489498.

P. M. Chaplya and G. P. Carman. Compression of pzt-5h piezoelectric ceramic at constant electric field: investigation of energy absorption mechanism. *Proc. SPIE*, 4699:124–132, 2002b. doi: 10.1117/12.474967. URL http://dx.doi.org/10.1117/12.474967.

J. Chen. Atomistic field theory of nano energy harvesting. *Journal of Computational and Theoretical Nanoscience*, 8(4):722–728, 2011. doi: doi:10.1166/jctn.2011.1744. URL http://www.ingentaconnect.com/content/asp/jctn/2011/00000008/00000004/art00028.

Kuan-Chia Chen, Wen-Wei Wu, Chien-Neng Liao, Lih-Juann Chen, and K N Tu. Observation of atomic diffusion at twin-modified grain boundaries in copper. *Science*, 321(5892):1066–9, 2008. doi: 10.1126/science.1160777. URL http://dx.doi.org/10.1126/science.1160777.

W. Chen and C. S. Lynch. A micro-electro-mechanical model for polarization switching of ferroelectric materials. *Acta Mater.*, 46(15):5303–5311, 1998. ISSN 1359-6454. doi: http://dx.doi.org/10.1016/S1359-6454(98)00207-9. URL http://www.sciencedirect.com/science/article/pii/S1359645498002079.

W. J. Chen, Y. Zheng, and B. Wang. Vortex domain structure in ferroelectric nanoplatelets and control of its transformation by mechanical load. *Scientific Reports*, 2:796, 2012. URL http://dx.doi.org/10.1038/srep00796.

L. Cheng, B., M. Gabbay, M. Maglione, Y. Jorand, and G. Fantozzi. Domain walls motions in barium titanate ceramics. *J. Phys. IV France*, 06(C8):C8–647–C8–650, 1996. URL http://dx.doi.org/10.1051/jp4:19968139.

P. Chu, D. P. Chen, Y. L. Wang, Y. L. Xie, Z. B. Yan, J-.M. Wan, J. G. Liu, and J. Y. Li. Kinetics of 90° domain wall motions and high frequency mesoscopic dielectric response in strained ferroelectrics: A phase-field simulation. *Scientific Reports*, 4:5007, 2014. doi: 10.1038/srep05007. URL https://doi.org/10.1038/srep05007.

A. C. F. Cocks and R. M. McMeeking. A phenomenological constitutive law for the behaviour of ferroelectric ceramics. *Ferroelectrics*, 228(1):219–228, 1999. ISSN 0015-0193. doi: 10.1080/00150199908226136. URL http://dx.doi.org/10.1080/00150199908226136.

D. Damjanovic and M. Demartin. Contribution of the irreversible displacement of domain walls to the piezoelectric effect in barium titanate and lead zirconate titanate ceramics. *J. Phys.: Condens. Matter*, 9(23):4943–4953, 1997. doi: 10.1088/0953-8984/9/23/018. URL http://dx.doi.org/10.1088/0953-8984/9/23/018.

M. Dawber, K. M. Rabe, and J. F. Scott. Physics of thin-film ferroelectric oxides. *Rev. Mod. Phys.*, 77:1083–1130, Oct 2005. doi: 10.1103/RevModPhys.77.1083. URL https://link.aps.org/doi/10.1103/RevModPhys.77.1083.

A. F. Devonshire. XCVI. Theory of barium titanate. *Philosophical Magazine Series 7*, 40(309):1040–1063, 1949. doi: 10.1080/14786444908561372. URL http://www.tandfonline.com/doi/abs/10.1080/14786444908561372.

A. F. Devonshire. Cix. theory of barium titanate: Part ii. *Philosophical Magazine Series 7*, 42(333):1065–1079, 1951. doi: 10.1080/14786445108561354. URL http://www.tandfonline.com/doi/abs/10.1080/14786445108561354.

Liang Dong, Donald S. Stone, and Roderic S. Lakes. Broadband viscoelastic spectroscopy measurement of mechanical loss and modulus of polycrystalline $BaTiO_3$ vs. temperature and frequency. *Physica Status Solidi (b)*, 245(11):2422–2432, 2008. doi: 10.1002/pssb.200880270. URL http://dx.doi.org/10.1002/pssb.200880270.

A. Dorfmann and R.W. Ogden. Nonlinear electroelasticity. *Acta Mechanica*, 174: 167–183, 2005.

H.M. Duiker, P.D. Beale, and J.F. Scott. Fatigue and switching in ferroelectric memories: Theory and experiment. *Journal of Applied Physics*, 68(11):5783, 1990. doi: 10.1063/1.346948. URL https://doi.org/10.1063/1.346948.

M. Elhadrouz, T. Ben Zineb, and E. Patoor. Constitutive law for ferroelectric and ferroelastic single crystals: a micromechanical approach. *Computational Materials Science*, 32(3–4):355–359, 2005. doi: http://dx.doi.org/10.1016/j.commatsci.2004.09.032. URL http://www.sciencedirect.com/science/article/pii/S0927025604002149.

Zhongming Fan and Xiaoli Tan. In-situ TEM study of the aging micromechanisms in a $BaTiO_3$-based lead-free piezoelectric ceramic. *Journal of the European Ceramic Society*, 38(10):3472 – 3477, 2018. ISSN 0955-2219. doi: https://doi.org/10.1016/j.jeurceramsoc.2018.03.049. URL http://www.sciencedirect.com/science/article/pii/S095522191830195X.

P. Gao, J. Britson, J.R. Jokisaari, C.T. Nelson, S.H. Baek, Y. Wang, C.B. Eom, L.Q. Chen, and X. Pan. Atomic-scale mechanisms of ferroelastic domain-wall-mediated ferroelectric switching. *Nature Communications*, 4(1):2791, 2013. doi: 10.1038/ncomms3791. URL http://dx.doi.org/10.1038/ncomms3791.

P. Gao, J. Britson, C.T. Nelson, J.R. Jokisaari, D. Chen, M. Trassin, S.H. Baek, H. Guo, L. Li, Y. Wang, Y.H. Chu, A.M. Minor, C.B. Eom, R. Ramesh, L.Q. Chen, and X. Pan. Ferroelastic domain switching dynamics under electrical and mechanical excitations. *Nature Communications*, 5(1):3801, 2014. doi: 10.1038/ncomms4801. URL http://dx.doi.org/10.1038/ncomms4801.

Y.A. Genenko, J. Glaum, M.J. Hoffmann, and K. Albe. Mechanisms of aging and fatigue in ferroelectrics. *Materials Science and Engineering: B*, 192(1):52–82, 2015. doi: 10.1016/j.mseb.2014.10.003. URL https://doi.org/10.1016/j.mseb.2014.10.003.

N. Goulbourne, E. Mockensturm, and M. Frecker. A nonlinear model for dielectric elastomer membranes. *Journal of Applied Mechanics*, 72:899–906, 2005.

A. Gruverman, D. Wu, H.-J. Fan, I. Vrejoiu, M. Alexe, R. J. Harrison, and J. F. Scott. Vortex ferroelectric domains. *Journal of Physics: Condensed Matter*, 20 (34):342201, 2008. URL http://stacks.iop.org/0953-8984/20/i=34/a=342201.

W. H. Gu and K. T. Faber. Tensile behavior of microcracking SiC-TiB_2 composites. *Journal of the American Ceramic Society*, 78(6):1507 – 1512, 1995. doi: 10.1111/j.1151-2916.1995.tb08845.x. URL https://onlinelibrary.wiley.com/doi/abs/10.1111/j.1151-2916.1995.tb08845.x.

H. Guo, X. Liu, J. Rödel, and X. Tan. Nanofragmentation of ferroelectric domains during polarization fatigue. *Advanced Functional Materials*, 25(1):270–277, 2015. doi: 10.1002/adfm.201402740. URL https://doi.org/10.1002/adfm.201402740.

J. Hadamard. *Lecons sur la propagation des ondes et les équations de l'hydrodynamique*. Hermann, Paris, 1903.

G. H. Haertling. Ferroelectric ceramics: History and technology. *Journal of the American Ceramic Society*, 82(4):797–818, 1999. ISSN 1551-2916. doi: 10.1111/j.1151-2916.1999.tb01840.x. URL http://dx.doi.org/10.1111/j.1151-2916.1999.tb01840.x.

M. G. Harwood, P. Popper, and D. F. Rushman. Curie point of barium titanate. *Nature*, 160:58–59, 1947. doi: 10.1038/160058a0. URL https://doi.org/10.1038/160058a0.

D. S. Helman. Symmetry-based electricity in minerals and rocks: A summary of extant data, with examples of centrosymmetric minerals that exhibit pyro- and piezoelectricity. *Periodico di Mineralogia*, 85:201–248, 2016. doi: 10.2451/2016PM590. URL http://dx.doi.org/10.2451/2016PM590.

H. Hinterstein, J. Rouquette, J. Haines, Ph. Papet, J. Glaum, M. Knapp, J. Eckert, and M. Hoffman. Mechanisms of aging and fatigue in ferroelectrics. *Physics Review B*, 90(9):094113, 2014. doi: 10.1103/PhysRevB.90.094113. URL https://doi.org/10.1103/PhysRevB.90.094113.

S. Hong, E.L. Colla, E. Kim, D.V. Taylor, A.K. Tagantsev, P. Muralt, K. No, and N. Setter. High resolution study of domain nucleation and growth during polarization switching in Pb(Zr,Ti)O_3 ferroelectric thin film capacitors. *Journal*

of Applied Physics, 86(1):607–613, 1999. doi: 10.1063/1.370774. URL http://dx.doi.org/10.1063/1.370774.

M.W. Hooker. Properties of pzt-based piezoelectric ceramics between -150 to 250°c. Technical report, National Aeronautics and Space Administration, Langley Research Center, 09 1998.

Y. H. Hu, H. M. Chan, Z. X. Wen, and M. P. Harmer. Scanning electron microscopy and transmission electron microscopy study of ferroelectric domains in doped $BaTiO_3$. *Journal of the American Ceramic Society*, 69(8):594–602, 1986. doi: 10.1111/j.1151-2916.1986.tb04814.x. URL http://dx.doi.org/10.1111/j.1151-2916.1986.tb04814.x.

J. E. Huber. Micromechanical modelling of ferroelectrics. *Current Opinion in Solid State and Materials Science*, 9(3):100–106, 2005. doi: http://dx.doi.org/10.1016/j.cossms.2006.05.001. URL http://www.sciencedirect.com/science/article/pii/S1359028606000404.

J. E. Huber and N. A. Fleck. Multi-axial electrical switching of a ferroelectric: theory versus experiment. *Journal of the Mechanics and Physics of Solids*, 49(4):785–811, 2001. doi: http://dx.doi.org/10.1016/S0022-5096(00)00052-1. URL http://www.sciencedirect.com/science/article/pii/S0022509600000521.

J.E. Huber and N.A. Fleck. Ferroelectric switching: a micromechanics model versus measured behaviour. *European Journal of Mechanics - A/Solids*, 23(2):203 – 217, 2004. ISSN 0997-7538. doi: http://dx.doi.org/10.1016/j.euromechsol.2003.11.006. URL http://www.sciencedirect.com/science/article/pii/S0997753803001335.

J.e. Huber, N.a. Fleck, C.M. Landis, and R.M. McMeeking. A constitutive model for ferroelectric polycrystals. *Journal of the Mechanics and Physics of Solids*, 47(8):1663 – 1697, 1999. ISSN 0022-5096. doi: http://dx.doi.org/10.1016/S0022-5096(98)00122-7. URL http://www.sciencedirect.com/science/article/pii/S0022509698001227.

Yongzhong Huo and Qing Jiang. Modeling of domain switching in polycrystalline ferroelectric ceramics. *Smart Materials and Structures*, 6(4):441–447, aug 1997. doi: 10.1088/0964-1726/6/4/008. URL https://doi.org/10.1088/0964-1726/6/4/008.

S. C. Hwang, C. S. Lynch, and R. M. McMeeking. Ferroelectric/ferroelastic interactions and a polarization switching model. *Acta Metallurgica et Materialia*, 43(5):2073–2084, 1995. ISSN 0956-7151. doi: http://dx.doi.org/10.1016/0956-7151(94)00379-V. URL http://www.sciencedirect.com/science/article/pii/095671519400379V.

M. I. Idiart. Modeling two-phase ferroelectric composites by sequential laminates. *Modelling and Simulation in Materials Science and Engineering*, 22(2):025010, 2014. URL http://stacks.iop.org/0965-0393/22/i=2/a=025010.

Y. Ishibashi and Y. Takagi. Note on ferroelectric domain switching. *Journal of the Physical Society of Japan*, 31(2):506–510, 1971. doi: 10.1143/JPSJ.31.506. URL https://doi.org/10.1143/JPSJ.31.506.

B. Jaffe, W. R. Jr. Cook, and H. Jaffe. *Piezoelectric Ceramics*. Academic Press, New-York & London, 1971.

B. Jiménez and J.M. Vicente. Influence of mobile 90° domains on the complex elastic modulus of pzt ceramics. *Journal of Physics D: Applied Physics*, 33(12): 1525, 2000. URL http://stacks.iop.org/0022-3727/33/i=12/a=315.

F. Jona and G. Shirane. Ferroelectric crystals. 1962.

M. Kachanov. Effective elastic properties of cracked solids: Critical review of some basic concepts. *Applied Mechanics Reviews*, 45:304–335, 1992. doi: 10.1115/1.3119761. URL https://doi.org/10.1115/1.3119761.

S. V. Kalinin, A. Rar, and S. Jesse. A decade of piezoresponse force microscopy: progress, challenges, and opportunities. *IEEE Transactions on Ultrasonics, Ferroelectrics, and Frequency Control*, 53(12):2226–2252, 2006. doi: 10.1109/TUFFC.2006.169. URL https://doi.org/10.1109/TUFFC.2006.169.

M. Kamlah. Ferroelectric and ferroelastic piezoceramics - modeling of electromechanical hysteresis phenomena. *Continuum Mechanics and Thermodynamics*, 13(4):219–268, 2001. ISSN 0935-1175. doi: 10.1007/s001610100052. URL http://dx.doi.org/10.1007/s001610100052.

M. Kamlah and C. Tsakmakis. Phenomenological modeling of the non-linear electro-mechanical coupling in ferroelectrics. *International Journal of Solids and Structures*, 36(5):669–695, 1999. doi: 10.1016/S0020-7683(98)00040-7. URL http://dx.doi.org/10.1016/S0020-7683(98)00040-7.

S. Karasawa. Origin of piezoelectricity in an alpha-quartz. *Japanese Journal of Applied Physics*, 13:799–803, 1974. doi: 10.1143/JJAP.13.799. URL https://doi.org/10.1143/JJAP.13.799.

T'ing-Sui Kê. Experimental evidence of the viscous behavior of grain boundaries in metals. *Physical Review*, 71:533–546, Apr 1947. doi: 10.1103/PhysRev.71.533. URL http://link.aps.org/doi/10.1103/PhysRev.71.533.

S.J. Kim and Q. Jiang. Microcracking and electric fatigue of polycrystalline ferroelectric ceramics. *Smart Materials and Structures*, 5(3):321, 1996. doi: 10.1088/0964-1726/5/3/010. URL https://doi.org/10.1088/0964-1726/5/3/010.

David Kinderlehrer. Twinning of crystals (ii). In StuartS. Antman, J.L. Ericksen, David Kinderlehrer, and Ingo Müller, editors, *Metastability and Incompletely Posed Problems*, volume 3 of *The IMA Volumes in Mathematics and Its Applications*, pages 185–211. Springer New York, 1987. ISBN 978-1-4613-8706-0. doi:

10.1007/978-1-4613-8704-6_12. URL http://dx.doi.org/10.1007/978-1-4613-8704-6_12.

D. M. Kochmann and K. Hackl. The evolution of laminates in finite crystal plasticity: a variational approach. *Continuum Mechanics and Thermodynamics*, 23(1):63–85, 2011. doi: 10.1007/s00161-010-0174-5. URL http://www.springerlink.com/content/b02h6085l620u737/?MUD=MP.

D. M. Kochmann, C. S. Wojnar, and J.-B. le Graverend. Broadband electromechanical spectroscopy, 10 2014. URL https://patents.google.com/patent/US20140298918A1/en. patent.

H. Kohlstedt, Y. Mustafa, A. Gerber, A. Petraru, M. Fitsilis, R. Meyer, U. Böttger, and R Waser. Current status and challenges of ferroelectric memory devices. *Microelectronic Engineering*, 80:296 – 304, 2005. ISSN 0167-9317. doi: https://doi.org/10.1016/j.mee.2005.04.084. URL http://www.sciencedirect.com/science/article/pii/S0167931705002236. 14th biennial Conference on Insulating Films on Semiconductors.

A. N. Komolgorov. On the statistical theory of the crystallization of metals. *Bulletin of the Russian Academy of Sciences: Mathematics*, 1(2):355–359, 1937.

A. Kontsos and C. M. Landis. Computational modeling of domain wall interactions with dislocations in ferroelectric crystals. *International Journal of Solids and Structures*, 46(6):1491–1498, 2009. doi: http://dx.doi.org/10.1016/j.ijsolstr.2008.11.021. URL http://www.sciencedirect.com/science/article/pii/S0020768308004939.

R. S. Lakes. Viscoelastic measurement techniques. *Review of Scientific Instruments*, 75(4):797–810, 2004. doi: 10.1063/1.1651639. URL http://link.aip.org/link/?RSI/75/797/1.

R.S. Lakes. *Viscoelastic Solids*. CRC Mechanical Engineering Series. CRC Press, 1999. URL http://books.google.com/books?id=soZZl17sm5IC.

R.S. Lakes and J. Quackenbusch. Viscoelastic behavior in indium tin alloys over a wide range of frequency and time. *Philosophical Magazine Letters*, 74:227–238, 1996. URL http://silver.neep.wisc.edu/~lakes/gInSn.pdf.

L.D. Landau. On the theory of phase transitions (in russian). *Zh. Eksp. Teor. Fiz.*, 7:19–32, 1937.

C. M. Landis. Fully coupled, multi-axial, symmetric constitutive laws for polycrystalline ferroelectric ceramics. *Journal of the Mechanics and Physics of Solids*, 50 (1):127–152.

C. M. Landis. Non-linear constitutive modeling of ferroelectrics. *Current Opinion in Solid State and Materials Science*, 8(1):59 – 69, 2004. ISSN

1359-0286. doi: http://dx.doi.org/10.1016/j.cossms.2004.03.010. URL http://www.sciencedirect.com/science/article/pii/S1359028604000397.

C. M. Landis and R. M. McMeeking. A self-consistent constitutive model for switching in polycrystalline barium titanate. *Ferroelectrics*, 255(1):13–34, 2001. doi: 10.1080/00150190108225965. URL https://doi.org/10.1080/00150190108225965.

S. Lange and A. Ricoeur. High cycle fatigue damage and life time prediction for tetragonal ferroelectrics under electromechanical loading. *International Journal of Solids and Structures*, 80(1):181–192, 2016. doi: 10.1016/j.ijsolstr.2015.11.003. URL https://doi.org/10.1016/j.ijsolstr.2015.11.003.

J. B. Le Graverend, C. S. Wojnar, and D. M. Kochmann. Broadband electromechanical spectroscopy (bes): Measuring the dynamic mechanical response of viscoelastic materials under temperature and electric-field control in a vacuum environment. *J. Mater. Sci.*, 50(10):3656–3685, 2015. doi: 10.1007/s10853-015-8928-x. URL http://dx.doi.org/10.1007/s10853-015-8928-x.

J. Y. Li, R. C. Rogan, E. ÜstÜndag, and K. Bhattacharya. Domain switching in polycrystalline ferroelectric ceramics. *Nature Materials*, 4:776–781, 2005. doi: 10.1038/nmat1485. URL https://doi.org/10.1038/nmat1485.

Y. W. Li and F. X. Li. The effect of domain patterns on 180° domain switching in batio3 crystals during antiparallel electric field loading. *Applied Physics Letters*, 104(4):042908, 2014. doi: 10.1063/1.4863672. URL https://doi.org/10.1063/1.4863672.

Z. Li, S.K. Chan, M.H. Grimsditch, and E.S. Zouboulis. The elastic and electromechanical properties of tetragonal $BaTiO_3$ single crystals. *Journal of Applied Physics*, 70(12):7327–7332, 1991. doi: 10.1063/1.349751. URL http://dx.doi.org/10.1063/1.349751.

M. E. Lines and A. M. Glass. *Principles and applications of ferroelectrics and related materials*. Oxford University Press, 1977. ISBN 019850778X.

E. A. Little. Dynamic behavior of domain walls in barium titanate. *Physical Review*, 98(4):978–984, 1955. URL http://link.aps.org/doi/10.1103/PhysRev.98.978. PR.

Q.D. Liu and J.E. Huber. State dependent linear moduli in ferroelectrics. *International Journal of Solids and Structures*, 44(17):5635 – 5650, 2007. ISSN 0020-7683. doi: http://dx.doi.org/10.1016/j.ijsolstr.2007.01.014. URL http://www.sciencedirect.com/science/article/pii/S0020768307000224.

S. Liu, I. Ginberg, and A. M. Rappe. Intrinsic ferroelectric switching from first principles. *Nature*, 534:360, 2016. doi: 10.1038/nature18286. URL https://doi.org/10.1038/nature18286.

D.C. Lupascu. *Fatigue in Ferroelectric Ceramics and Related Issues*. Springer, 2004.

C.S. Lynch, L. Chen, Z. Suo, R.M. Mcmeeking, and W. Yang. Crack growth in ferroelectric ceramics driven by cyclic polarization switching. *Journal of Intelligent Material Systems and Structures*, 6(2):191–198, 1995. doi: 10.1177/1045389X9500600206. URL https://doi.org/10.1177/1045389X9500600206.

W. J. Merz. Switching time in ferroelectric $BaTiO_3$ and its dependence on crystal thickness. *Journal of Applied Physics*, 27(8):938–943, 1956. URL http://dx.doi.org/10.1063/1.1722518.

Walter J. Merz. Domain formation and domain wall motions in ferroelectric $BaTiO_3$ single crystals. *Physical Review*, 95(3):690–698, 1954. URL http://link.aps.org/doi/10.1103/PhysRev.95.690. PR.

C. Miehe and D. Rosato. A rate-dependent incremental variational formulation of ferroelectricity. *International Journal of Engineering Science*, 49(6):466–496, 2011. ISSN 0020-7225. doi: http://dx.doi.org/10.1016/j.ijengsci.2010.11.003. URL http://www.sciencedirect.com/science/article/pii/S0020722510002466. Theoretical-Read 05/14/13.

A. Migliori, J.L. Sarrao, V.M. Visscher, T.M. Bell, M. Lei, Z. Fisk, and R.G. Leisure. Resonant ultrasound spectroscopic techniques for measurement of the elastic moduli of solids. *Physica B: Condensed Matter*, 183:1–24, 1993. doi: 10.1016/0921-4526(93)90048-B. URL http://www.sciencedirect.com/science/article/pii/092145269390048B.

Robert C. Miller. Some experiments on the motion of 180° domain walls in $batio_3$. *Phys. Rev.*, 111:736–739, Aug 1958. doi: 10.1103/PhysRev.111.736. URL https://link.aps.org/doi/10.1103/PhysRev.111.736.

I. J. Mohamad, L. J. Zammit-Mangion, E. F. Lambson, G. A. Saunders, and A. E. Abey. Acoustic emission from ferroelectric crystals. *Ferroelectrics*, 38:983, 1981. doi: 10.1080/00150198108209600. URL http://dx.doi.org/10.1080/00150198108209600.

P. Mokrý, P. Psota, K. Steiger, J. Václavík, R. Doleček, D. Vápenka, and V. Lédl. Ferroelectric domain pattern in barium titanate single crystals studied by means of digital holographic microscopy. *Journal of Physics D: Applied Physics*, 49(25):255307, may 2016. doi: 10.1088/0022-3727/49/25/255307. URL https://doi.org/10.1088/0022-3727/49/25/255307.

K. Momma and F. Izumi. Vesta 3 for three-dimensional visualization of crystal, volumetric and morphology data. *Journal of Applied Crystallography*, 44:1272–1276, 2011. doi: 10.1107/S0021889811038970. URL https://doi.org/10.1107/S0021889811038970.

G. P. Morosova and O. Y. Serdobolskaja. Acoustical emission by switching gadolinium molybdate. *Ferroelectrics*, 75:449–453, 1987. doi: 10.1080/00150198708215066. URL http://dx.doi.org/10.1080/00150198708215066.

A. J. Moulson and J. M. Herbert. Electronic ceramic materials and their applications. *Chappman and Hall, London*, 1990.

Neel Nadkarni, Chiara Daraio, Rohan Abeyaratne, and Dennis M. Kochmann. Universal energy transport law for dissipative and diffusive phase transitions. *Phys. Rev. B*, 93:104109, Mar 2016. doi: 10.1103/PhysRevB.93.104109. URL http://link.aps.org/doi/10.1103/PhysRevB.93.104109.

J. Nuffer, D.C. Lupascu, and J. Rödel. Damage evolution in ferroelectric PZT induced by bipolar electric cycling. *Acta Materialia*, 48(14):191–198, 2000. doi: 10.1016/S1359-6454(00)00173-7. URL https://doi.org/10.1016/S1359-6454(00)00173-7.

M. Ortiz and L. Stainier. The variational formulation of viscoplastic constitutive updates. *Computer Methods in Applied Mechanics and Engineering*, 171(3–4):419 – 444, 1999. ISSN 0045-7825. doi: http://dx.doi.org/10.1016/S0045-7825(98)00219-9. URL http://www.sciencedirect.com/science/article/pii/S0045782598002199.

Metin Ozgul, Susan Trolier-McKinstry, and Clive A. Randall. Influence of electrical cycling on polarization reversal processes in $Pb(Zn_{1/3}Nb_{2/3})O_3$-$PbTiO_3$ ferroelectric single crystals as a function of orientation. *Journal of Applied Physics*, 95(8):4296–4302, 2004. doi: 10.1063/1.1687046. URL https://doi.org/10.1063/1.1687046.

Metin Ozgul, Susan Trolier-Mckinstry, and Clive A. Randall. Fatigue induced effects on bipolar strain loops in pzn-pt piezoelectric single crystals. *Journal of Electroceramics*, 20(3):133–138, Aug 2008. doi: 10.1007/s10832-007-9120-8. URL https://doi.org/10.1007/s10832-007-9120-8.

X. Pan and L. Li. Atomic structures and dynamic behaviors of domain walls in ferroelectric thin films. *European Microscopy Congress 2016: Proceedings*, pages 944–945, 2016. doi: 10.1002/9783527808465.EMC2016.6341. URL https://doi.org/10.1002/9783527808465.EMC2016.6341.

S.-E. Park and T. R. Shrout. Ultrahigh strain and piezoelectric behavior in relaxor based ferroelectric single crystals. *Journal of Applied Physics*, 82(4):1804–1811, 1997. doi: 10.1063/1.365983. URL https://doi.org/10.1063/1.365983.

J. R. Partington. *An Advanced Treatise on Physical Chemistry – Volume 1, Fundamental Principles*. Longmans, Green, and Co., London, 1949.

Y. Pasco and A. Berry. A hybrid analytical/numerical model of piezoelectric stack actuators using a macroscopic nonlinear theory of ferroelectricity and a preisach model of hysteresis. *Journal of intelligent material systems and structures*, 15(5): 375–386, 2004. ISSN 1045-389X.

L. Pálová, P. Chandra, and K.M. Rabe. Modeling the dependence of properties of ferroelectric thin film on thickness. *Physical Review B*, 76(1):014112, 2007. doi: 10.1103/PhysRevB.76.014112. URL http://dx.doi.org/10.1103/PhysRevB.76.014112.

M. J. Polking, M.-G. Han, A. Yourdkhani, V. Petkov, C. F. Kisielowski, V. V. Volkov, Y. Zhu, G. Caruntu, A. P. Alivisatos, and R Ramesh. Ferroelectric order in individual nanometre-scale crystals. *Nature Materials*, 11:700–709, 2012. doi: 10.1038/nmat3371. URL https://doi.org/10.1038/nmat3371.

W. Promsawat, N. Promsawat, S. Jiansirisomboon, O. Namsar, F. Marlton, J. Daniels, and S. Pojprapai. Investigation of frequency effect on electrical fatigue and crack tip domain-switching behaviors in $Pb(Mg_{1/3}Nb_{2/3})_{0.65}Ti_{0.35}O_3$ ceramics via synchrotron X-ray diffraction. *Journal of the European Ceramic Society*, 37(15):4609–4616, 2017. doi: 10.1016/j.jeurceramsoc.2017.06.020. URL https://doi.org/10.1016/j.jeurceramsoc.2017.06.020.

U. Robels and G. Arlt. Domain wall clamping in ferroelectrics by orientation of defects. *Journal of Applied Physics*, 73:3454, 1993. doi: 10.1063/1.352948. URL https://doi.org/10.1063/1.352948.

T. Rojac, M. Kosec, B. Budic, N. Setter, and D. Damjanovic. Strong ferroelectric domain-wall pinning in $BiFeO_3$ ceramics. *Journal of Applied Physics*, 108: 074107, 2010. doi: 10.1063/1.3490249. URL https://doi.org/10.1063/1.3490249.

C. A. Rosen, K. A. Fish, and H. C. Rothenberg. Broadband electromechanical spectroscopy, 1 1954. URL https://patents.google.com/patent/US2830274A/en. patent.

Yukio Sato, Tsukasa Hirayama, and Yuichi Ikuhara. Real-time direct observations of polarization reversal in a piezoelectric crystal: $Pb(mg_{1/3}nb_{2/3})\mathbf{o}_3{-}pbtio_3$ studied via in situ electrical biasing transmission electron microscopy. *Phys. Rev. Lett.*, 107:187601, Oct 2011. doi: 10.1103/PhysRevLett.107.187601. URL https://link.aps.org/doi/10.1103/PhysRevLett.107.187601.

C. A. Schneider, W. S. Rasband, and K. W. Eliceiri. NIH Image to ImageJ: 25 years of image analysis. *Nature methods*, 9(7):671–675, 2012. doi: 10.1038/nmeth.2089. URL https://www.nature.com/articles/nmeth.2089.

D. Schrade, R. Müller, D. Gross, M.-A. Keip, H. Thai, and J. Schröder.

D. Schrade, R. Mueller, D. Gross, T. Utschig, V. Y. Shur, and D. C. Lupascu. Interaction of domain walls with defects in ferroelectric materials. *Mechanics of materials*, 39(2):161–174, 2007. ISSN 0167-6636.

J. Schröder and H. Romanowski. A thermodynamically consistent mesoscopic model for transversely isotropic ferroelectric ceramics in a coordinate-invariant setting. *Archive of Applied Mechanics*, 74(11):863–877, 2005. doi: 10.1007/s00419-005-0412-7. URL http://dx.doi.org/10.1007/s00419-005-0412-7.

J. Schultheiß. *Polarization reversal dynamics in polycrystalline ferroelectric/ferroelastic ceramic materials*. PhD thesis, Technische Universität Darmstadt, 2018.

J. K. Shang and X. Tan. A maximum strain criterion for electric-field-induced fatigue crack propagation in ferroelectric ceramics. *Materials Science and Engineering: A*, 301(2):131 – 139, 2001. ISSN 0921-5093. doi: https://doi.org/10.1016/S0921-5093(00)01812-8. URL http://www.sciencedirect.com/science/article/pii/S0921509300018128.

J. Shieh, N.A. Fleck, and J.E. Huber. Observation of fatigue crack growth in ferroelectrics under electrical loading. volume 4699, pages 4699 – 4699 – 13, 2002. doi: 10.1117/12.475016. URL https://doi.org/10.1117/12.475016.

J. Shieh, J.H. Yeh, Y.C. Shu, and J.H. Yen. Hysteresis behaviors of barium titanate single crystals based on the operation of multiple 90° switching systems. *Materials Science and Engineering B*, 161(1):50–54, 2009. doi: 10.1016/j.mseb.2008.11.046. URL http://dx.doi.org/10.1016/j.mseb.2008.11.046.

D. Shilo, E. Burcsu, G. Ravichandran, and K. Bhattacharya. A model for large electrostrictive actuation in ferroelectric single crystals. *International Journal of Solids and Structures*, 44(6):2053 – 2065, 2007. ISSN 0020-7683. doi: https://doi.org/10.1016/j.ijsolstr.2006.07.020. URL http://www.sciencedirect.com/science/article/pii/S0020768306002940. Physics and Mechanics of Advanced Materials.

Y. H. Shin, I. Grinberg, I-.W. Chen, and A. M. Rappe. Nucleation and growth mechanism of ferroelectric domain-wall motion. *Nature*, 449(881-884), 2007. doi: 10.1038/nature06165. URL https://doi.org/10.1038/nature06165.

Y. C. Shu and K. Bhattacharya. Domain patterns and macroscopic behaviour of ferroelectric materials. *Philosophical Magazine Part B*, 81(12):2021–2054, 2001. doi: 10.1080/13642810108208556. URL http://www.tandfonline.com/doi/abs/10.1080/13642810108208556.

Y. Su and C. M. Landis. Continuum thermodynamics of ferroelectric domain evolution: Theory, finite element implementation, and application to domain wall pinning. *Journal of the Mechanics and Physics of Solids*, 55(2):280–305, 2007. doi: http://dx.doi.org/10.1016/j.jmps.2006.07.006. URL http://www.sciencedirect.com/science/article/pii/S0022509606001256.

E. C. Subbarao, M. C. McQuarrie, and W. R. Buessem. Domain effects in polycrystalline barium titanate. *Journal of Applied Physics*, 28(10):1194–1200, 1957. doi: 10.1063/1.1722606. URL https://doi.org/10.1063/1.1722606.

Michael A. Sutton. *Digital Image Correlation for Shape and Deformation Measurements*, pages 565–600. Springer US, Boston, MA, 2008. ISBN 978-0-387-30877-7. doi: 10.1007/978-0-387-30877-7_20. URL https://doi.org/10.1007/978-0-387-30877-7_20.

K.Y. Sze and N. Sheng. Polygonal finite element method for nonlinear constitutive modeling of polycrystalline ferroelectrics. *Finite Elements in Analysis and Design*, 42:107–129, 2005. doi: 10.1016/j.finel.2005.04.004. URL https://doi.org/10.1016/j.finel.2005.04.004.

A. K. Tagantsev, E. L. Cross, and J. Fousek. *Domains in Ferroic Crystal and Thin Flims*. Springer, 2010. ISBN 978-1-4419-1416-3.

A.K. Tagantsev and I.A. Stolichnov. Injection-controlled size effect on switching of ferroelectric thin films. *Applied Physics Letters*, 74:1326, 1999. doi: 10.1063/1.123539. URL https://doi.org/10.1063/1.123539.

Hidemi Takasu. The ferroelectric memory and its applications. *Journal of Electroceramics*, 4(2):327–338, Jun 2000. ISSN 1573-8663. doi: 10.1023/A:1009910525462. URL https://doi.org/10.1023/A:1009910525462.

Y. Tan, J. Zhang, Y. Wu, C. Wang, V. Koval, B. Shi, H. Ye, R. McKinnon, G. Viola, and Haixue Yan. Unfolding grain size effects in barium titanate ferroelectric ceramics. *Scientific Reports*, 5:9953, 2015. doi: 10.1038/srep09953. URL https://doi.org/10.1038/srep09953.

N. T. Tsou, P. R. Potnis, and J. E. Huber. Classification of laminate domain patterns in ferroelectrics. *Phys. Rev. B*, 83:184120, May 2011. doi: 10.1103/PhysRevB.83.184120. URL http://link.aps.org/doi/10.1103/PhysRevB.83.184120.

K. Uchino. *Piezoelectric Actuators and Ultrasonic Motors*. Springer US, 1997.

Y. Uetsuji, T. Hata, T. Oka, H. Kuramae, and K. Tsuchiya. Multiscale simulation of domain switching behavior in polycrystalline ferroelectric materials. *Computational Materials Science*, 106(1):100–110, 2015. doi: 10.1016/j.commatsci.2015.03.035. URL http://dx.doi.org/10.1016/j.commatsci.2015.03.035.

S. Wada, K. Yako, K. Yokoo, H. Kakemoto, and T. Tsurumi. Domain wall engineering in barium titanate single crystals for enhanced piezoelectric properties. *Ferroelectrics*, 334(1):17–27, 2006. doi: 10.1080/00150190600689647. URL https://doi.org/10.1080/00150190600689647.

H. N. G. Wadley. Acoustic emission source characterization. *The Journal of the Acoustical Society of America*, 68:103, 1980. doi: 10.1121/1.2004511. URL http://dx.doi.org/10.1121/1.2004511.

C. S. Wojnar. *Exploring the Kinetics of Domain Switching in Ferroelectrics for Structural Applications*. PhD thesis, California Institute of Technology, 2014.

C. S. Wojnar, J.-B. le Graverend, and D. M. Kochmann. Broadband control of the viscoelasticity of ferroelectrics by electric fields. *Appl. Phys. Lett.*, 105(16): 162912, 2014. doi: 10.1063/1.4899055. URL http://dx.doi.org/10.1063/1.4899055.

B.-X. Xu, D. Schrade, R. Müller, D. Gross, T. Granzow, and J. Rödel. Phase field simulation and experimental investigation of the electro-mechanical behavior of ferroelectrics. *ZAMM - Journal of Applied Mathematics and Mechanics/Zeitschrift für Angewandte Mathematik und Mechanik*, 90(7-8):623–632, 2010. ISSN 1521-4001.

Y. Yu, N. Naganathan, and R. Dukkipati. Preisach modeling of hysteresis for piezoceramic actuator system. *Mechanism and Machine Theory*, 37(1):49–59.

N. Zhang, L. Li, and Z. Gui. Frequency dependence of ferroelectric fatigue in PLZT ceramics. *Journal of the European Ceramic Society*, 21(5):677–681, 2001. doi: 10.1016/S0955-2219(00)00248-X. URL https://doi.org/10.1016/S0955-2219(00)00248-X.

Q. Zhang. *Atomistic Simulations of Barium Titanate*. PhD thesis, California Institute of Technology, 2004.

W. Zhang and K. Bhattacharya. A computational model of ferroelectric domains. Part I: model formulation and domain switching. *Acta Materialia*, 53(1):185–198, 2005a. doi: http://dx.doi.org/10.1016/j.actamat.2004.09.016. URL http://www.sciencedirect.com/science/article/pii/S1359645404005580. Read 04/25/13.

W. Zhang and K. Bhattacharya. A computational model of ferroelectric domains. Part II: grain boundaries and defect pinning. *Acta Materialia*, 53(1):199–209, 2005b. doi: http://dx.doi.org/10.1016/j.actamat.2004.09.015. URL http://www.sciencedirect.com/science/article/pii/S1359645404005579.

Luo Zhenhua, Glaum Julia, Granzow Torsten, Jo Wook, Dittmer Robert, Hoffman Mark, and Rödel Jürgen. Bipolar and unipolar fatigue of ferroelectric bnt-based lead-free piezoceramics. *Journal of the American Ceramic Society*, 94(2):529–535, 2011. doi: 10.1111/j.1551-2916.2010.04101.x. URL https://onlinelibrary.wiley.com/doi/abs/10.1111/j.1551-2916.2010.04101.x.

L. Zhou, N. Zhang, A. Zimmerman, F. Aldinger, and L. Li. Frequency dependent electric fatigue in antiferroelectric pzst ceramics. *Ferroelectrics*, 315(1):61–71, 2004. doi: 10.1080/00150190590933005. URL https://doi.org/10.1080/00150190590933005.

S. Zhukov, S. Fedosov, J. Glaum, T. Granzow, Y. A. Genenko, and H. von Seggern. Effect of bipolar electric fatigue on polarization switching in lead-zirconate-titanate ceramics. *Journal of Applied Physics*, 108(1):014105, 2010. doi: 10.1063/1.3452326. URL https://doi.org/10.1063/1.3452326.

S. Zhukov, J. Glaum, H. Kungl, E. Sapper, R. Dittmer, Y.A. Genenko, and H. von Seggern. Fatigue effect on polarization switching dynamics in polycrystalline bulk ferroelectrics. *Journal of Applied Physics*, 120(6):064103, 2016. doi: 10.1063/1.4960691. URL https://doi.org/10.1063/1.4960691.

Appendix A

DOMAIN REMANENT STRAINS IN THE REUSS MODEL

The convexification-based constitutive model described in Section 2.2 uses the Reuss bound to compute the effective response at the single-grain level from the mixture of domain variants. This requires solving for the individual domain strains in order to determine stresses in (2.31). The linear set of equations to be solved for the remanent strains in the ferroelectric domains is

$$\begin{aligned}
\mathbb{C}_\alpha\left(\boldsymbol{\varepsilon}_{\alpha+}-\boldsymbol{\varepsilon}^r_{\alpha+}\right) &= \mathbb{C}_\alpha\left(\boldsymbol{\varepsilon}_{\alpha-}-\boldsymbol{\varepsilon}^r_{\alpha-}\right),\\
\mathbb{C}_\beta\left(\boldsymbol{\varepsilon}_{\beta+}-\boldsymbol{\varepsilon}^r_{\beta+}\right) &= \mathbb{C}_\beta\left(\boldsymbol{\varepsilon}_{\beta-}-\boldsymbol{\varepsilon}^r_{\beta-}\right),\\
\mathbb{C}_\gamma\left(\boldsymbol{\varepsilon}_{\gamma+}-\boldsymbol{\varepsilon}^r_{\gamma+}\right) &= \mathbb{C}_\gamma\left(\boldsymbol{\varepsilon}_{\gamma-}-\boldsymbol{\varepsilon}^r_{\gamma-}\right),\\
\mathbb{C}_\alpha\left(\boldsymbol{\varepsilon}_{\alpha+}-\boldsymbol{\varepsilon}^r_{\alpha+}\right) &= \mathbb{C}_\beta\left(\boldsymbol{\varepsilon}_{\beta+}-\boldsymbol{\varepsilon}^r_{\beta+}\right),\\
\mathbb{C}_\beta\left(\boldsymbol{\varepsilon}_{\beta+}-\boldsymbol{\varepsilon}^r_{\beta+}\right) &= \mathbb{C}_\gamma\left(\boldsymbol{\varepsilon}_{\gamma+}-\boldsymbol{\varepsilon}^r_{\gamma+}\right),\\
\lambda_{\alpha+}\boldsymbol{\varepsilon}_{\alpha+}+\lambda_{\alpha-}\boldsymbol{\varepsilon}_{\alpha-}+\lambda_{\beta+}\boldsymbol{\varepsilon}_{\beta+}+\lambda_{\beta-}\boldsymbol{\varepsilon}_{\beta-}+\lambda_{\gamma+}\boldsymbol{\varepsilon}_{\gamma+}+\lambda_{\gamma-}\boldsymbol{\varepsilon}_{\gamma-} &= \boldsymbol{\varepsilon},
\end{aligned} \tag{A.1}$$

where $\alpha+$ and $\alpha-$ refer to a pair of 180° domains, and α, β, γ represent the three orthogonal pairs of domains in a tetragonal perovskite structure. We further note that the remanent strains $\boldsymbol{\varepsilon}^r_{\alpha+}$ and $\boldsymbol{\varepsilon}^r_{\alpha-}$ represent the coupled strains as per (2.68), such that (for $\chi=\alpha,\beta,\gamma$)

$$\boldsymbol{\varepsilon}^r_{\chi+}=\boldsymbol{\varepsilon}^r_{\chi}\left(1+\delta_{\chi+}\right) \tag{A.2a}$$

$$\boldsymbol{\varepsilon}^r_{\chi-}=\boldsymbol{\varepsilon}^r_{\chi}\left(1-\delta_{\chi+}\right) \tag{A.2b}$$

with

$$\delta_{\chi+}=\xi\,\frac{\boldsymbol{e}}{e_c}\cdot\frac{\boldsymbol{p}_{\chi+}}{p_s}, \tag{A.3}$$

so that, from (A.1), strains of opposite domains are related via

$$\boldsymbol{\varepsilon}_{\chi+}=\boldsymbol{\varepsilon}_{\chi-}+2\boldsymbol{\varepsilon}^r_{\chi}\delta_{\chi+}. \tag{A.4}$$

The above system of six linear equations then reduces to the three equations

$$\mathbb{C}_\alpha \left(\boldsymbol{\varepsilon}_{\alpha-} - \boldsymbol{\varepsilon}^r_{\alpha-}\right) = \mathbb{C}_\beta \left(\boldsymbol{\varepsilon}_{\beta-} - \boldsymbol{\varepsilon}^r_{\beta-}\right), \tag{A.5a}$$

$$\mathbb{C}_\beta \left(\boldsymbol{\varepsilon}_{\beta-} - \boldsymbol{\varepsilon}^r_{\beta-}\right) = \mathbb{C}_\gamma \left(\boldsymbol{\varepsilon}_{\gamma-} - \boldsymbol{\varepsilon}^r_{\gamma-}\right), \tag{A.5b}$$

$$\begin{aligned}\left(\lambda_{\alpha+} + \lambda_{\alpha-}\right)\boldsymbol{\varepsilon}_{\alpha-} + \left(\lambda_{\beta+} + \lambda_{\beta-}\right)\boldsymbol{\varepsilon}_{\beta-} + \left(\lambda_{\gamma+} + \lambda_{\gamma-}\right)\boldsymbol{\varepsilon}_{\gamma-} \\ +2\left(\lambda_{\alpha+}\boldsymbol{\varepsilon}^r_\alpha\delta_{\alpha+} + \lambda_{\beta+}\boldsymbol{\varepsilon}^r_\beta\delta_{\beta+} + \lambda_{\gamma+}\boldsymbol{\varepsilon}^r_\gamma\delta_{\gamma+}\right) = \boldsymbol{\varepsilon},\end{aligned} \tag{A.5c}$$

whose solution is

$$\begin{aligned}
\boldsymbol{\varepsilon}_{\gamma-} =& \frac{1}{\lambda_\gamma}\left(\boldsymbol{\varepsilon}^* - \lambda_\alpha\boldsymbol{\varepsilon}_{\alpha-} - \lambda_\beta\boldsymbol{\varepsilon}_{\beta-}\right), \\
\boldsymbol{\varepsilon}_{\alpha-} =& \left[\boldsymbol{I} + \mathbb{C}_\alpha^{-1}\mathbb{C}_\gamma\frac{\lambda_\alpha}{\lambda_\gamma}\right]^{-1}\mathbb{C}_\alpha^{-1}\left[\mathbb{C}_\gamma\frac{1}{\lambda_\gamma}\left(\boldsymbol{\varepsilon}^* - \lambda_\beta\boldsymbol{\varepsilon}_{\beta-}\right) - \boldsymbol{\sigma}^r_{\gamma-} + \boldsymbol{\sigma}^r_{\alpha-}\right], \\
\boldsymbol{\varepsilon}_{\beta-} =& \left[\mathbb{C}_\beta + \mathbb{C}_\alpha\left[\boldsymbol{I} + \mathbb{C}_\alpha^{-1}\mathbb{C}_\gamma\frac{\lambda_\alpha}{\lambda_\gamma}\right]^{-1}\mathbb{C}_\alpha^{-1}\mathbb{C}_\gamma\frac{\lambda_\beta}{\lambda_\gamma}\right]^{-1} \\
& \left[\mathbb{C}_\alpha\left[\boldsymbol{I} + \mathbb{C}_\alpha^{-1}\mathbb{C}_\gamma\frac{\lambda_\alpha}{\lambda_\gamma}\right]^{-1}\mathbb{C}_\alpha^{-1}\left[\mathbb{C}_\gamma\frac{1}{\lambda_\gamma}\boldsymbol{\varepsilon}^* - \boldsymbol{\sigma}^r_{\gamma-} + \boldsymbol{\sigma}^r_{\alpha-}\right] - \boldsymbol{\sigma}^r_{\alpha-} + \boldsymbol{\sigma}^r_{\beta-}\right]
\end{aligned} \tag{A.6}$$

with

$$\lambda_\alpha = \lambda_{\alpha+}+\lambda_{\alpha-}, \quad \boldsymbol{\sigma}^r_{\alpha-} = \mathbb{C}_\alpha\boldsymbol{\varepsilon}^r_{\alpha-}, \quad \boldsymbol{\varepsilon}^* = \boldsymbol{\varepsilon} - 2\left(\lambda_{\alpha+}\boldsymbol{\varepsilon}^r_\alpha\delta_{\alpha+} + \lambda_{\beta+}\boldsymbol{\varepsilon}^r_\beta\delta_{\beta+} + \lambda_{\gamma+}\boldsymbol{\varepsilon}^r_\gamma\delta_{\gamma+}\right). \tag{A.7}$$

Appendix B

HIGHER-ORDER ENERGY-MINIMIZING DOMAIN PATTERNS

As discussed in Section 2.2, the Reuss and Voigt constructions make no assumption about the spatial arrangement of ferroelectric domains. The condensed energy density (2.45) confirms this as follows. Assume that domains form a higher-order laminate, i.e., assume that each of the n domains decomposes into m domains in a hierarchical fashion, and that the volume fractions within each of the n domains are obtained from energy minimization. This implies that the energy of a first-order domain α is obtained from an energy-minimizing second-order domain mixture, i.e.,

$$F_{\text{cond.,}\alpha} = -kT \log \left[\sum_{\beta=1}^{m} \exp(-W_{\alpha\beta}/T) \right], \tag{B.1}$$

and insertion into the final solution of (2.45) for W_α leads to the total enthalpy

$$F_{\text{cond.}} = -kT \log \left[\sum_{\alpha=1}^{n} \sum_{\beta=1}^{m} \exp(-W_{\alpha\beta}/T) \right]. \tag{B.2}$$

This result, however, is the same as if we had started with $n \times m$ domains on the same microstructural level. Consequently, the spatial arrangement of domains is not accounted for in the Reuss and Voigt constructions.